EXPERIMENTAL AND ANALYTICAL INVESTIGATIONS OF SOLITARY WAVES ON A BEACH

A Dissertation

Presented to the Faculty of the Graduate School

of Cornell University

in Partial Fulfillment of the Requirements for the Degree of

Doctor of Philosophy

by

Nimish Pujara

August 2015

© 2015 Nimish Pujara
ALL RIGHTS RESERVED

EXPERIMENTAL AND ANALYTICAL INVESTIGATIONS OF SOLITARY WAVES ON A BEACH

Nimish Pujara, Ph.D.

Cornell University 2015

This thesis presents theoretical and experimental investigations of the flow on a beach, *i.e.*, the swash, due to solitary waves with the objective of understanding the flow processes that govern complex coastal hydrodynamics.

The bed shear stress is identified as an important quantity and consequently, a shear plate sensor is developed to make accurate measurements of the bed shear stress. Its size is designed to be small enough to give spatially local measurements and its bandwidth high enough to resolve time-varying forcing due to waves. Typically, shear plate sensors are restricted to zero pressure gradient flows because secondary forces on the edge of the shear plate caused by pressure gradients can introduce large errors. To address this issue, a theory is developed to analyze the pressure distribution at the edges of the shear plate and a new methodology is introduced for correcting for the pressure gradient force. Experimental results are presented that show that this methodology improves the accuracy of the sensor.

The swash flow created by solitary waves beyond the stillwater shoreline on a plane, impermeable beach is studied. Measurements of the bed shear stress, flow velocities, water depths, bed pressure and shoreline motion are presented for a wide range of incident solitary waves that span different regimes of wave breaking. The flow evolution due to breaking solitary waves is found to be a gravity-driven flow that is scaled by the initial velocity of the shoreline, which,

in turn, is shown to be predicted by measurements of wave height near the still-water shoreline. Experimental results are presented that show how different wave breaking regimes influence the initial shoreline velocity, the swash flow evolution, the run-up and the time period of the swash. Time-histories of the bed shear stress are also presented, but a new normalization for the peak values of the bed shear stress using the initial shoreline velocity shows the cross-shore variation of bed shear stress and the influence of different wave breaking regimes.

The effects of bed friction are found to significantly alter the flow in the leading edge of the swash, near the moving shoreline. A theory is developed that considers the leading order dynamical balance in the swash tip, treating it in a bulk sense. Predictions of the shoreline motion from the theory compare very well to the measured shoreline motion.

Experiments are also conducted to study the interaction between successive solitary waves incident on a beach. Two cases are examined: a strongly interacting case and a weakly interacting case. The parameters relevant to predicting the strength of interaction between the swash of successive solitary waves are given. Measurements of bed shear stress, bed pressure and velocity are also used to explain the complex boundary layer dynamics that occur in the interaction of the swash flows due to successive waves.

BIOGRAPHICAL SKETCH

The author was born in Rajkot, India in July 1988 and graduated from Cambridge University with a Master of Engineering (MEng) degree in June 2010. Since August 2010, he has been living in Ithaca, NY studying fluid mechanics in the School of Civil & Environmental Engineering at Cornell University and learning a lot about himself in the process. He strives to develop intuitive understanding of the phenomena that he studies through experiments and theory.

To my parents, for their love and support

ACKNOWLEDGEMENTS

First and foremost, I would like to thank my advisor, Philip Liu, for his belief, support, and patience, during my time at Cornell. Phil has been generous with his time and energy, and from his example I have learned the importance of self-critical examination of one's own work. His lucid lecturing and teaching style have also been a source of inspiration. Sincere thanks must also go to members of the special committee: Edwin (Todd) Cowen, Harry Yeh, and Zellman Warhaft. Todd has been an approachable ally in all matters related to the DeFrees hydraulics laboratory and also a useful resource in discussing research. Todd has also been a great mentor for teaching and I would also like to thank him for the opportunities and the support he provided me to be a teaching assistant for his courses. Harry has been a fantastic research mentor: his enthusiasm for discussing the experiments and generosity in sharing his knowledge are much appreciated. I have also been fortunate to learn aspects scientific communication from him. Zellman's support and interest in my research provided me with the encouragement I needed to move forward to the proposal exam and beyond.

When I first arrived at Cornell, Yong Sung Park took me under his wing and helped me start my project, spending time to help me design the first version of the shear plate sensor and build it in the machine shop. Thank you, Yong Sung, for introducing to me the laboratory and for the many discussions we had. Thanks must also go to Tim Brock, Paul Charles, and Jack Powers for teaching me to use the tools in the machine shop, helping me with many parts of the design and construction, and troubleshooting laboratory equipment. Cameron Willkens helped to solve all problems related to IT and electronics, often at short notice.

The EFMH community has been an engaging group of people and an environment that facilitated learning and research. A special mention must go to the 'Hollister 114 blackboard group': Chao An, Jose Gonzalez, Blair Johnson, Mahmoud Sadek, Patricio Winckler, Qi Zhou. I am glad to have had these companions to share this journey with; we did not shy away from teaching and learning from each other. I would also like to acknowledge all staff in the main office (Karen, Carl, Jeannette, Su, Tania) and other staff (Jeff, Mark) who made Hollister Hall an efficient and enjoyable place to come to everyday.

A large component of the experimental work in this work was conducted at Oregon State University in the Hinsdale Wave Research Laboratory. The staff and faculty there were very helpful: From planning to experimental set up, data acquisition and analysis, their support was instrumental for the success of the experiments. I am grateful to Melora Park, Tim Maddux, Jason Killian, and Adam Ryan for all their help.

The support from the National Science Foundation (NSF) and the Network for Earthquake Engineering Simulation (NEES) through research grants (CMMI-1041541) to support this work is acknowledged.

Finally, none of this would have been possible without the love and support from my parents and my brother. I dedicate this work to them.

The swash, the swash,
ever present and it's gone again,
a stranger who speaks alone in a crowd.
In the wind under a cloudless grey sky,
it tells stories from its past:
I was ready to collapse
when the curve of identity was lost
to the curls of velocity
in the clouds of lathered milk.
The wave, the wave, again it returns,
to trace its arc back to the ocean again.
It leaves me to wish for the whole once more.

TABLE OF CONTENTS

LIST OF TABLES

LIST OF FIGURES

CHAPTER 1

INTRODUCTION

1.1 Motivation and background

The importance of coasts to human well-being cannot be underestimated. Apart from providing habitable areas (as of 2010, 40% of the population of the U.S. occupied less than 10% of the landmass that lies adjacent to its coast, NOAA, 2013), they provide access to the sea for transportation, sources of food, and commerce. However, coastal regions around the world are increasingly at risk from rising sea levels, higher intensity storm surges that produce extreme wave conditions (leading to coastal erosion, overtopping and flooding), and unsustainable practices in coastal management (IPCC, 2014). Magnifying these issues is the fact that migration towards the coast continues as a trend worldwide. Larger population densities in coastal regions place higher pressures on natural resources while also increasing the risks to people and infrastructure due to flooding, sea-level rise and erosion. Higher levels of pollutants are released into natural systems and energy demands are increased. Lakeshore communities share many of the same concerns of erosion, damage to infrastructure due to wave action, and management of healthy lake ecology. Thus, sustainable management of coastal and lakeshore regions is of increasing importance. This need calls for further fundamental research into nearshore hydrodynamics to understand the evolution of coastlines and beaches.

1.1.1 Waves on a beach and the swash zone

Surface gravity waves occur throughout the ocean and at different scales. This work is primarily concerned with waves in the nearshore region since this is where the interaction of the land and the ocean occurs. Svendsen (2006) defines the nearshore region as: *the region between the shoreline and a fictive offshore limit which is usually defined as the limit where the depth becomes so large that it no longer influences the waves ... This definition is practical becase the influence of the bottom on the waves is one of the most important mechanisms in nearshore hydrodynamics.*

The nearshore region can take many different forms, but the research presented here is motivated by waves on a beach and their role as part of a 'beach system' (illustrated in Figure 1.1). The most landward influence of waves on a beach occurs in what is called the 'swash zone'. The swash is defined as the region between the wave run-up and run-down limits. Essentially it is the flow behind the moving shoreline that climbs and recedes periodically. Although the swash occupies a relatively narrow extent in the cross-shore direction, it is an important region for coastal processes such as run-up and overtopping (*e.g.*, Battjes, 1974; Peregrine, 1983), sediment transport (*e.g.*, Butt and Russell, 2000; Elfrink and Baldock, 2002; Puleo and Butt, 2006; Bakhtyar *et al.*, 2009), beach morphodynamics (*e.g.*, Masselink and Puleo, 2006; Brocchini and Baldock, 2008), forces on coastal structures (*e.g.* Fenton and Rienecker, 1982), and mass transport in the nearshore region (Fischer *et al.*, 1979; Winckler *et al.*, 2013). The swash flow dyanmics are also coupled to the ground-water flow (*e.g.*, Horn, 2006), the evolution of flow turbulence (*e.g.*, Longo *et al.*, 2002; Sou *et al.*, 2010), and due to the grouping of waves in the swash, the larger surf zone dynamics (Brocchini, 2006).

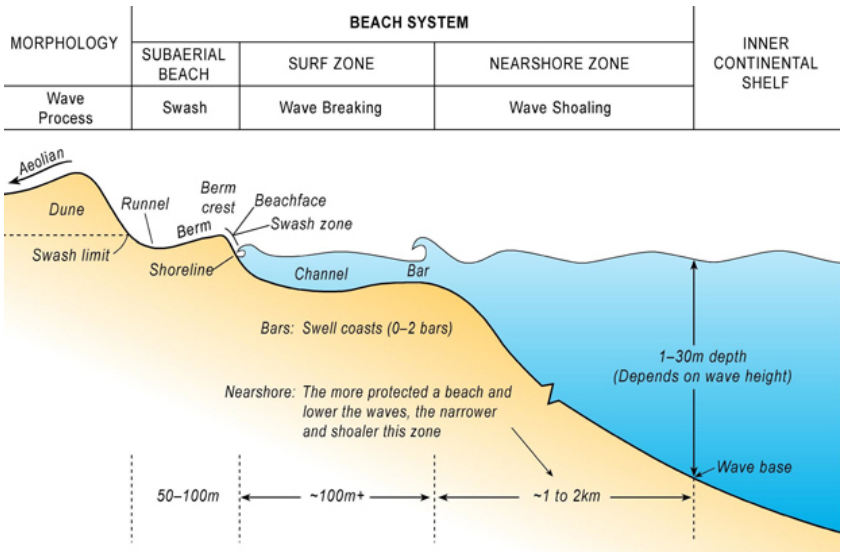

Figure 1.1: From Short (2012): *An idealised cross-section of a beach system*.

With regards to the sediment transport, field measurements have shown that the majority of sediment transport on a beach occurs in the swash zone (Beach and Sternberg, 1992). The high rate of sediment transport leads to morphological changes that determine the long-term evolution of the beach system. It is established that the bed shear stress plays a key role in the overall mechanics of sediment transport (Nielsen, 1992, 2002), but a thorough understanding of how the bed shear stress is distributed in the dynamic and transient swash flow is still lacking. Thus, because the swash zone is responsible for a high volume of sediment transport, and sediment transport models often rely on estimates of the bed shear stress, understanding the distribution of bed shear stresses in the swash is still a subject of active research. Further, laboratory studies remain a key feature of the study of swash flows since numerical solutions using non-linear shallow water equations face challenges due to the moving shoreline and wave breaking (Brocchini and Dodd, 2008) and numerical models used to complement measurements require calibration to the data to be able to predict flow depths and depth-averaged velocities with accuracy (Barnes *et al.*, 2009;

O'Donoghue *et al.*, 2010).

The wave conditions relevant to the nearshore region must be shallow water waves of finite amplitude, which can be concluded from Svendsen's useful definition of the nearshore region. The first theory and analytical solutions of such types of waves were due to Boussinesq (1872) and Korteweg and de Vries (1895): solitary waves and cnoidal waves. Solitary waves have been studied for various applications relating to the nearshore region: the study of integral properties (*e.g.*, total mass, energy, and impulse) of waves that have reached their maximum amplitude and will soon break (*e.g.*, Longuet-Higgins, 1974; Fenton and Rienecker, 1982), the understanding of the relative importance of terms modeling frequency dispersion and non-linear wave steepening, respectively, in the Boussinesq equations (*e.g.*, Peregrine, 1967; Hammack and Segur, 1978), the study of the influence of viscous effects or transition to turbulence in the bottom boundary layer on wave propagation (*e.g.*, Keulegan, 1948; Liu *et al.*, 2006, 2007; Sumer *et al.*, 2010; Seelam *et al.*, 2011), *etc.* Solitary waves were also used to study the run-up of tsunamis (*e.g.*, Goring, 1978; Synolakis, 1986; Li, 2000; Synolakis and Bernard, 2006; Madsen and Schäffer, 2010), although there may be certain shortcomings of using them to model tsunamis at the laboratory scale (Madsen *et al.*, 2008).

In fact, Madsen *et al.* (2008) calimed that solitary waves in the laboratory may be dynamically similar to wind waves at a beach, but this idea is not a new one. For example, Munk (1949) stated that: *because the energy of the solitary waves is largely confined within a relatively narrow band about the crest, it seems reasonable to apply the theory to periodic humping crests of ocean swell.* Solitary waves are also the fastest, most massive and have the highest impulse for all waves of the same

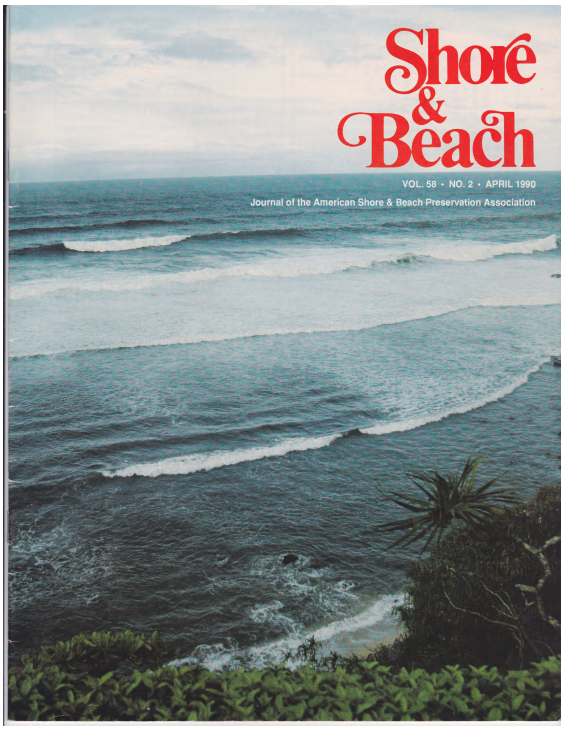

Figure 1.2: The cover of Shore & Beach, as part of Wiegel (1990); Galvin (1990), showing the transformation of long ocean swells into multiple wave crests that resemble solitary waves.

wave height (Longuet-Higgins, 1974; Fenton and Rienecker, 1982) and so provide useful upper bounds in the study of wind waves. Although quantitative evidence from the field for the existence of solitary waves approaching a beach is still lacking, observerations suggest that waves approaching a beach often resemble solitary waves (Peregrine, 1983). Wiegel (1990) and Galvin (1990) discussed some qualitative evidence for soliton fission, for example, when a long ocean swell is transformed by a reef and under goes fission into multiple wave crests that resemble solitary waves (see Figure 1.2). This process has also been studied more formally by Peregrine (1966); Madsen and Mei (1969); Mei (1989); El *et al.* (2012) and others, who all conclude that the transformation of a weak or undular bore on a slope and climbing onto a shelf results in multiple solitons.

Thus, although solitary waves have also been used as a canonical model to study the run-up of long waves (Pedersen and Gjevik, 1983; Synolakis, 1987; Synolakis and Skjelbreia, 1993; Zelt, 1991; Liu *et al.*, 1995; Lin *et al.*, 1999; Li and Raichlen, 2001, 2002, 2003; Jensen *et al.*, 2003, and others), the swash of solitary waves, which may be very relevant to the swash on natural beaches, has received only limited attention (*e.g.*, Kobayashi and Lawrence, 2004; Sumer *et al.*, 2011; Pedersen *et al.*, 2013).

1.2 Outline

Chapter 2 describes the design and development of a 'shear plate sensor' – a sensor to measure the bed shear stress of a flow by directly measuring the tangential force exerted by the flow on a small element, *i.e.*, the 'shear plate'. The mechanical design of the shear plate sensor is kept as simple as possible to increase its robustness in the complex swash flows, but a new solution is proposed to the old problem of how to handle flows with pressure gradients. Scaling arguments of the flow in the housing of the sensor underneath the shear plate lead to a simplified solution of the pressure distribution that is independent of the flow in mild pressure gradients, where the mildness of the pressure gradients is also quantified. The solution is tested under solitary waves in a small-scale laboratory flume. Pujara and Liu (2014) is a journal article based on the work in this chapter.

Chapter 3 presents the analytical and experimental investigation of the swash flow due to solitary waves when they climb a plane sloping beach. In a large-scale flume, where the beach slope is kept constant, ten wave cases are

examined that range from non-breaking waves to plunging breakers. The goal of the study is to elucidate how the breaker type, which is a qualitative property of the wave breaking that can nonetheless be predicted from the incident waves and beach slope, influences the swash. It is found that the classic solutions for the collapse of a 'fully-developed' bore climbing a beach as the water depth goes to zero and the ensuing swash flow are more widely applicable than previously thought. In short, the swash of breaking solitary waves is found to be equivalent to that of a breaking dam on a sloping bed and the flow evolution can be predicted by a single measurement: The velocity of the shoreline immediately after collapse of the bore/waveform or the wave height immediately before collapse. The values the peak bed shear stress in the swash also a dependency on the shoreline velocity following collapse. Finally, with the flow evolution in the swash known and the bed shear stress near the moving shoreline parameterized, the balance of forces of the fluid near the moving shoreline is considered and a solution found for the equations of motion. This solution is able to predict the motion of the shoreline in the initial stages of the swash, including the deceleration due to friction with the bed. The work from this chapter has been submitted as two manuscripts to the *Journal of Fluid Mechanics*, one of which (Pujara *et al.*, 2015) has already been accepted for publication.

While chapter 3 considers the swash due to a solitary wave climbing a beach of initially quiescent water, chapter 4 presents an experimental investigation of the flow due to two successive solitary waves, with a focus on characterization of the interaction between the successive waves on the beach. Swash-swash interactions can be classified into different qualitative categories and two interactions that fall into different categories are studied. The change of flow direction in the boundary layer when a wave approaching a beach encounters the

residual flow due to the swash of the previous wave is measured and described using the shear plate sensor and a bed pressure sensor. The reduction of run-up of the second wave is parameterized in terms of the breaker type of the first wave. Based on the work in this chapter, a manuscript has been submitted to the *Coastal Engineering* journal.

The remainder of this chapter provides an introduction to the theory of solitary waves.

1.3 Solitary waves

The solitary wave is a finite-amplitude elevation wave of permanent form that travels at a constant phase velocity. It was first observed and documented by Russell (1845), but it was not until Boussinesq (1872) and Korteweg and de Vries (1895) that the first equations to describe the dynamics of the solitary wave and the first analytical solution to the solitary wave became available (see Miles, 1980, for more details). This solution is known as the Boussinesq theory for the small-amplitude solitary wave, in which tthe free-surface displacement is given by

$$\eta(x,t) = H_0 \mathrm{sech}^2\left[K_0\left(x - c_0 t\right)\right], \tag{1.1}$$

where,

$$K_0 = \frac{1}{h_0}\sqrt{\left(\frac{3}{4}\epsilon_0\right)}, \tag{1.2a}$$

$$c_0 = \sqrt{g h_0 (1 + \epsilon_0)}. \tag{1.2b}$$

The wave height, H_0, and the stillwater depth, h_0, are sufficient to fully describe the wave and the dimensionless parameter, $\epsilon_0 = H_0/h_0$, represents the non-linearity of the wave. In the Boussinesq theory, terms of $O(\epsilon_0^2)$ or higher are ignored and the theory has been shown to provide results that agree with experiments up to $\epsilon_0 \approx 0.25$ (Dingemans, 1997). The horizontal velocity and the leading order vertical velocity are given by

$$u(x,z,t) = U_0 \text{sech}^2 \left[K_0 (x - c_0 t)\right], \tag{1.3}$$

$$w(x,z,t) = U_0 \sqrt{3\epsilon_0} \left(\frac{z + h_0}{h_0}\right) \text{sech}^2 \left[K_0 (x - c_0 t)\right] \tanh \left[K_0 (x - c_0 t)\right], \tag{1.4}$$

respectively. $U_0 = \epsilon_0 \sqrt{g h_0}$ is the maximum horizontal velocity and it occurs under the wave crest. The horizontal velocity is $O(\epsilon_0)$ whereas the leading order vertical velocity is $O(\epsilon_0^{3/2})$. The pressure in the water column is quasi-hydrostatic and given by

$$p(x,z,t) = -\rho g z + \rho g H_0 \text{sech}^2 \left[K_0 (x - c_0 t)\right]. \tag{1.5}$$

Although the wavelength and period of a solitary wave are infinite, following Madsen *et al.* (2008), an effective wavelength and an effective period can be defined, respectively, as

$$L_0 = \frac{2\pi}{K_0}, \quad T_0 = \frac{2\pi}{K_0 c_0}. \tag{1.6}$$

Grimshaw (1971) provided a higher order theory of solitary waves, where terms up to $O(\epsilon_0^2)$ are included. The Grimshaw theory gives the free-surface displacement of the solitary wave as

$$\eta(x,t) = H_0\left[s^2 - \frac{3}{4}\epsilon_0 s^2 q^2 + \epsilon_0^2\left(\frac{5}{8}s^2q^2 - \frac{101}{80}s^4q^2\right)\right], \tag{1.7}$$

where,

$$s = \operatorname{sech}\left[K_{0,G}\left(x - c_{0,G}t\right)\right], \tag{1.8a}$$

$$q = \tanh\left[K_{0,G}\left(x - c_{0,G}t\right)\right], \tag{1.8b}$$

$$K_{0,G} = \frac{1}{h_0}\sqrt{\left(\frac{3}{4}\epsilon_0\right)\left(1 - \frac{5}{8}\epsilon_0 + \frac{71}{128}\epsilon_0^2\right)}, \tag{1.8c}$$

$$c_{0,G} = \sqrt{gh_0\left(1 + \epsilon_0 - \frac{1}{20}\epsilon_0^2 - \frac{3}{70}\epsilon_0^3\right)}. \tag{1.8d}$$

The horizontal and vertical velocity are given by

$$\begin{aligned} u(x,z,t) = U_0\Bigg\{ & s^2 - \epsilon_0\left[-\frac{1}{4}s^2 + s^4 + \left(\frac{z+h_0}{h_0}\right)^2\left(\frac{3}{2}s^2 - \frac{9}{4}s^4\right)\right] \\ & - \epsilon_0^2\Bigg[\frac{19}{40}s^2 + \frac{1}{5}s^4 - \frac{6}{5}s^6 + \left(\frac{z+h_0}{h_0}\right)^2\left(-\frac{3}{2}s^2 - \frac{15}{4}s^4 + \frac{15}{2}s^6\right) \\ & + \left(\frac{z+h_0}{h_0}\right)^4\left(-\frac{3}{8}s^2 + \frac{45}{16}s^4 - \frac{45}{16}s^6\right)\Bigg]\Bigg\}, \end{aligned} \tag{1.9}$$

$$\begin{aligned} w(x,z,t) = U_0\sqrt{3\epsilon_0}\left(\frac{z+h_0}{h_0}\right)q\Bigg\{ & s^2 - \epsilon_0\left[\frac{3}{8}s^2 + 2s^4 + \left(\frac{z+h_0}{h_0}\right)^2\left(\frac{1}{2}s^2 - \frac{3}{2}s^4\right)\right] \\ & + \epsilon_0^2\Bigg[-\frac{49}{640}s^2 - \frac{17}{20}s^4 - \frac{18}{5}s^6 + \left(\frac{z+h_0}{h_0}\right)^2\left(-\frac{13}{16}s^2 - \frac{25}{16}s^4 + \frac{15}{2}s^6\right) \\ & + \left(\frac{z+h_0}{h_0}\right)^4\left(-\frac{3}{40}s^2 + \frac{9}{8}s^4 - \frac{27}{16}s^6\right)\Bigg]\Bigg\}, \end{aligned} \tag{1.10}$$

respectively. The pressure in the water column is given by (Fenton, 1972)

$$p(x,z,t) = -\rho g z + \rho g h_0 \epsilon_0 \left\{ s^2 - \epsilon_0 \left[\frac{3}{4}s^2 - \frac{3}{2}s^4 + \left(\frac{z+h_0}{h_0}\right)^2 \left(-\frac{3}{2}s^2 + \frac{9}{4}s^4\right)\right] \right.$$
$$+ \epsilon_0^2 \left[-\frac{1}{2}s^2 - \frac{19}{20}s^4 + \frac{11}{5}s^6 + \left(\frac{z+h_0}{h_0}\right)^2 \left(\frac{3}{4}s^2 + \frac{39}{8}s^4 - \frac{33}{4}s^6\right) \right.$$
$$\left. \left. + \left(\frac{z+h_0}{h_0}\right)^4 \left(\frac{3}{8}s^2 - \frac{45}{16}s^4 + \frac{45}{16}s^6\right)\right]\right\}. \tag{1.11}$$

Note, the leading order solution of Eq. (1.7)-(1.11) reduces to the Boussinesq solution, Eq. (1.1)-(1.5). Further higher order solutions of the solitary wave are also available (*e.g.*, Fenton, 1972; Longuet-Higgins and Fenton, 1974) and Tanaka (1986) gives a fully non-linear solution in integral form.

A Reynolds number associated with the solitary wave can be defined using the Boussinesq solution, Eq. (1.1)-(1.5). Following Sumer *et al.* (2010), this Reynolds number is given by

$$Re_0 = \frac{a_0 U_0}{\nu}. \tag{1.12}$$

The lengthscale, $a_0 = U_0/(K_0 c_0)$, is the half-excursion length for a water particle and ν is the kinematic viscosity of water.

1.3.1 Generation of solitary waves in the laboratory

Goring (1978) developed a theory for the generation of long waves of permanent form that propogate at a constant phase velocity using a vertical piston-

type wavemaker. The wavemaker velocity, $d\xi_{wm}/dt$, is matched to the depth-averaged horizontal water particle velocity, $\overline{u}(x,t)$, since the vertical variation of horizontal water particle is weak for long waves. This formulation gives

$$\frac{d\xi_{wm}}{dt} = \overline{u}(\xi_{wm}, t). \tag{1.13}$$

The above equation is a non-linear differential equation due to the fact that the horizontal velocity is evaluated at the wavemaker position, ξ_{wm}. Eq. (1.13) is solved numerically with a fourth-order Runge-Kutta algorithm using $\overline{u}(x,t) = c_0\eta/(h_0+\eta)$, where c_0 and η are described by the Boussinesq solution to the solitary wave (Synolakis, 1990).

CHAPTER 2

SHEAR PLATE SENSOR

2.1 Introduction

The wall shear stress is an important quantity in any wall-bounded flow and its measurement has been widely discussed in the literature (*e.g.*, Winter, 1979; Hanratty and Campbell, 1996). Methods for the measurement of wall shear stress can be broadly classified into two catagories: direct and indirect (Haritonidis, 1989). Indirect methods rely on correlating flow properties to the shear stress at the wall using established assumptions of the near-wall flow. Examples include the Preston tube, the Clauser chart, heat transfer probes, mass transfer probes *etc.* On the other hand, direct methods measure the force exerted by the shear stress of the fluid on a separated section of the wall that is surrounded by a small gap. Thus, in principle, the direct method does not require any information regarding the flow, but it faces other challenges that are discussed below.

The flow in the nearshore region driven by wave action is characterized by shallow depths, entrained air due to wave breaking, transient behaviour and boundary layer flow reversals, all of which pose signficant challenges to the use of indirect methods. Nonetheless, there are examples in the literature that report measurements of the bed shear stress in this flow environment. Cox *et al.* (1996), Cowen *et al.* (2003), and others have obtained estimates of the bed shear stress in the nearshore region from measurements of phase-averaged velocity profiles, which were fitted to a logarithmic law of the wall. Sumer *et al.* (2011, 2013) used hot-film sensors to measure the bed shear stress under plunging breakers, but

the direction of the bed shear stress had to be determined from additional velocity measurements very close to the bed. The calibration of hot-film probes also makes certain assumptions about the structure of the flow very close to the bed (Ling, 1963) so that an *in situ* calibration was needed. For recent developments on indirect methods, see Fernholz *et al.* (1996).

Sensors using the direct measurement method, referred to as shear plate sensors in the context of coastal engineering, are more robust to the challenges of nearshore coastal flows. Shallow depths, presence of air bubbles, flow reversals, *etc.* are handled more easily and the sensor can also be easily designed to distinguish the direction of stress. Examples of studies using a shear plate sensor in oscillatory or wave-driven flow include Riedel and Kamphuis (1973); Simons *et al.* (1992, 1994); Rankin and Hires (2000); Mirfenderesk and Young (2003); Boers (2005); You and Yin (2007) and Seelam *et al.* (2011). Barnes *et al.* (2009) also used a shear plate sensor to measure bed shear stress in a bore driven swash flow. For a recent survey of the many direct measurement sensors used in other types of flows, see Kolitawong *et al.* (2010).

To study the flow of solitary waves in the surf and the swash zones, accurate measurements of the bed shear stress were required. For this purpose, a new shear plate sensor was designed and built and this chapter describes the development of that shear plate sensor.

2.2 Design

2.2.1 General considerations

The compromises and difficulties in the design of shear plate sensors have been summarized by Winter (1979). Those relevant to the present design are:

1. Transducing small forces or deflections, and the compromise between local measurement and having a large enough shear plate area so that the force on it can be accurately measured.
2. The effect of the necessary gaps around the shear plate.
3. The secondary force due to pressure gradients.
4. The secondary forces due to misalignments.

For the first item on the list, the design compromise is between the size of the sensor and the desire to measure forces accurately: smaller sensors provide more local measurements but produce smaller forces that need to be measured. If the sensor is passive, where the shear force of the fluid is measured by measuring the deflection rather than an active sensor that measures the force required to keep the shear plate position constant, the size of the gaps is determined by the stiffness that provides resistance to shear plate deflection. The size of the gaps surrounding the shear plate should be as small as possible to cause minimal disturbance to the flow and to minimize flow circulation through the sensor but to be large enough so that deflections of the shear plate sensor can be measured accurately. The third item on the list refers to the force due to a difference in pressure between the upstream and downstream edges of the shear

plate. This issue is considered a fundamental limitation of shear plate sensors, especially in wave-driven flows where pressure gradients are significant. For a given size of the shear plate top surface, the force due to pressure gradients is minimized by minimizing the shear plate thickness so that the pressure difference acts on a smaller area. The fourth item on the list is also important in this consideration because as dimensions of the sensor and gaps become smaller, the tolerances in construction also need to decrease so that misalignments are minimized. Therefore, the designs of the shear plate size, gap size and stiffness are not independent.

2.2.2 Current design

The current sensor design is motivated by the study of the nearshore region in small-scale and large-scale laboratory wave flumes, where the range of values of the bed shear stress can span $O\left(10^{-1}\right)$ – $O\left(10^{2}\right)$ Pa. The flow is primarily two-dimensional, varying in the $x-$ (cross-shore) and $z-$ (vertical) directions but with negligible variation of the mean flow in the spanwise (long-shore) direction of the flume. To obtain a local, phase-resolved measurement of the bed shear stress, the length of the shear plate in the cross-shore direction needs to be much smaller than $O\left(1\right)$ m, the typical lengthscale of waves in laboratory flumes, and the time response of the sensor needs to be much faster than $O\left(1\right)$ s, the typical period of waves in laboratory flumes.

To satisfy the various design constraints while also maintaining a design simple enough to allow manual construction in the machine shop, a configuration that uses an eddy-current proximity probe, which is able to measure small

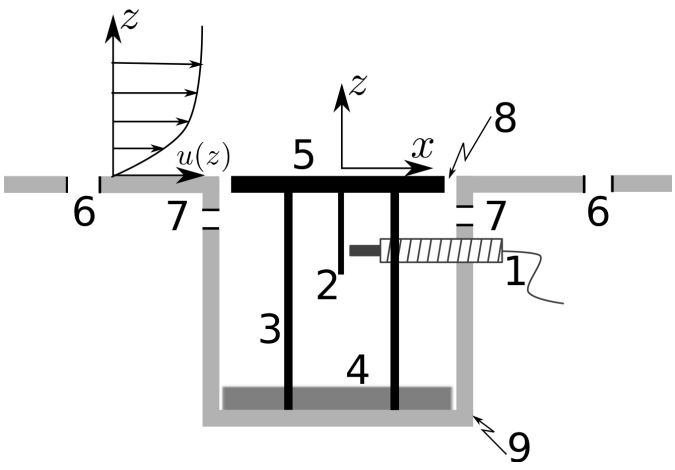

Figure 2.1: Schematic of the shear plate sensor design. *1*: eddy-current proximity sensor; *2*: target plate; *3*: cylindrical links; *4*: base plate; *5*: shear plate; *6*: external pressure tappings; *7*: chamber pressure tappings; *8*: gap; *9*: acrylic housing.

deflections with high accuracy, combined with a structural linkage mechanism that provides stiffness against the shear force of the fluid, was used following the designs of Simons *et al.* (1992); Mirfenderesk and Young (2003); Boers (2005) and Barnes *et al.* (2009). A schematic for the current shear plate sensor is shown in Figure 2.1. The shear plate is made of brass (alloy 260) and it is of length 43.0 mm, width 136.0 mm and thickness 0.8 mm, where the length is the dimension in the streamwise direction. It is rigidly attached to 4 cylindrical brass (also alloy 260) links of diameter 1.6 mm and length 62.2 mm. The bottom ends of the cylindrical links are rigidly clamped to an aluminium base plate of thickness 6.4 mm. Such a configuration creates a parallel linkage mechanism, which provides stiffness to the shear plate deflections in the horizontal direction and support in the vertical direction. This type of mechanism also minimizes the tilting of the shear plate from small deflections in the horizontal direction. The mechanism is installed into an acrylic housing via bolts through the aluminium base plate such that the top surface of the shear plate is flush with the top surface of the

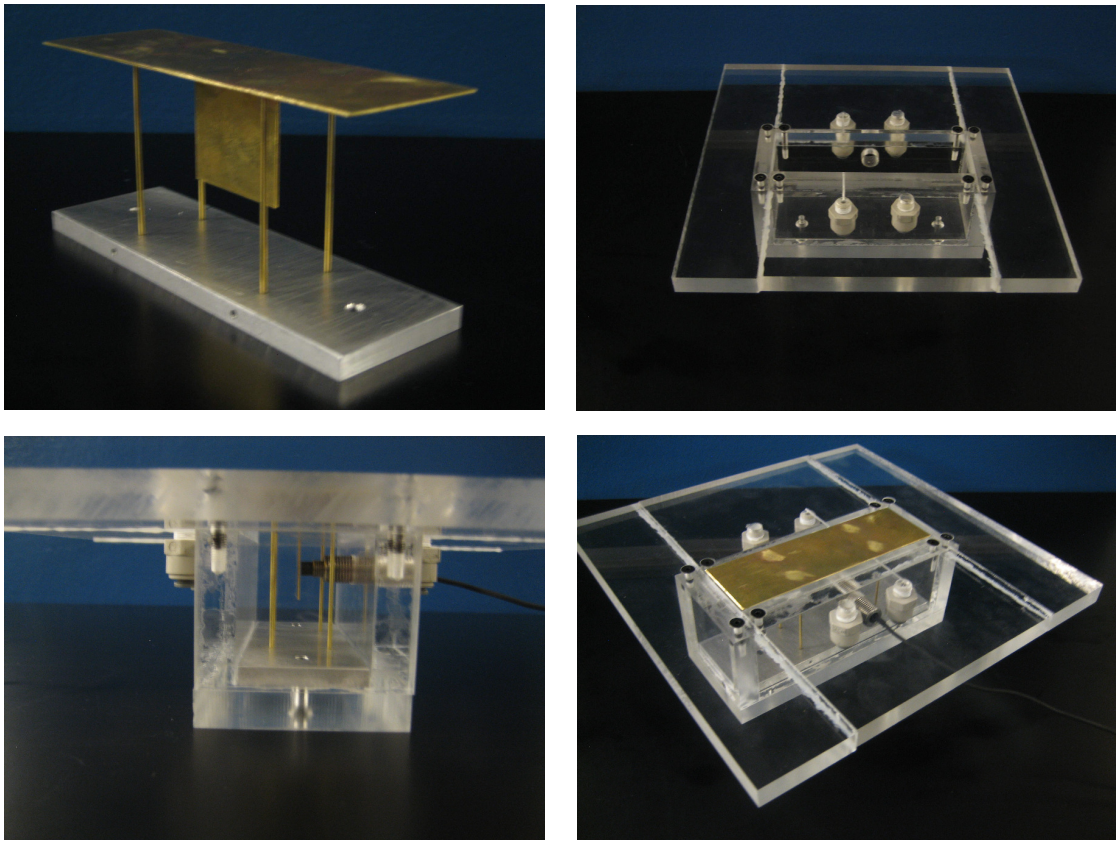

Figure 2.2: Photographs of the shear plate sensor. *Top left*: parallel linkage mechanism; *top right*: acrylic housing; *bottom left*: side view of shear plate sensor assembly; *bottom right*: isometric view of shear plate sensor assembly.

acrylic housing. The deflection of the shear plate in the horizontal direction is detected by an eddy-current proximity probe (Lion Precision ECL-202, probe U8), which measures the distance to a small vertical target plate rigidly attached to the bottom face of the shear plate. The eddy-current proximity probe has a range of 2 mm with a resolution of 0.001 mm. There exists a small gap of 1 mm along the perimeter of the shear plate between the shear plate and the housing to allow for small deflections. The acrylic housing can in turn be installed into laboratory flumes with the top surface flush with the flume bottom. Additionally, there are 2 pairs of pressure tappings to enable measurement of pressure

gradients above the shear plate (external pressure tappings) and underneath the shear plate (chamber pressure tappings). The external pressure tappings are of diameter 6.4 mm, located 95.4 mm apart equidistant from the centerline of the shear plate. The chamber pressure tappings are of diameter 1.2 mm located 45.0 mm apart on the side walls of the chamber under the shear plate. The centre of the chamber pressure tappings is 1.8 mm below the top surface of the shear plate. Figure 2.2 shows photographs of the shear plate sensor.

2.3 Calibration

The convert measurements of the shear plate displacement to force under time-varying loading, it is necessary to know both the static and dynamic response of the parallel linkage mechanism. To study its response, the mechanism is modeled as a linear, second-order lumped parameter system of a mass, spring and dashpot. The equation of motion for this system (*e.g.*, den Hartog, 1956) is

$$\frac{\ddot{\chi}}{\omega_n^2} + 2c\frac{\dot{\chi}}{\omega_n} + \chi = \frac{F}{k}, \tag{2.1}$$

where F is the total force on the shear plate in the x-direction, χ is the deflection in the x-direction and the dot notation refers to differentiation with respect to time. For such a system, the natural frequency of oscillation is given by $\omega_n = \sqrt{k/m}$, where m is the mass of the shear plate, k is the stiffness constant. The damping ratio is given by $c = \lambda/(2\sqrt{km})$, where λ is the dashpot constant, and the damped natural frequency is given by $\omega_d = \omega_n\sqrt{1-c^2}$.

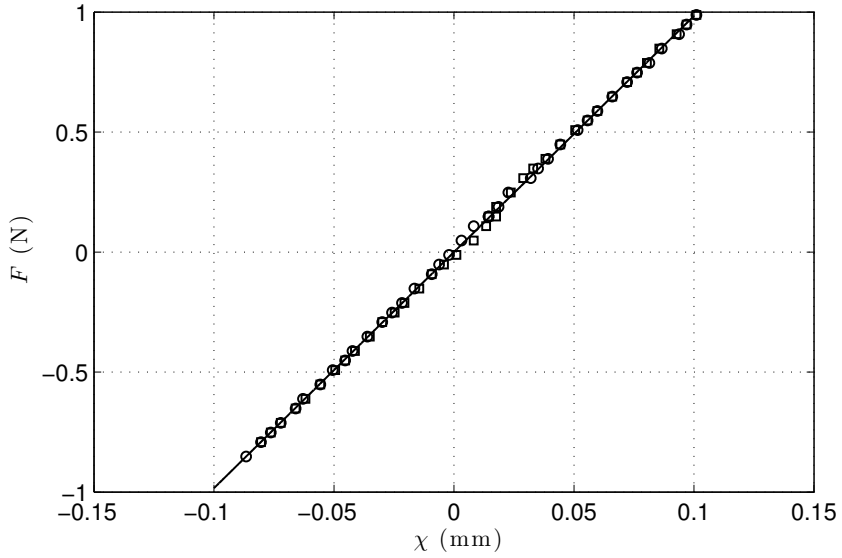

Figure 2.3: Typical data for shear plate sensor stiffness measurement. ∘, increasing load; □, decreasing load; ——, linear fit.

2.3.1 Static response

Measuring the static response of the system amounts to measuring the stiffness constant, k, of the parallel linkage mechanism under steady loading. The stiffness constant was measured by applying known forces and recording displacements. Two methods of applying forces were used. The first method used a weights-and-pulley system and the second method used a spring force meter. Figure 2.3 shows the data from a typical stiffness measurement. The two methods were used to measure stiffness many times over the course of the duration of all the experiments reported in this thesis. The final value of the stiffness constant, k, used in the analysis was derived from performing a linear regression on all the combined data and the uncertainty was derived from using the bootstrap method (Efron and Tibshirani, 1993) on the residuals. The result was that $k = 9800 \pm 100\ \mathrm{Nm}^{-1}$ at the 95% confidence interval.

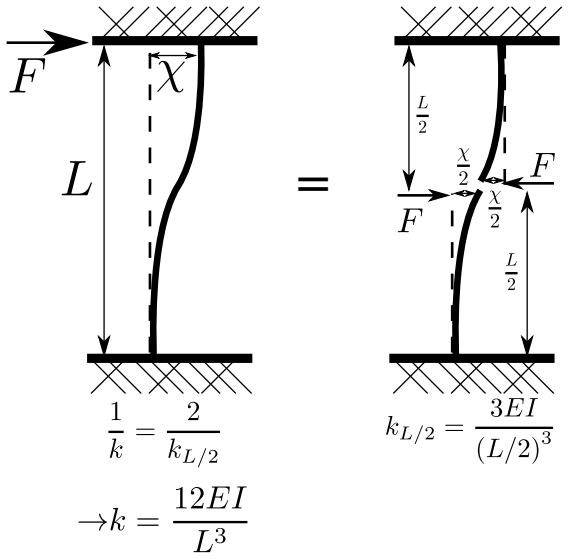

Figure 2.4: The stiffness of a clamped guided beam.

The measured value of the stiffness constant can be compared to the expected stiffness by analysing the mechanism using simple beam structural mechanics since the deflections are small compared to the length of the links. The links will deflect as clamped guided beams maintaining a right angle to the shear plate as well as to the base plate (see Figure 2.4). The stiffness of a cantilevered beam with one moment-free end is given by $3EI/L^3$, where E is the Young's Modulus of the material, I is the second moment of area of the cross-section of the beam and L is the length of the beam. A clamped guided beam is equivalent to two cantilevered beams of half the length each and so a clamped guided beam has a stiffness four times in magnitude to that of a cantilevered beam of the same dimensions (see Figure 2.4). The expected stiffness of four links acting in parallel is given by $48EI/L^3$. Using the Young's Modulus for brass as $E = 110$ GPa, the second moment of area of the cylindrical links as $I = \pi D^4/64$, where the links are of diameter D, the expected stiffness of the four links acting in parallel is calculated as 9900 N/m. The predicted value and the measured value agree to within the level of uncertainty.

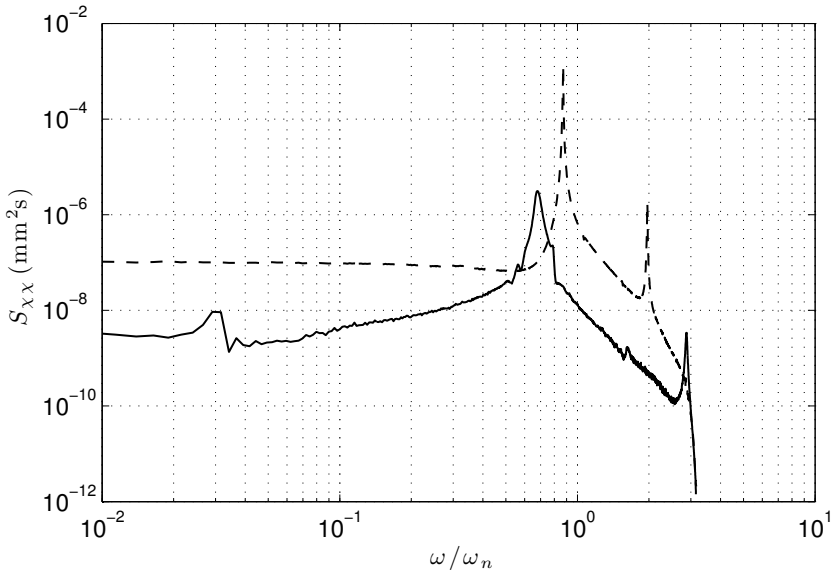

Figure 2.5: Power spectral density function of impulse response in air and in water. The natural frequency is 79 Hz; the reflected portion of the spectra are not plotted. ——, water; — —, air.

The range of the shear plate sensor, calculated by the maximum force applied in the calibration divided by the area of the top surface of the shear plate, is ±200 Pa. The accuracy of the shear plate sensor due to the combined uncertainty in the measurement of shear plate displacement (resolution of eddy-current proximity probe) and the uncertainty in the stiffness of the parallel linkage mechanism is combined using a root-sum-square combination (Taylor, 1997) to be ±1%.

2.3.2 Dynamic response

To measure the dynamic response of the parallel linkage mechanism, its impulse response was measured in two media: air and water. The shear plate was given a small impulse by hand with a hammer and the shear plate oscil-

lations were recorded at a sampling frequency of 500 Hz until they died out. The power spectral density fuction of the impulse response, $S_{\chi\chi}$, is plotted in Figure 2.5 against frequency made dimensionless by the undamped natural frequency. The undamped natural frequency was estimated at 79 Hz using the measured stiffness, k = 9800 Nm^{-1}, and mass of the shear plate plus the four links, m = 0.040 kg. The locations of the peaks in Figure 2.5 indicate values of the damped natural frequencies, which were found to be 69 Hz and 54 Hz for air and water, respectively and the corresponding damping ratio, c, was found to be 0.49 and 0.73 for air and water, respectively. Using this information, the harmonic response of the mechanism can be computed using Eq. (2.1). For water, the bandwidth of the shear plate sensor, *i.e.*, the frequency where the output of the sensor falls to -3 dB of the forcing input was found to be 75 Hz.

2.4 Secondary forces

Apart from the force created by the shear stress of the flow over the top surface of the shear plate, there are additional, secondary, forces experienced by the shear plate that may cause an error in the measurement of bed shear stress. The most significant of these secondary forces is the force due to pressure gradients. The next section provides a method to account for this force if the streamwise pressure gradient in the flow is mild enough.

2.4.1 Correction for the force due to pressure gradients

The force on the shear plate due to a streamwise pressure gradient is illustrated in Figure 2.6: the streamwise pressure gradient caused by a tilting free-surface creates, for example, a higher pressure on the upstream edge of the plate compared to the downstream edge. As previously mentioned, the existance of this secondary force is a severe limitation on the applicability of shear plate sensors in wave-driven flows, and this force must be accounted for to avoid large errors in measurement of bed shear stress. There have been solutions previously suggested to avoid this issue. For example, Frei and Thomann (1980) filled the gaps and chamber with a denser fluid in their sensor, which was designed to make measurements in wind tunnels. However, this introduces additional surface tension forces, which, in the current design, would change the dynamic response of the sensor and significantly reduce its bandwidth. The results would be similar if the gap is sealed by any kind of elastic membrane. Therefore, to preserve a fast dynamic response of the shear plate sensor, the gaps and chamber are left open, and in such a case, an estimate for the ratio of the pressure gradient force to the shear force is given by the expression $\alpha l_{pt}/u_\tau^2$, where l_{pt} is the shear plate thickness, $\alpha = |(1/\rho)\,\partial p/\partial x|$ is the magnitude of the kinematic pressure gradient (or alternatively, the free stream acceleration), and $u_\tau = \sqrt{\tau_b/\rho}$ is the friction velocity of the flow. The error due to the pressre gradient force is negligible if $\alpha l_{pt}/u_\tau^2 \ll 1$. However, in laboratory wave-driven flows, $\alpha l_{pt}/u_\tau^2$ can be $O(1)$.

The precise value of the pressure gradient force experienced by the shear plate is expected to be of lower magnitude than $|\partial p/\partial x|\, V_{sp}$, where V_{sp} is the shear plate volume, as pointed out by Brown and Joubert (1969), Riedel and

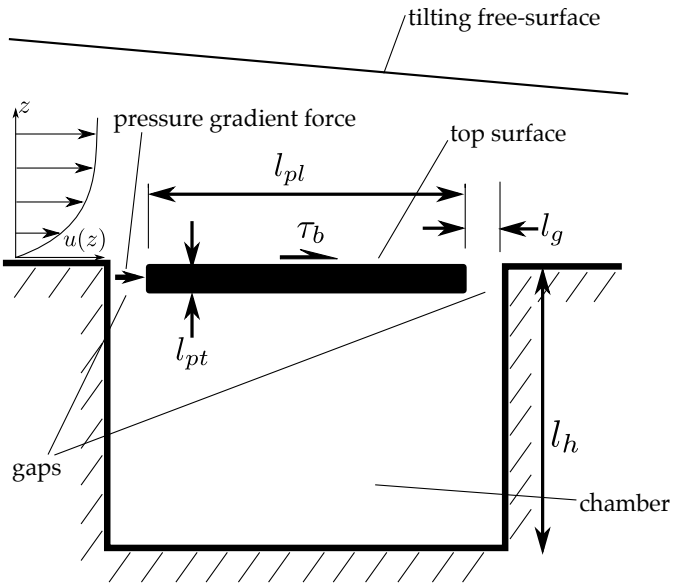

Figure 2.6: Schematic of the forces on the shear plate.

Kamphuis (1973), and others. The constriction of the gaps forces the pressure gradient to decay through the gaps and in the chamber from its external flow value. Thus, it is insufficient to measure just the external pressure gradient to correct for the pressure gradient force; it is also necessary to know the rate of pressure gradient decay. To account for this decay, we introduce an effective pressure gradient that acts on the shear plate: let f_{pg} denote the effective fraction of the external flow pressure gradient felt by the shear plate. From the value of f_{pg} and measurements of the external flow pressure gradient, the bed shear stress is obtained by

$$\tau_b = \frac{1}{A_{sp}} \left(F - f_{pg} \frac{\partial p}{\partial x} V_{sp} \right), \tag{2.2}$$

where A_{sp} is the shear plate top surface area. The concept of f_{pg} has been previously introduced by Coles (1953); Brown and Joubert (1969); Riedel and Kamphuis (1973); Allen (1977); Acharya *et al.* (1985), *etc.* Some of these studies (*e.g.*,

Coles, 1953; Brown and Joubert, 1969; Allen, 1977; Acharya *et al.*, 1985) assume $f_{pg} = 0.5$ by the following reasoning: the pressure gradient decays linearly from its external value at the shear plate top surface to a value of zero at the shear plate bottom surface and the fluid in the chamber is at the average pressure of the upstream and downstream gaps. Alternatively, a commonly employed method to estimate the value of f_{pg} uses measurements of pressure difference at the shear plate top surface and at some vertical distance below the shear plate top surface to estimate pressure gradients at those two vertical locations. Then the value of f_{pg} is calculated assuming a linear decay in pressure gradient between the two vertical locations. Such a method is employed by Riedel and Kamphuis (1973); Allen (1977) and Seelam *et al.* (2011). However, the most likely scenario is that the value of f_{pg} falls in the range $0.5 < f_{pg} < 1$, depending upon on how constricted the flow through the gaps and chamber is.

In what follows, a simplified analysis for the flow through the gaps and chamber of the shear plate sensor is presented in order to estimate the value of f_{pg}. The following assumptions are made: (i) deflections of the shear plate are ignored since they are small and do not have a large effect on the flow; (ii) the flow field is assumed to be invariant in the spanwise direction so that only the two-dimensional flow field is considered; (iii) the value of the external pressure gradient remains constant over the shear plate top surface; (iv) the pressure above the gaps is not modified by local flow perturbations due to a small flow through the sensor, *i.e.*, the flow through the sensor is essentially forced by the external flow without any coupling between the external flow and flow through the sensor. Thus, the boundary conditions for the flow in the chamber are known and it is implied that the flow velocities in the chamber are small. This last assumption is required if the shear plate is non-intrusive to the exter-

nal flow. The flow through the sensor is analyzed by introducing the following dimensionless quantities:

$$\tilde{\mathbf{u}} = \frac{\mathbf{u}}{U_{ch}};\ \tilde{t} = \frac{t}{T};\ \tilde{\nabla} = l_g \nabla;\ \tilde{p} = \frac{p}{\rho \alpha l_g}, \tag{2.3}$$

where U_{ch} is the velocity scale in the sensor chamber, T is the relevant timescale of the external flow, l_g is the size of the gap as defined in Figure 2.6, $\alpha = |(1/\rho)\,\partial p/\partial x|$ is the magnitude of the kinematic pressure gradient in the external flow. The chamber flow pressure gradients scale with the external flow pressure gradient since it is assumed that the external pressure gradient drives the flow in the chamber. The dimensionless momentum equation is then given by

$$\frac{l_g^2}{\nu T}\frac{\partial \tilde{\mathbf{u}}}{\partial \tilde{t}} + \frac{U_{ch} l_g}{\nu}\tilde{\mathbf{u}} \cdot \tilde{\nabla}\tilde{\mathbf{u}} = \frac{\alpha l_g^2}{\nu U_{ch}}\tilde{\nabla}\tilde{p} + \nabla^2 \tilde{\mathbf{u}}. \tag{2.4}$$

With the intention of linearising the equation, and under the assumption that the velocities in the chamber are small due to viscous forces in the chamber flow and mild pressure gradients in the external flow, the order of the chamber velocity scale is derived by requiring that the viscous term be of the same order as the pressure gradient term. This gives

$$U_{ch} = O\left(\frac{\alpha l_g^2}{\nu}\right). \tag{2.5}$$

The above is consistent with the intuition for the order of the chamber velocity scale, *i.e.*, $U_{ch} = U_{ch}\left(\alpha,\ l_g,\ \nu\right)$. Using this order of the chamber velocity scale, the importance of the non-linear term in Eq. (2.4) can be evaluated by the magnitude of its coefficient, the chamber flow Reynolds number, Re_{ch}, given by

$$Re_{ch} = \frac{\alpha l_g^3}{\nu^2}. \tag{2.6}$$

If $Re_{ch} \ll 1$, the non-linear advective acceleration can be neglected and the difficulty in determining the value of f_{pg} greatly reduced by taking the divergence of the remaining terms in Eq. (2.4) and invoking continuity to reveal that the pressure in the chamber follows Laplace's equation

$$\tilde{\nabla}^2 \tilde{p} = 0. \tag{2.7}$$

The boundary conditions for Eq. (2.7) are the Dirichlet boundary conditions above the gaps prescribed by the external pressure gradient and the Neumann boundary conditions at the walls such that the wall normal pressure gradient is zero, implying that the pressure gradient in the chamber simply scales with the external pressure gradient and its decay depends only on the dimensions of the sensor. The Neumann boundary condition follows directly from the kinematic no-flux boundary condition for velocity. Therefore, to calculate the value of f_{pg}, an aribitrary pressure gradient can be imposed above the shear plate by imposing different pressures above the upstream and downstream gaps. The pressure field in the chamber is then obtained via a numerical solution to Eq. (2.7). From the solution to the pressure field, the vertical variation of the pressure gradient over the thickness of the plate can be calculated and the value of f_{pg} is simply the average pressure gradient felt by the shear plate divided by the external pressure gradient imposed above the shear plate. This method for calculating f_{pg} is extremely convenient since its value is independent of the flow and therefore only needs to be calculated once for a given sensor design.

Eq. (2.7) was solved numerically using a second-order accurate finite difference scheme. Figure 2.7 shows the numerical solution for the pressure, p, for the dimensions of the shear plate sensor: $l_g = 1.0$ mm, $l_{pl} = 43.0$ mm, $l_{pt} = 0.8$ mm, $l_h = 55.0$ mm. The grid size was the same in both x- and z-directions so that $\Delta x = \Delta z = 0.1$ mm, which was ten times smaller than the gap size. A dimensionless pressure of 1 was imposed above the left gap and a dimensionless pressure of 0 above the right gap. The value of f_{pg} calculated from the pressure field gives $f_{pg} = 0.8$ to 1 significant figure. Successively refining the grid from $\Delta x = \Delta z = 0.2$ mm to $\Delta x = \Delta z = 0.05$ mm showed that the value of f_{pg} did indeed converge to $f_{pg} = 0.8$ to 1 significant figure.

The value of f_{pg} will vary with the dimensions of the sensor. There are three dimensions of the sensor that are important: l_g, l_{pt}, l_{pl}. The variations of l_h are considered unimportant provided that $l_h = O\left(l_{pl}\right)$. Therefore, from dimensional considerations,

$$f_{pg} = f_{pg}\left(\frac{l_{pt}}{l_g}, \frac{l_g}{l_{pl}}\right). \tag{2.8}$$

The functional relationship in Eq. (2.8) was established by calculating the values of f_{pg} for different ratios of l_{pt}/l_g and l_g/l_{pl}, keeping $l_h/l_{pl} = 1$, via numerical solutions to Eq. (2.7). Figure 2.8 shows the results: the variation of f_{pg} with the shear plate thickness to gap size ratio, l_{pt}/l_g, and gap size to shear plate length ratio, l_g/l_{pl}. The value of f_{pg} tends to decrease towards 0.5 as the thickness to gap size ratio is increased, whereas increasing the gap size to shear plate length ratio, while holding the shear plate thickness to gap size ratio constant, also reduces the value of f_{pg}. The trends of the results are the same as those observed by Acharya *et al.* (1985), who studied the variation of the value of f_{pg}

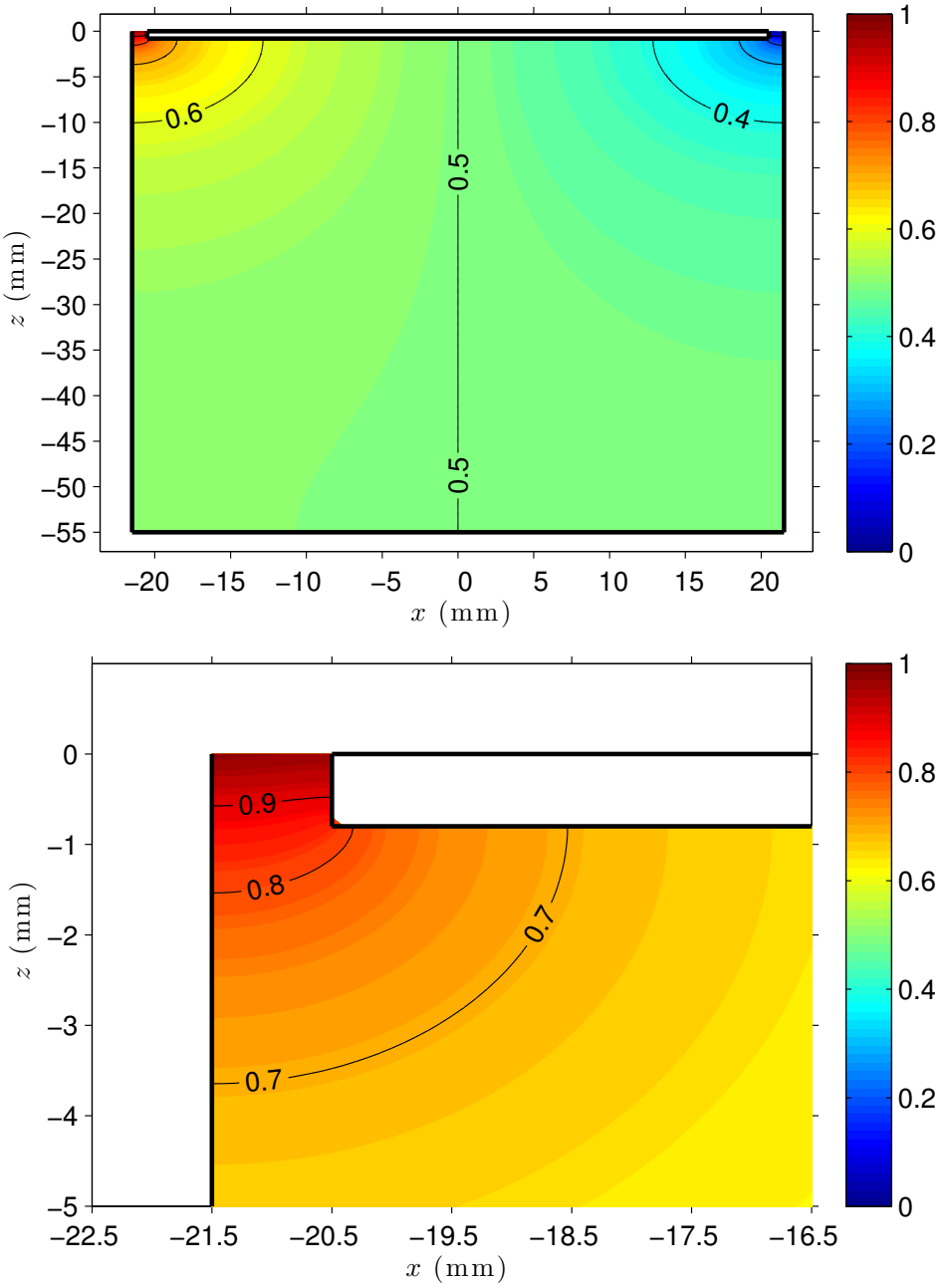

Figure 2.7: Numerical solution to Eq. (2.7) for pressure field in sensor chamber. l_g = 1.0 mm, l_{pl} = 43.0 mm, l_{pt} = 0.8 mm, l_h = 55.0 mm, $\Delta x = \Delta z$ = 0.1 mm. p = 1 above left gap, p = 0 above right gap. *Top*: entire chamber; *bottom*: zoomed into top left corner.

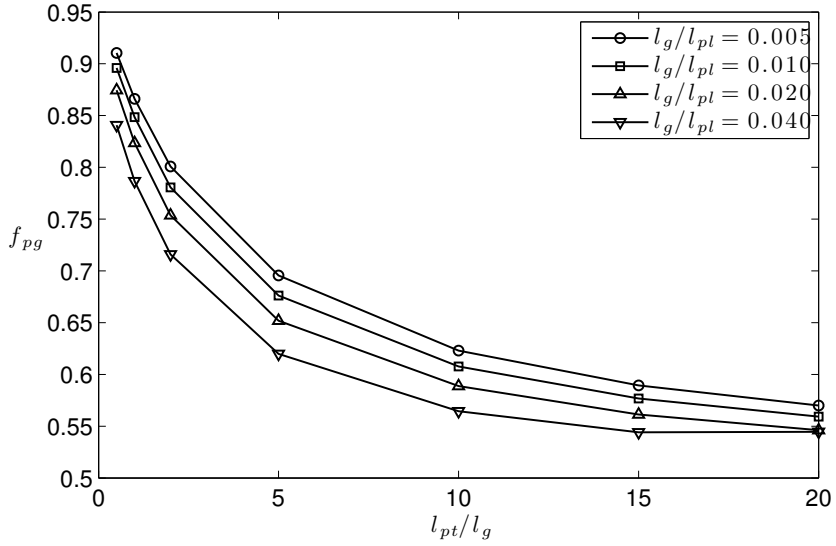

Figure 2.8: Variation of the value of f_{pg} with l_{pt}/l_g and l_g/l_{pl}.

experimentally by constructing multiple sensors and making measurements in fully-developed turbulent boundary layers with variable pressure gradients in wind tunnel experiments. A direct comparison to their data is not possible because their shear plate was circular, which introduces variations with anlgular position.

2.4.2 Misalignments and intrusiveness

Misalignment of the shear plate relative to the rest of the bed can add extra forces to the shear plate. Small protrusions, recessions and shear plate rotations can create complex flow patterns that add extra forces (*e.g.*, stagnation points for streamlines). Such extra forces can be large if the misalignments are large, but due to their complexity, it is not generally possible to correct for them. Allen (1977, 1980) and Kolitawong *et al.* (2010) discuss this matter further. The shear plate sensor was constructed to minimize these errors by the use of a parallel

linkage mechanism that minimizes shear plate tilting and by careful construction so that the top surface of the shear plate is aligned with the surrounding acrylic housing. Measurements of this alignment using a vertical test dial indicator revealed that the misalignment around the perimeter of the shear plate was everywhere smaller than 0.2 mm.

There may also be secondary forces on the shear plate due to non-zero chamber velocities and the exchange of momentum between the external flow and the chamber (Brown and Joubert, 1969). The accompanying velocity perturbations may also disturb the boundary layer flow and alter the local bed shear stress. Dhawan (1953) argued that the intrusion due to the gaps is small if the gap size is of the order of the viscous lengthscale, or equivalently, that the Reynolds number based on the gap size and friction velocity is $O(1)$. This Reynolds number is defined as

$$l_{g+} = \frac{u_\tau l_g}{\nu}. \tag{2.9}$$

However, Dhawan's experiments in turbulent boundary layers over gaps showed that, as an empirical guideline, the local bed shear stress is unaltered by the presence of the gaps up to $l_{g+} < 100$.

2.5 Experimental validation

The shear plate sensor was experimentally validated in two different flow conditions: a flat plate turbulent boundary layer and a laminar boundary layers under a solitary wave. The first flow is a canonical turbulent flow that has neg-

ligible pressure gradients whereas the second flow is a typical example of a flow driven by pressure gradients that remains laminar. To obtain independent measurements of the bed shear stress, particle image velocimetry (PIV) measurements were made in the flat plate turbulent boundary layer, whereas the results of PIV measurements and solutions to linearized boundary layer equations from Park (2009) were used in the solitary wave boundary layer.

In both sets of experiments, flow visualizations were conducted where coloured dye was used to check whether the shear plate sensor suffered from large velocities through the gaps. No significant perturbations were observed and thus the shear plate sensor was concluded to be non-intrusive to the external flow.

The validation experiments covered did not cover the full range of bed shear stress that the shear plate sensor is capable of measuring, but given that the shear plate sensor was designed for flow environments that are not well-understood and challenge other measurement techniques, it was not possible to generate a flow in which high values of bed shear stress measurable by the shear plate sensor could be verified by independent measurements. Furthermore, given that the dynamics of the shear plate sensor are well-understood, the experimental validation of the sensor is most crucially required at low values of bed shear stress, where the sensor is most prone to errors.

2.5.1 Flat plate turbulent boundary layer

Unidirectional flow was established in an 8 m long open channel flume with glass side walls and an acrylic bed in the DeFrees Hydraulics Laboratory at Cor-

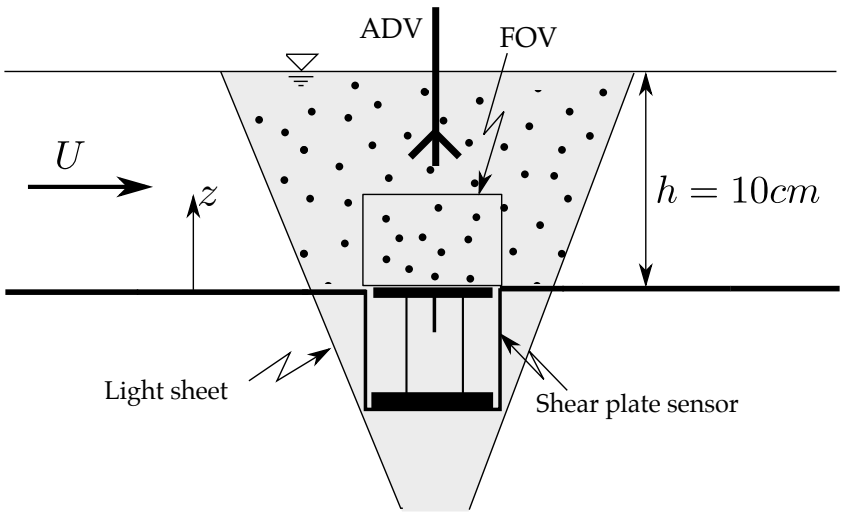

Figure 2.9: Schematic of the setup of flat plate turbulent boundary layer experiments.

nell University. Simultaneous measurements of the bed shear stress were made using the shear plate sensor and using the velocity data from particle image velocimetry (PIV) measurements. The setup of the experiment is shown in Figure 2.9. The shear plate sensor and the PIV field of view (FOV) coincided in the streamwise direction, allowing for a direct comparison of the bed shear stress, but were slightly separated in the spanwise direction. Both the shear plate sensor and the PIV FOV were sufficiently far from the side walls to be unaffected by the side wall boundary layer. Also at the same streamwise location, but separate spanwise location, was an acoustic doppler velocimeter (ADV, Nortek Vectrino with plus firmware), which was used to measure the mean flow velocity. Six separate tests were conducted at different mean flow velocities. The results are summarized in Table 2.1.

The FOV was illuminated by a dual-head Spectra Physics Nd:YAG laser operating at 10 Hz for each head, allowing for 10 Hz velocity data. The laser beams were expanded into a vertical light sheet using a cylindrical lens. The

Test	U (ms^{-1})	Re_θ (-)	$u_{\tau,1} \pm 95\%$ CI ($cm\ s^{-1}$)	$u_{\tau,2} \pm 95\%$ CI ($cm\ s^{-1}$)
U1	0.33	910	1.72 ±0.01	1.72 ±0.01
U2	0.40	1120	1.97 ±0.01	2.11 ±0.01
U3	0.45	1240	2.19 ±0.01	2.32 ±0.01
U4	0.51	1410	2.42 ±0.01	2.60 ±0.01
U5	0.56	1540	2.65 ±0.01	2.81 ±0.01
U6	0.62	1620	3.11 ±0.01	3.03 ±0.01
Test	l_{g+} (-)	$\tau_{b,1} \pm 95$ % CI (Nm^{-2})	$\tau_{b,2} \pm 95\%$ CI (Nm^{-2})	$\tau_{b,sp} \pm 95\%$ CI (Nm^{-2})
U1	17	0.296 ±0.003	0.296 ±0.003	0.28 ±0.01
U2	20	0.388 ±0.004	0.445 ±0.004	0.49 ±0.01
U3	22	0.480 ±0.004	0.538 ±0.005	0.52 ±0.01
U4	24	0.586 ±0.005	0.676 ±0.005	0.64 ±0.01
U5	27	0.702 ±0.005	0.790 ±0.006	0.87 ±0.01
U6	31	0.967 ±0.006	0.918 ±0.006	1.00 ±0.01

Table 2.1: Results of flat plate turbulent boundary layer experiments.

FOV measured 4×3 cm with 4 cm in the horizontal direction to match the shear plate length of 4.3 cm. The images were taken with a 1600 x 1200 14-bit camera (Vision Research, Phantom v9.1) fitted with a Nikon 105 mm f/2.8D AF Micro-Nikkor lens. Images were taken for 200 s, at 20 Hz yielding 4000 images and the time between images (Δt) ranged from 0.7 ms to 0.4 ms for the six tests with different mean flow velocities. Image pairs were analyzed using the dynamic sub-window PIV algorithm outlined in Cowen and Monismith (1997) after the background image from each image pair was removed. Sub-pixel peak location was obtained with the use of the spectral shifting technique given in Liao and Cowen (2005), which has been shown to reduce peak-locking and improve accuracy. The final pass of the image analysis was done with 32 x 32 pixels sub-windows with 50% overlap giving a velocity vector array of 97×71 ($x \times z$) for every image pair. The PIV algorithm produced approximately 90% valid vec-

tors; the number of valid vectors suffered slightly due to small differences in illumination intensity between images in each image pair because of the difficulty of achieving identical power output from both laser heads.

The PIV velocity data were decomposed into mean quantities and fluctuating quantities using the Reynolds decomposition given by

$$u = \langle u \rangle + u', \tag{2.10}$$

where u is the horizontal velocity but could be any flow quantity of interest, $\langle u \rangle$ represents its ensemble mean and u' is its instantaneous turbulent fluctuation. For this flow, the ensemble mean is the mean in time and the x-direction since the flow is steady with negligible variation in the x-direction within the FOV. The mean horizontal velocity profiles $\langle u(z) \rangle$ were thus computed from 194,000 data points at each vertical elevation. The Reynolds stress, given by $-\rho\langle u'w' \rangle$, was also calculated at each vertical location to give a Reynolds stress profile. From the mean velocity profile, the momentum thickness of the boundary layer was calculated by (Pope, 2000)

$$\theta = \int_0^\infty \frac{\langle u \rangle}{U_0}\left(1 - \frac{\langle u \rangle}{U_0}\right) dz, \tag{2.11}$$

using a numerical integration of the mean velocity profile upto the height of the FOV. This allowed a calculation of the momentum thickness Reynolds number, $Re_\theta = U_0\theta/\nu$, for each test. In zero pressure gradient turbulent boundary layers, there exists the well-known law of the wall for the mean velocity profile scaled by the friction velocity, $u_\tau = \sqrt{\tau_b/\rho}$. The law of the wall is usually written as

$$u_+ = \frac{1}{\kappa} \ln (z_+) + C, \tag{2.12}$$

where $u_+ = u/u_\tau$, $z_+ = u_\tau z/\nu$, $\kappa = 0.41$ and $C = 5.5$ (Pope, 2000).

The friction velocity, and hence the bed shear stress, was estimated in two different ways: (i) by least squares fit of the mean velocity profile to the law of the wall, denoted as $u_{\tau,1}$; (ii) by linear extrapolation of the Reynolds stress profile from $z/h > 0.075$ to $z = 0$, denoted as $u_{\tau,2}$. The values of $u_{\tau,1}$, $u_{\tau,2}$, and the corresponding bed shear stress values, $\tau_{b,1}$ and $\tau_{b,2}$, are given in Table 2.1. Figure 2.10 shows the mean horizontal velocity profiles normalized with $u_{\tau,1}$. The law of the wall is also plotted for comparison and shows good agreement with the data. The data also shows good agreement with the direct numerical simulation (DNS) dataset of Spalart (1988), for which $Re_\theta = 1410$. Figure 2.11 shows the profiles of the Reynolds stress normalized with $u_{\tau,2}$.

The deflection of the shear plate was recorded simultaneously with the PIV data at 50Hz. To obtain the deflection, the mean position of the shear plate after the flow was stopped and the fluid returned to rest was subtracted from the mean position of the shear plate during the flow. The measured deflection was converted to force using the stiffness and this force was divided by the area of the shear plate top surface to obtain a mean shear stress. For these experiments, the streamwise pressure gradients are negligible and there is no need to include a correction for the force due to pressure gradients. The measurements of bed shear stress using the shear plate sensor are denoted as $\tau_{b,sp}$ and given in Table 2.1.

Table 2.1 also gives estimates of the 95% confidence intervals on all mea-

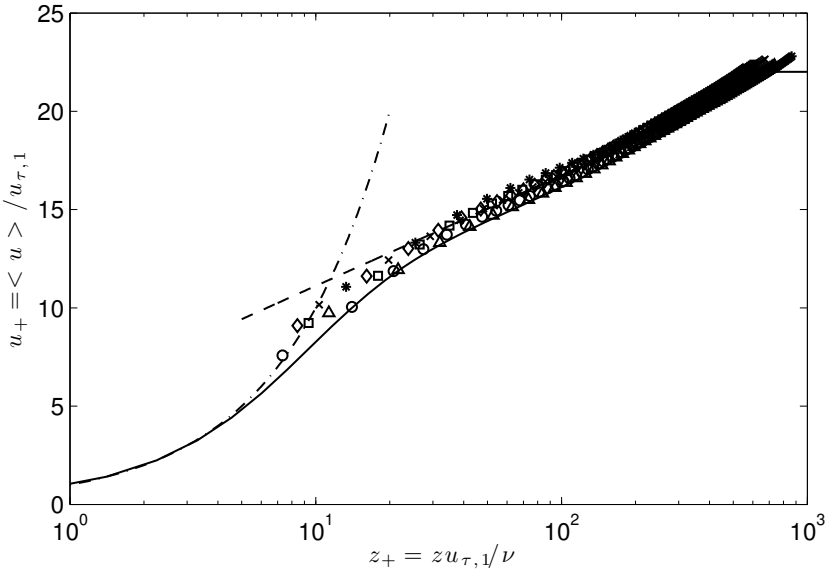

Figure 2.10: Mean horizontal velocity profiles for flat plate turbulent boundary layer experiments. ∘, U1 (U = 0.33 ms^{-1}, Re_θ = 910); ⋄, U2 (U = 0.40 ms^{-1}, Re_θ = 1120); □, U3 (U = 0.45 ms^{-1}, Re_θ = 1240); ×, U4 (U = 0.51 ms^{-1}, Re_θ = 1410); △, U5 (U = 0.56 ms^{-1}, Re_θ = 1540); ∗, U6 (U = 0.62 ms^{-1}, Re_θ = 1620); ——, Spalart (1988) DNS data; — —, law of the wall, Eq. (2.12).

surements. Following Moffat (1988), the uncertainty in the measurements was split into a bias error and a random error. For $\tau_{b,sp}$, the estimated 95% confidence intervals were calculated by a root-sum-square combination (*e.g.*, Taylor, 1997) of the 1% bias error found in the calibration and the random error, which was found by applying the bootstrap technique (Efron and Tibshirani, 1993) on the mean of the shear plate deflection. The combined error is reported to 1 significant figure. For the PIV results, the major bias error resulting from peak-locking effects was difficult to estimate quantitatively, but qualitatively, probability density functions of the particle displacement can show the peak-locking effect (Liao and Cowen, 2005). These were examined and showed there was little peak-locking, consistent with the use of the spectral shifting technique for finding sub-pixel peak location. However, the were several sources of random

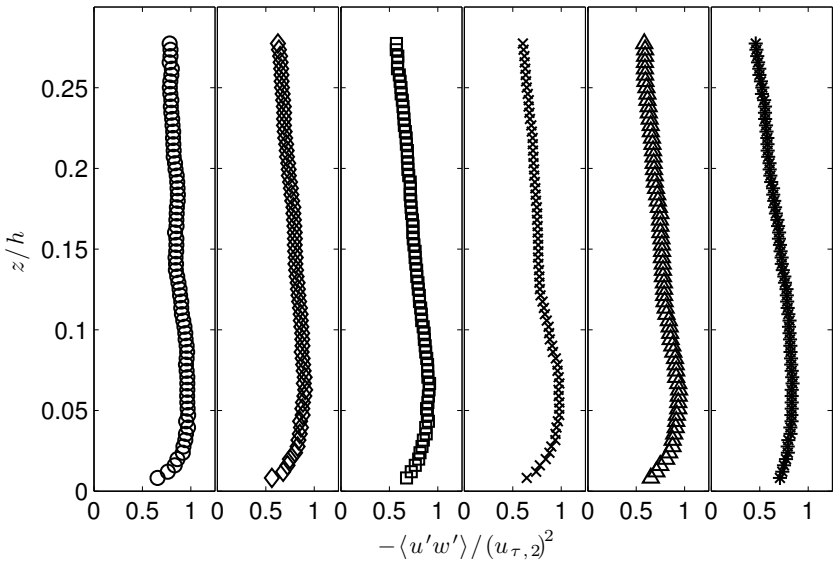

Figure 2.11: Reynolds stress profiles for flat plate turbulent boundary layer experiments. ∘, U1 (U = 0.33 ms^{-1}, Re_θ = 910); ⋄, U2 (U = 0.40 ms^{-1}, Re_θ = 1120); □, U3 (U = 0.45 ms^{-1}, Re_θ = 1240); ×, U4 (U = 0.51 ms^{-1}, Re_θ = 1410); △, U5 (U = 0.56 ms^{-1}, Re_θ = 1540); ∗, U6 (U = 0.62 ms^{-1}, Re_θ = 1620).

error in determining the particle displacement, *e.g.*, camera thermal noise, out of plane movement of particles, *etc.* (see Raffel, 2007, for a comprehensive list). There were also uncertainties in the coefficients of linear regression used to determine $u_{\tau,1}$ and $u_{\tau,2}$ from the mean velocity and Reynolds stress profiles. The overall random error in $u_{\tau,1}$ and $u_{\tau,2}$ was found by applying the bootstrap technique on the entire process of finding $u_{\tau,1}$ and $u_{\tau,2}$ from the raw velocity vectors. The uncertainty was then propagated to $\tau_{b,1}$ and $\tau_{b,2}$ using the standard root-sum-square combination. The results, with vertical error bars representing the estimated 95% confidence intervals, are plotted in Fig. 2.12.

There is good agreement between the direct measurement of bed shear stress using the shear plate sensor and the indirect measurement of bed shear stress using PIV velocity data. With the exception of tests U2 and U5, the shear plate

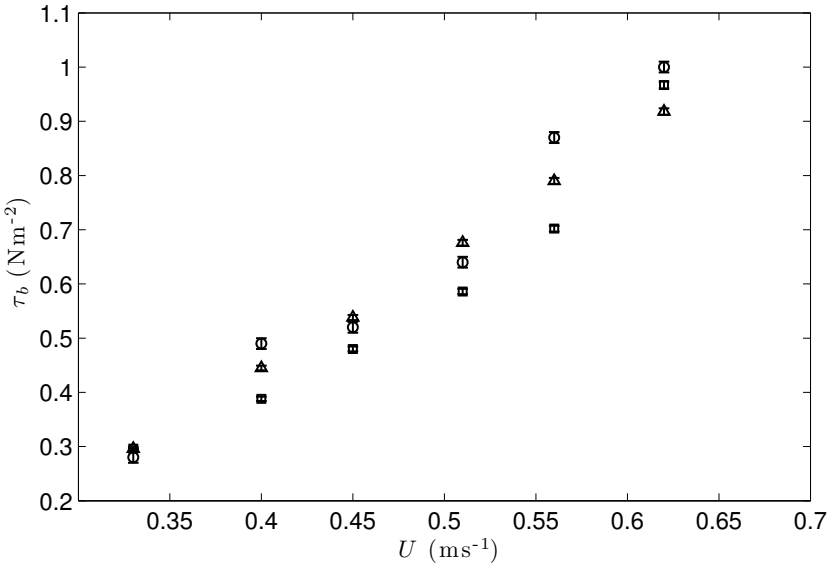

Figure 2.12: Bed shear stress data for flat plate turbulent boundary layer experiments. ∘, $\tau_{b,sp}$ (shear plate sensor data); □, $\tau_{b,1}$ (law of the wall fit to mean velocity profile); △, $\tau_{b,2}$ (extrapolation of Reynolds stress profile).

sensor data agree to within 10% of the values of shear stress obtained from the PIV velocity data. Additionally, there may be a bias error in the measurements of the shear plate sensor caused by the fact that for the low values of the bed shear stress, the shear plate sensor is more susceptible to small shifts in the zero position of the shear plate caused by vibration noise from the variable frequency pumps used to drive the flow in the channel. This error, which is difficult to quantify, could explain some of the discrepancy between the shear plate sensor measurements and the bed shear stress values obtained from PIV data. Finally, Table 2.1 also gives values of the gap size Reynolds number, l_{g+}, for all six tests calculated using $u_{\tau,1}$ and the values fall below $l_{g+} = 100$, Dhawan's (1953) empirical threshold for good measurement.

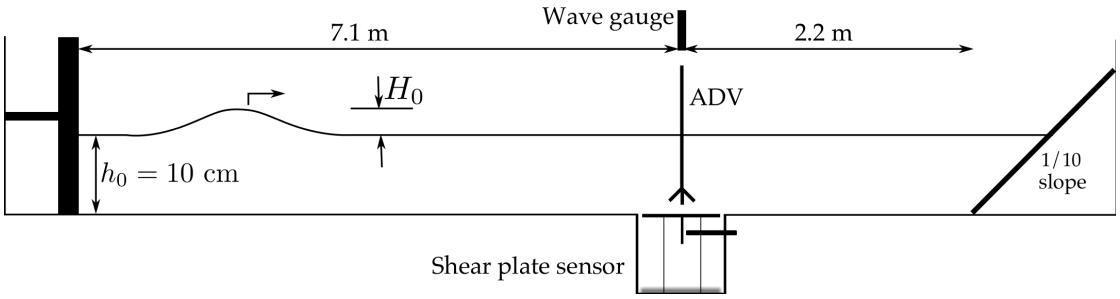

Figure 2.13: Schematic of the setup of solitary wave boundary layer experiments.

2.5.2 Laminar boundary layer under a solitary wave

In the absence of viscosity, a solitary wave is an elevation wave of permanent form propagating at constant phase velocity, but in the presence of viscosity, there exist thin boundary layers at the bottom boundary and at the free-surface that introduce damping to the solitary wave as it propagates in water of constant depth. The bottom boundary layer of the solitary wave was first analyzed by Keulegan (1948), but Liu and Orfila (2004) recently developed a more general theory for the bottom boundary layer of transient long waves. Liu *et al.* (2007) conducted an experimental study to measure the velocity profiles and bed shear stress in the bottom boundary layer under solitary waves using PIV and compared their results to the theory of Liu and Orfila (2004) applied specifically to solitary waves. Two wave cases from Liu *et al.* (2007) were repeated to compare the direct bed shear stress measurements from the shear plate sensor to: (i) the data from Liu *et al.* (2007); (ii) the theoretical solution to the linearized boundary layer equations presented in Liu *et al.* (2007).

Solitary waves were generated in a 15 m wave flume, equipped with a piston-type wavemaker capable of a stroke of 1.2 m and maximum wavemaker velocity of 0.25 ms^{-1}, in the DeFrees Hydraulics Laboratory at Cornell Univer-

sity. The setup of the experiment is shown in Figure 2.13. The stillwater depth was kept at $h_0 = 10.0$ cm and the shear plate sensor was installed in the flume with the top surface of the shear plate flush with the rest of the bed of the flume. The centre of the shear plate was at a distance of 7.1 m from the wavemaker in its retracted position. There was a plane beach of slope 1:10 installed at the other end of the flume but the toe of the beach was sufficiently far from the shear plate so that the waves did not encounter the sloping bottom until they had passed the shear plate sensor. An acoustic wave gauge (Banner Engineering, S18U; resolution ±0.5 mm) was positioned directly above the centre of the shear plate sensor to record the free-surface displacement. Two pressure gauges (Omega Engineering, PX26; resolution ±7.5 Pa) were used to record the pressure difference between the external pressure tappings and the chamber pressure tappings (see Figure 2.1).

Solitary waves of two different amplitudes were generated. The two wave cases are denoted as CW1, where the wave height was $H_0 = 0.83$ cm, and CW2, where the wave height was $H_0 = 2.00$ cm, respectively. Table 2.2 gives further properties of the solitary waves generated for these experiments. The wavelengths of the solitary waves in these experiments were much larger than the shear plate length and thus the bed shear stress and the streamwise pressure gradient can be assumed constant over the shear plate. The force due to the streamwise pressure gradient was expected to be significant. The estimated values of the ratio of pressure gradient force to shear force, $\alpha l_{pt}/u_\tau^2$, and the chamber flow Reynolds number, Re_{ch}, are also given in Table 2.2. The characteristic scale for the pressure gradient for solitary waves was derived using $\alpha = (1/\rho)\,(2\rho g H_0/L_0)$, which is the average steepness of the solitary wave assuming the pressure is hydrostatic. The assumption of hydrostatic pressure is only

valid for $\epsilon_0 \ll 1$, but still provides a useful way to characterize the pressure gradient. A characteristic bed shear stress value expressed as the friction velocity, u_τ, was also needed and this was obtained from the maximum value of the bed shear stress using the theoretical solution to in Liu *et al.* (2007). It can be seen from the data in Table 2.2 that the pressure gradient force is of the same order of magnitude as the shear force and $Re_{ch} > O(1)$ even for the small wave amplitudes used in these experiments. Thus, it was important to correct for the force due to pressure gradients, but the solution to the pressure distribution in the chamber and the calculation of the value of f_{pg} presented in section 2.4.1 may not be valid. Nonetheless, the constant value of $f_{pg} = 0.8$ was used to correct for the force due to pressure gradients, as presented below.

Additionally, it was found that the force on the shear plate was very small and the signal to noise ratio of the data was poor. To increase the signal to noise ratio of the shear plate sensor for the low values of shear stress in these experiments, each wave case was repeated 40 times and the results were ensemble averaged. Measurements of the free-surface displacement confirmed that the repetitions were aligned in phase and highly repeatable. An additional repetition of each wave was done where an ADV was also installed to measure the water velocity 2 cm above the bed, which was outside the boundary layer for both wave cases. It was operated at 40 Hz with a sampling volume of diameter 6 mm and height 7 mm.

Figure 2.14 shows the measurements of free-surface displacement for CW1 and CW2 and the comparison to the Boussinesq and Grimshaw theories. It can be seen that the data matches the theoretical solutions very well. The difference between the two theories is not significant so that the different lines are diffi-

Wave	H_0 (cm)	ϵ_0 (-)	L_0 (m)	T_0 (s)	Re_{ch} (-)	$\alpha l_{pt}/u_\tau^2$ (-)
CW1	0.83	0.083	2.57	2.49	60	0.6
CW2	2.00	0.200	1.62	1.50	240	1.0

Table 2.2: Properties of solitary waves in solitary wave boundary layer experiments.

cult distinguish. The horizontal and vertical velocities measured with the ADV are shown in Figure 2.15. Again, the data matches the theories very well. The pressure gradient at the bed is estimated by dividing the data of the external pressure difference by the distance separating the external pressure tappings. This estimated pressure gradient is plotted in Figure 2.16. The bed pressure from the Grimshaw and Boussinesq theories is numerically differentiated using a second-order finite difference scheme and also plotted. It can be seen that the assumption of constant pressure gradient over the shear plate area is a good one since the estimated pressure gradient matches the theories well. The discrepancies between the Grimshaw theory and Boussinesq theory for CW2 are more noticable (particularly in vertical velocity and bed pressure gradient) because the value of ϵ_0 is higher.

Figure 2.17 shows measurements of the bed shear stress using the shear plate sensor, derived from measurements of the total force on the shear plate using Eq. (2.2) with $f_{pg} = 0.8$ as discussed above. The shear plate sensor data show good agreement with the data of Liu *et al.* (2007) and with the solution to the linearized boundary layer equations of Liu *et al.* (2007) even though the magnitude of the pressure gradient force is comparable to the shear force, $\alpha l_{pt}/u_\tau^2 = O(1)$, and the chamber flow Reynolds number is not small. The most notable discrepancy is in CW2, where the shear plate sensor fails to capture the negative por-

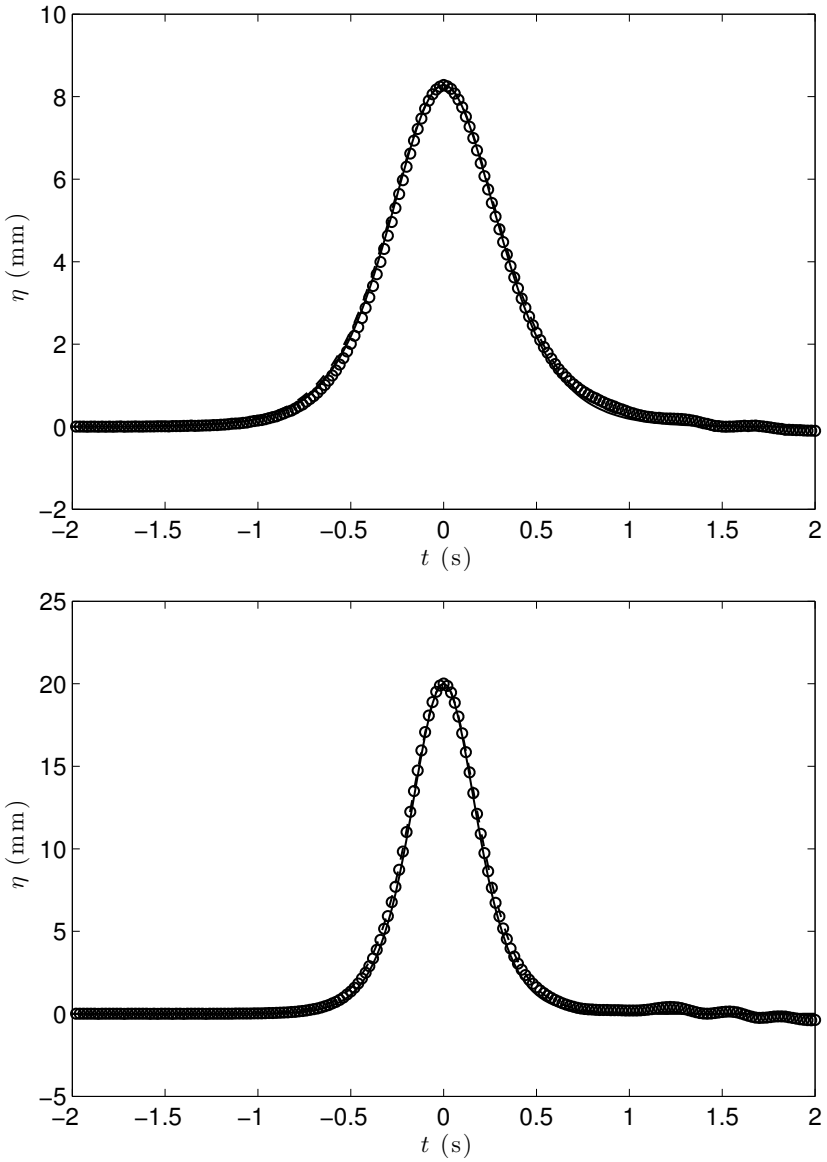

Figure 2.14: Free-surface displacement, η, for solitary wave boundary layer experiments. ∘, data; ——, Boussinesq solution; — —, Grimshaw solution. *Top*: CW1, H_0 = 0.83 cm, ϵ_0 = 0.083; *bottom*: CW2, H_0 = 2.00 cm, ϵ_0 = 0.200.

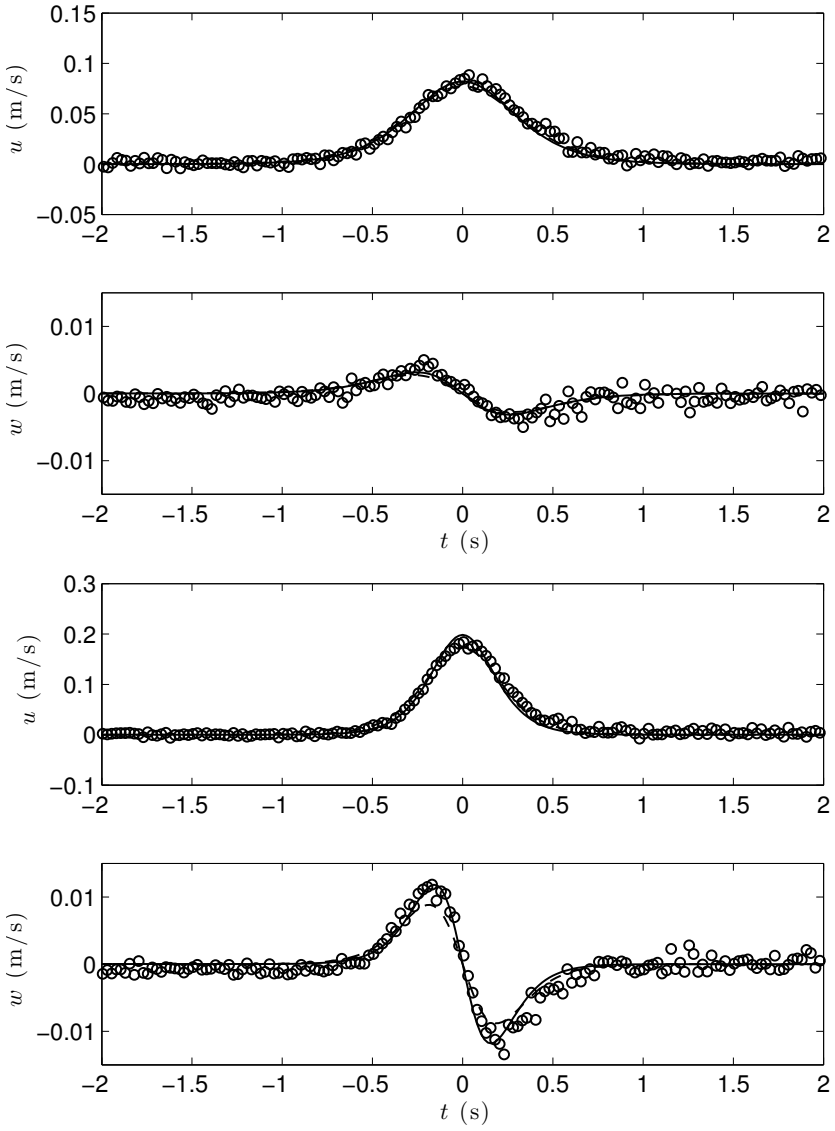

Figure 2.15: Horizontal and vertical velocities, u, w, for solitary wave boundary layer experiments. ∘, data; ——, Boussinesq solution; — —, Grimshaw solution. *Top*: CW1, H_0 = 0.83 cm, ϵ_0 = 0.083; *bottom*: CW2, H_0 = 2.00 cm, ϵ_0 = 0.200.

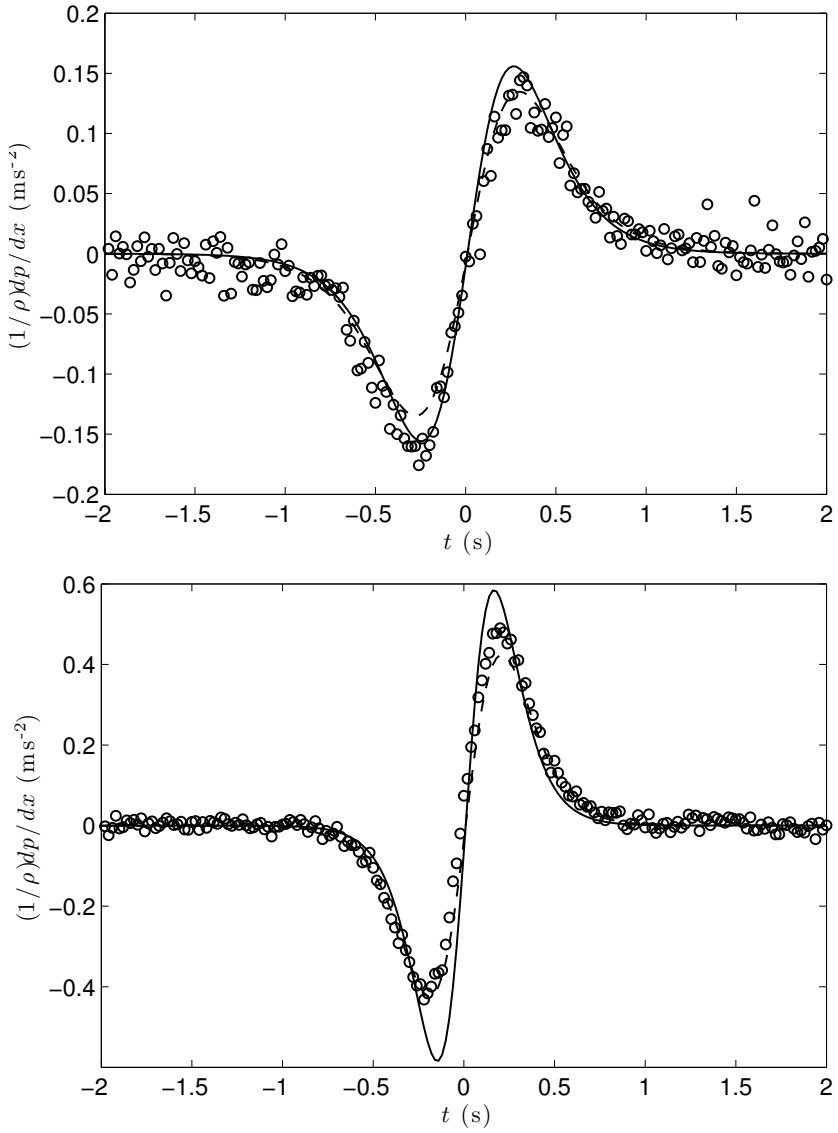

Figure 2.16: Pressure gradient at the bed in kinematic units, α, estimated using the pressure difference measurement from the external pressure tappings for solitary wave boundary layer experiments. ∘, data; ——, Boussinesq solution; — —, Grimshaw solution. *Top*: CW1, H_0 = 0.83 cm, ϵ_0 = 0.083; *bottom*: CW2, H_0 = 2.00 cm, ϵ_0 = 0.200.

tion of the bed shear stress signal that accompanies flow reversal in the bounary layer behind the wave crest as a result of the adverse pressure gradient. For CW2, $Re_{ch} > 100$ meaning that there may be a non-negligible flow through the chamber of the shear plate sensor (though it was too small to observe with coloured dye tests as described at the start of section 2.5). Measurements of pressure difference in the chamber, plotted in Figure 2.18, show that during the time when the bed shear stress is expected to be negative, the pressure on the downstream chamber wall was higher than the pressure on the upstream chamber wall. This pressure difference may be indicative of flow velocity in the chamber in the same direction as the external flow suggesting that the chamber flow was important during the short time under the wave crest and just behind it. Any such secondary flow through the chamber would affect the local velocity profile and cause an error in the measurement of bed shear stress, which would explain why the negative part of the shear stress was not captured. For the majority of the wave period, the pressure difference in the chamber was too small to measure leading to good measurement of the bed shear stress signal. Note, the resolution of the pressure difference measurements has been improved to ±1.2 Pa from ensemble averaging process.

For CW1, it can be seen that the bed shear stress signal is well-captured for the entire wave period and that measurements of the pressure difference in the chamber shows very small values. This is in accordance with the lower value of the chamber flow Reynolds number, $Re_{ch} < 100$, which predicted the chamber flow to be negligible.

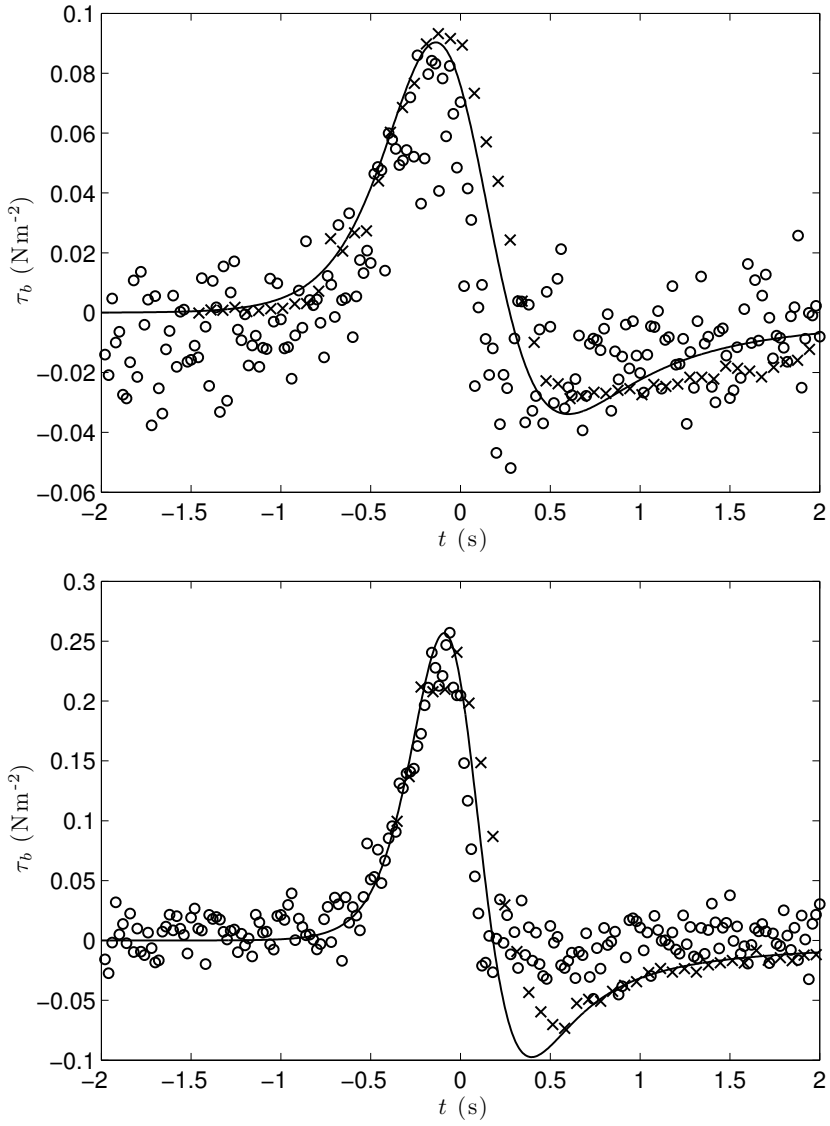

Figure 2.17: Bed shear stress, τ_b, for solitary wave boundary layer experiments. ∘, shear plate sensor data; ×, data from Liu *et al.* (2007); ——, bed shear stress from solution to linearized boundary layer equations in Liu *et al.* (2007). *Top*: CW1, H_0 = 0.83 cm, ϵ_0 = 0.083; *bottom*: CW2, H_0 = 2.00 cm, ϵ_0 = 0.200.

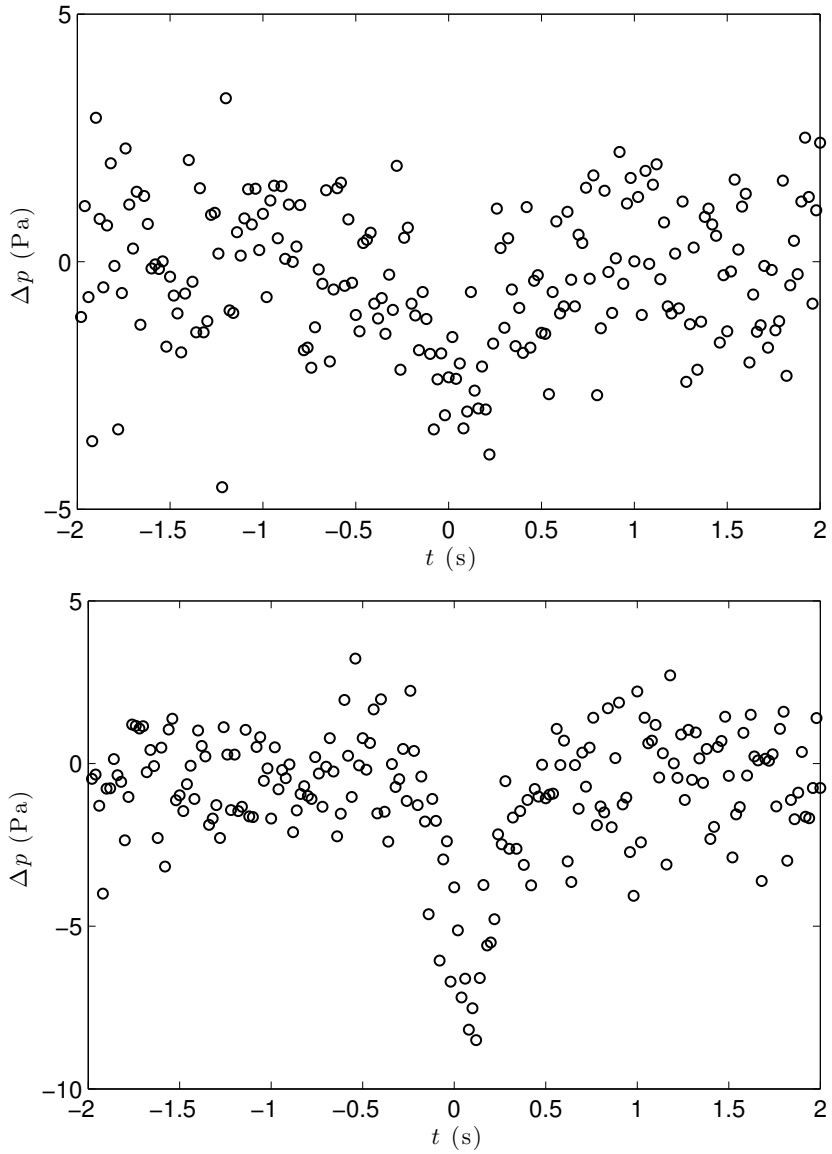

Figure 2.18: Pressure difference in the shear plate sensor chamber, Δp, for solitary wave boundary layer experiments. Negative values indicate higher pressure on downstream wall. ∘, data. *Top*: CW1, H_0 = 0.83 cm, ϵ_0 = 0.083; *bottom*: CW2, H_0 = 2.00 cm, ϵ_0 = 0.200.

2.6 Concluding remarks

The design of a shear plate sensor, capable of measuring the local mean bed shear stress in the range ±200 Pa with an accuracy of ±1% and within a bandwidth of 75 Hz, has been described. The design employs the use of an eddy-current proximity probe that is able to measure small deflections with high accuracy, in combination with a simple parallel-linkage mechanism, which provides stiffness against shear plate deflection, minimizes shear plate tilting, and does not require *in situ* calibration. The size of the shear plate is small compared to the typical horizontal lengthscale of waves and its bandwidth is fast compared to the typical timescale of waves. The shear plate sensor provides local measurements of the bed shear stress. In laminar flow, this is a true local bed shear stress (unless there are very strong spatial gradients in bed shear stress, *e.g.*, near a separation point) whereas in turbulent flow, scales of motion much smaller than the streamwise length of the shear plate are averaged out.

However, the true accuracy of the bed shear stress measurements depend primarily on the error introduced via the secondary forces on the shear plate, which are linked to how intrusive the sensor is to the flow being measured. If the presence of the sensor locally alters the flow in the boundary layer due to misalignments or flow circulations through the chamber, then the difficulty in correcting for the secondary forces due to those effects also increases. The Reynolds number, l_{g+} (Dhawan, 1953, defined in Eq. 2.9) provides a parameter to gauge whether the gap size is small enough to ensure the boundary layer and the bed shear stress is not locally altered by the presence of the gaps. The experiments in a flat plate turbulent boundary layer confirmed Dhawan's emprical rule that the sensor will be non-intrusive for $l_{g+} < 100$. For applications in the

nearshore region driven by wave action, however, even if the sensor is designed to have minimal intrusion on the flow, the accuracy suffers primarily due to the force due to the streamwise pressure gradients. Analysis of the pressure distribution in the gaps and chamber has allowed a new method to be developed to correct for this force: the effective fraction of the streamwise pressure gradient that acts on the shear plate, f_{pg}, can be calculated *a priori* and independently of the flow by the solution to Laplace's equation for the pressure field in the chamber. This is valid so long as the flow driven by the external pressure gradient is small enough. This flow will be small if either the pressure gradient is mild enough or the gap size is small enough to constrict the flow. The chamber flow Reynolds number, Re_{ch} (defined in Eq. 2.6), provides a parameter to characterize whether the flow in the chamber is small enough. The experiments in a laminar boundary layer driven by the pressure gradients due to the passage of solitary waves suggest that for $Re_{ch} < 100$, the bed shear stress can be accurately measured using an *a priori* calculation of f_{pg}.

$f_{pg} = 0.8$ for the shear plate sensor, which is valid for pressure gradients up to $\alpha = O\left(10^{-1}\right)$ ms^{-2} using the above empirical guideline. This can be still be a constraint under surface gravity waves, especially in small-scale flumes where the magnitude of the bed shear stress is very low and the force due to pressure gradient is large as shown by the test case of the boundary layer under the larger amplitude solitary wave (CW2 in Table 2.2). However, the design of the shear plate sensor makes it an especially suitable sensor to measure the bed shear stress in the nearshore region of a large-scale flume since the pressure gradients are relative mild and the magnitudes of bed shear stresses are high. Such a flow environment presents severe difficulties for indirect methods to measure the bed shear stress due to the shallow flow depth often containing

air bubbles, transient flow that that covers a large range of shear stress values (that can also change direction), and lack of optical access. Thus, the design of the shear plate sensor provides an inexpensive and robust way to measure the bed shear stress directly in the the nearshore region of a large-scale laboratory, making it a powerful tool to study the flow in that region.

CHAPTER 3

SWASH OF SOLITARY WAVES

3.1 Introduction

Laboratory investigations of the swash, the flow of water that covers and uncovers a beach with each incident wave, usually employ regular waves (*e.g.*, Cox *et al.*, 1996; Cowen *et al.*, 2003; Sumer *et al.*, 2013) to study multiple swash events, or a bore (*e.g.*, Yeh and Ghazali, 1988; Yeh *et al.*, 1989; Barnes *et al.*, 2009; O'Donoghue *et al.*, 2010; Kikkert *et al.*, 2012, 2013) to study an isolated swash event. However, solitary waves offer unique advantages in a laboratory study of the swash zone: (i) to the leading order, they do not transform while propagating in a rectangular channel with a flat bed; (ii) they break not unlike regular waves when climbing a beach where the water depth decreases, but produce a single, isolated swash event; (iii) varying the wave height of solitary waves (or alternatively varying the beach slope) allows control over what qualitative type of breaking occurs; (iv) there exist many studies of the run-up of solitary waves that can be used substantiate claims from new results. Thus, this chapter describes an experiments and results of the swash of solitary waves conducted to determine how a single swash event is influenced by the type of wave breaking that occurs.

An important component of the sediment transport in swash events is the variation of the bed shear stress, but because the swash zone is a challenging environment to make measurements in, fewer studies have focused on measuring the bed shear stress. The most common difficulties are that the flow depths are very shallow and the water often contains entrained air. Added

complexities include that the flow is unsteady and almost always turbulent. Laboratory and field studies typically measure the near-bed velocity to infer the bed shear stresss (*e.g.*, Cox *et al.*, 1996; Cowen *et al.*, 2003; Raubenheimer, 2004; O'Donoghue *et al.*, 2010; Sou and Yeh, 2011; Kikkert *et al.*, 2012) using assumptions about the boundary layer structure. Relationships between boundary layer velocities and bed shear stress established for steady flows are applied to the unsteady swash flow, which may give unreliable results (Kikkert *et al.*, 2009). There have been recent studies that used a shear plate sensor (Barnes *et al.*, 2009) and a hot-film sensor (Conley and Griffin, 2004; Sumer *et al.*, 2011) to measure the bed shear stress in the swash zone. They have found that the bed shear stress in the swash is asymmetric, i.e., that the uprush bed shear stress and corresponding friction coefficients are larger than the downrush bed shear stress and corresponding friction coefficients. It was also concluded that a constant friction coefficient was unable to predict the time evolution of the bed shear stress. However, although some properties of the boundary layer in the swash zone are known (Barnes *et al.*, 2009; Sou and Yeh, 2011; Kikkert *et al.*, 2012), active research efforts into the role of bed shear stress are ongoing. Thus, the shear plate sensor described in chapter 2, which is well-suited to directly measure the bed shear stress in the swash zone, is used in the experiments described in this chapter.

This chapter begins with a review of the well-established theories that use the non-linear shallow water equations to describe the climb and swash of a bore on a beach (Keller *et al.*, 1960; Ho and Meyer, 1962; Shen and Meyer, 1963, further described below) and the climb of non-breaking solitary waves on a beach (Synolakis, 1987, and others). A link is established between the approximate evolution of a bore approaching the shoreline (first proposed by Whitham,

1958) to the more recent solution to the swash flow described by the breaking of a dam on a sloping bed (Peregrine and Williams, 2001). The application of these theories to the swash of breaking solitary waves, and the influence of bed friction, *i.e.*, the deviations it creates from the idealized solution, forms later sections of the chapter. The final section of the chapter develops an integral model for the shoreline during a swash uprush that includes the effects of friction.

3.2 Non-linear shallow water equations

In the constant depth region, neglecting the effects of viscosity, a solitary wave maintains its form due to a balance between non-linear steepening and frequency dispersion but as the wave climbs a sloping beach, the water depth reduces and the non-linear effects dominate the effects of frequency dispersion. Thus, near the shoreline, the non-linear shallow water equations (NSWE), which are fully non-linear but neglect wave dispersion, are the appropriate governing equations. The NSWE are formulated in terms of depth-averaged quantities so that they are one-dimensional. They describe the balance of mass and momentum, which gives

$$\frac{\partial \eta}{\partial t} + \frac{\partial}{\partial x}\left[(h+\eta)\,\overline{u}\right] = 0, \tag{3.1a}$$

$$\frac{\partial \overline{u}}{\partial t} + \overline{u}\frac{\partial \overline{u}}{\partial x} + g\frac{\partial \eta}{\partial x} = 0, \tag{3.1b}$$

where g is the gravitational acceleration, $\overline{u}\,(x,t)$ is the depth-averaged velocity in the x-direction and $\eta\,(x,t)$ is the free-surface displacement measured from the stillwater level. (Onshore of the stillwater shoreline, $h = 0$ and the total water

depth is given by η). The beach slope has been assumed mild enough so that $\sin\theta \approx \tan\theta = s$ and $\cos\theta \approx 1$ so the errors from assuming distances, velocities, *etc.* in the beach-parallel direction are the same as those in the x-direction are negligible. See Peregrine (1972) for a full derivation of the NSWE.

The NSWE can be written in characteristic form by introducing the local long wave celerity, $c = \sqrt{g(h+\eta)}$ and restricting the beach slope to be a constant, $dh/dx = s$. Then, the NSWE can be expressed as

$$\left[\frac{\partial}{\partial t} + (\overline{u} + c)\frac{\partial}{\partial x}\right]\alpha = 0, \tag{3.2a}$$

$$\left[\frac{\partial}{\partial t} + (\overline{u} - c)\frac{\partial}{\partial x}\right]\beta = 0, \tag{3.2b}$$

where the characteristic variables (or Riemann invariants) are given by

$$\alpha = \overline{u} + 2c + gst, \tag{3.3a}$$

$$\beta = \overline{u} - 2c + gst, \tag{3.3b}$$

which are constants on on positive characteristics defined by $dx/dt = \overline{u} + c$ and negative characteristics defined by $dx/dt = \overline{u} - c$, respectively.

3.2.1 Bore collapse and the swash solution

The NSWE have been used to study the climb and swash of a bore on a plane beach, which relates to the climb of breaking waves. A bore is a moving discontinuity in the free-surface and depth-averaged velocity in the context of the

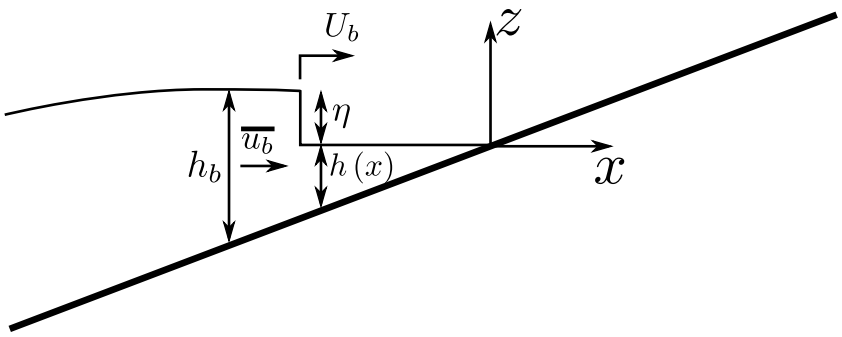

Figure 3.1: Definition sketch: a bore climbing a plane sloping beach.

NSWE. In reality, the jumps in water depth and depth-averaged velocity will take place over some finite distance (the 'bore front region') where the NSWE are invalid due to strong vertical accelerations, but across the bore front, the conservation of mass and momentum give (Stoker, 1957)

$$\frac{\overline{u_b}}{U_b} = 1 - \frac{h}{h_b}, \tag{3.4a}$$

$$2U_b^2 = gh_b\left(1 + \frac{h_b}{h}\right), \tag{3.4b}$$

respectively, where $h(x)$ is the undisturbed water depth, $h_b = h + \eta$ is the flow depth behind the bore front, $\overline{u_b}$ is the depth-averaged flow velocity behind the bore front and U_b is the velocity of the bore front, as shown in Figure 3.1. Equations (3.4), known as the bore relations, imply that while mass and momentum are conserved across the bore front, energy is dissipated, which is physically interpreted as the turbulent dissipation from breaking.

If the beach slope, s, in the characteristic variables, Eq. (3.3), is replaced by dh/dx, it can be shown that the differential relation $d\overline{u} + 2dc - gdh/(\overline{u} + c) = 0$ is valid on positive characteristics, $dx/dt = \overline{u} + c$. Whitham (1958) applied the bore relations, Eq. (3.4), to this differential relation valid on positive character-

istics to obtain an approximate formula for the evolution of the bore (known as Whitham's formula),

$$\frac{1}{h}\frac{dh}{dM} = \frac{-4\,(M+1)\left(M-\frac{1}{2}\right)^2\left(M^3+M^2-M-\frac{1}{2}\right)}{(M-1)\left(M^2-\frac{1}{2}\right)\left(M^4+3M^3+M^2-\frac{3}{2}M-1\right)}, \tag{3.5}$$

where $M = U_b/\sqrt{gh_b}$ is introduced as a bore strength parameter [small value of $(M-1)$ means a bore of low strength] and is related to the properties of the bore via

$$\frac{\eta}{h} = 2\left(M^2-1\right), \tag{3.6a}$$

$$\frac{\overline{u_b}}{\sqrt{gh}} = \frac{2M\left(M^2-1\right)}{\sqrt{2M^2-1}}, \tag{3.6b}$$

$$\frac{U_b}{\sqrt{gh}} = M\sqrt{2M^2-1}. \tag{3.6c}$$

Thus, Whitham's formula is equivalent to specifying that the flow depth and depth-averaged velocity behind the bore front follow the characteristic rule, *i.e.*,

$$\overline{u_b} + 2c_b + gst = \text{const.}, \tag{3.7}$$

where $c_b = \sqrt{gh_b}$. Keller *et al.* (1960) provided a solution to Whitham's formula,

$$h = A\frac{\left(M^2-\frac{1}{2}\right)\exp\left[0.2808\arctan\left(M+0.6769\right)/0.3179\right]}{(M-1)^{\frac{4}{5}}\left(M-0.7471\right)^{1.180}\left(M^2+1.354M+0.5593\right)^{1.173}\left(M+2.393\right)^{1.673}}, \tag{3.8}$$

where the constant of integration, A, is determined from an initial condition for the bore strength, M, and the corresponding stillwater depth at the location of

the bore front, h. The solution, Eq. (3.8), predicts the bore collapse phenomenon: as the bore front reaches the stillwater shoreline where $h = 0$, the height of the bore, η, vanishes and the depth-averaged velocity behind the bore, $\overline{u_b}$, and the bore front velocity, U_b, approach the same, finite, limit, U_s. This rapid conversion of potential energy to kinetic energy happens very rapidly near the shoreline. The constant of integration, A, and the velocity limit, U_s, both provide a measure of the energy at the time of bore collapse in units of length and velocity, respectively, and they are related via $U_s = 1.763\sqrt{gA}$ (Keller *et al.*, 1960).

Ho and Meyer (1962) showed that not only does Whitham's formula provide an accurate approximation of bore evolution as the bore approaches the stillwater shoreline, but that the development of the bore in the last stages before it reaches the stillwater shoreline depends only very weakly on the details of the wave forming the bore. As the bore approaches the shoreline, the initial conditions are forgotten and the solution is governed by the singularity in the NSWE as $h \to 0$ (Meyer and Taylor, 1972). Keller *et al.* (1960) also reached the same conclusion from their numerical computations. Barker and Whitham (1980) also showed that Whitham's formula is accurate when the bore strength is high by showing that as the bore approaches the shoreline, the velocity of the bore front, U_b, matches the velocity of the limiting characterisitc that reaches the shoreline at the same time as the bore front. Thus, Whitham's formula provides an accurate prediction of the velocity limit, U_s, provided the initial condition for the bore strength is sufficiently high, *i.e.*, the bore front is sufficiently close to the stillwater shoreline.

Shen and Meyer (1963) extended the analysis of Ho and Meyer (1962) to the swash generated by bore collapse and found that the shoreline, which impul-

sively starts moving at the velocity U_s, follows a parabolic path, just as a solid particle with an initial velocity that is acted on only by the force of gravity. This shoreline motion is described by

$$x_s = U_s t - \frac{1}{2} g s t^2, \tag{3.9a}$$

$$u_s = U_s - g s t, \tag{3.9b}$$

where x_s is the shoreline position, u_s is the shoreline velocity, and $t = 0$ denotes the time of bore collapse. Shen and Meyer (1963) also found that the water surface local to the shoreline to be tangential to the bed and given by $\eta(x,t) \rightarrow [x_s(t) - x]^2/(3t)^2$ as $(x_s - x) \rightarrow 0$. Thus, the pressure gradient for the fluid at the shoreline tip is negligible and the shoreline motion is governed solely by the force of gravity. Peregrine and Williams (2001) extended Shen and Meyer's asymptotic solution by applying their local water depth solution globally to the entire swash. From the global solution to the water depth, Peregrine and Williams also obtained the depth-averaged velocity throughout the swash. This solution is referred to as the swash solution and is given by

$$\eta(x,t) = \frac{1}{9g}\left(U_s - \frac{1}{2} g s t - \frac{x}{t}\right)^2, \tag{3.10a}$$

$$\overline{u}(x,t) = \frac{1}{3}\left(U_s - 2 g s t + 2\frac{x}{t}\right), \tag{3.10b}$$

where η is used to denote the total water depth in the swash ($x > 0$) since the stillwater depth, h, is zero there. The swash solution is an explicit solution to the NSWE and the only scaling parameter in the swash solution is U_s, the velocity with which the shoreline starts to move. The swash solution is analogous to the

classic dam-break solution on a horizontal bed, which is given by (*e.g.*, Stoker, 1957)

$$\eta_d(x_d, t_d) = \frac{1}{9g}\left(2\sqrt{gh_d} - \frac{x_d}{t_d}\right)^2, \tag{3.11a}$$

$$\overline{u_d}(x_d, t_d) = \frac{2}{3}\left(\sqrt{gh_d} + \frac{x_d}{t_d}\right), \tag{3.11b}$$

where η_d is the water depth, $\overline{u_d}$ is the depth-averaged velocity, and the dam is located at $x_d = 0$ with an initial water depth of h_d behind it. The bed in front of the dam is initially dry and the dam breaks at $t_d = 0$. Peregrine and Williams (2001) pointed out that a transformation of the variables $(x, t, \overline{u}, c, \eta, U_s) = \left(x_d - gst_d^2/2, t_d, \overline{u_d} - gst_d, c_d, \eta_d, 2\sqrt{gh_d}\right)$ recovers the swash solution. Therefore, just as the dam-break solution follows from any set of initial conditions for which $\overline{u_d} + 2c_d = 2\sqrt{gh_d}$ in $x_d < 0$, the swash solution follows from any set of initial conditions for which

$$u + 2c + gst = U_s \text{ in } x < 0. \tag{3.12}$$

In other words, what is required is that the value of the characteristic variable, α, is the same constant on all incoming positive characteristics, so that $\alpha = U_s$ for $(x, t) > (0, 0)$. Whitham's formula for bore evolution, Eq. (3.5), provides exactly this initial condition via bore collapse, *cf.* Eq. (3.7). Since the accuracy of Whitham's forumla increases as the bore approaches the shoreline and collapses, the swash solution is expected to follow bore collapse. This link between bore collapse as described by Whitham's formula and the swash solution has not been explicitly stated before.

3.2.2 Solutions for non-breaking solitary waves

The NSWE were also used by Synolakis (1987), who applied the formulation of Carrier and Greenspan (1958) and Keller and Keller (1964), to study non-breaking solitary waves moving from a constant depth region onto a plane beach. Synolakis found a solution to the NSWE for an incident solitary wave at the toe of the beach under the assumption that the non-linearity, ϵ_0, is negligible before the wave starts to climb the slope. In his theory, the run-up, R (defined in figure 3.2), of non-breaking solitary waves when the slope is mild enough so that the change in stillwater depth over one wavelength is small ($s\epsilon_0^{-1/2} \ll 3.47$) is given by

$$\frac{R}{h_0} = 2.831 s^{-\frac{1}{2}} \epsilon_0^{\frac{5}{4}}. \tag{3.13}$$

Synolakis also provided a breaking criterion based on when the free-surface first becomes vertical, *i.e.*, when the Jacobian of the non-linear hodographic transformation used to solve Eq. (3.1) becomes zero. The breaking criterion was found to be

$$\epsilon_0 > 0.8183 s^{\frac{10}{9}}, \tag{3.14}$$

but it was noted that this method would predict breaking (defined as when the free-surface first becomes vertical) earlier than expected in reality due to neglect of dispersion in the NSWE. Recently, Madsen and Schäffer (2010) provided a summary to the analytical solutions to the problem of waves traveling over a constant depth region and then climbing a plane beach using the NSWE on the

plane beach and assuming linearized governing equations in the constant depth region. An incident solitary wave with small non-linearity was presented as a special case with the same run-up result, but with an additional criterion to predict breaking during downrush,

$$\epsilon_0 > 0.5139 s^{\frac{10}{9}}, \tag{3.15}$$

and a result for the run-down, R_d,

$$\frac{R_d}{h_0} = -1.125 s^{-\frac{1}{2}} \epsilon_0^{\frac{5}{4}}. \tag{3.16}$$

Downrush breaking has also been referred to as the landward-facing bore in the downrush by Hibberd and Peregrine (1979) and is referred to herein as the hydraulic jump in the downrush. The run-down is defined as the largest vertical distance that the shoreline recedes below stillwater shoreline, as shown in Figure 3.2. The run-down result is for non-breaking waves and Madsen and Schäffer's theory predicts downrush breaking to occur before the shoreline reaches its predicted run-down. The downrush breaking criterion, Eq. (3.15), is also more stringent than the uprush breaking criterion, Eq. (3.14), so that waves of small amplitude that may not break during uprush may break during downrush.

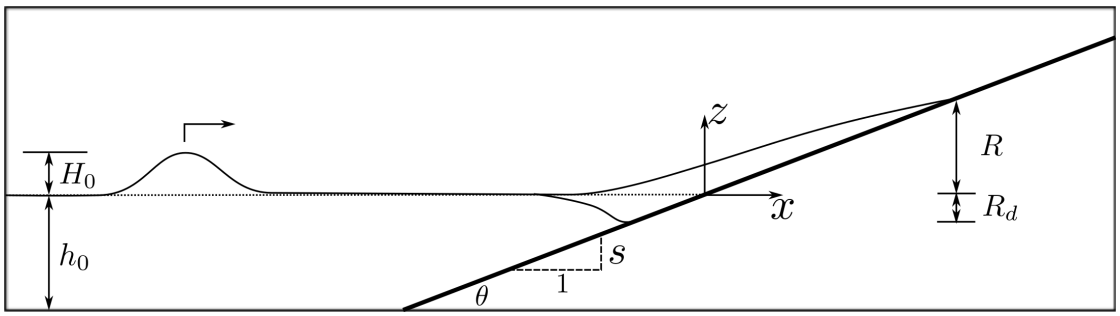

Figure 3.2: Definition sketch: an incident solitary wave in region of constant depth and a plane sloping beach. R is the run-up, the maximum vertical excursion of the water up the beach and R_d is the run-down, the maximum vertical distance the shoreline recedes below the stillwater shoreline. The beach slope, $s = \tan\theta$.

3.3 Experimental setup

Experiments were conducted in the Large Wave Flume (LWF) at the Hinsdale Wave Research Laboratory at Oregon State University to study the swash of solitary waves at a much larger scale than typical laboratory studies. The basic setup of the problem under consideration is given in Figure 3.2: a solitary wave is generated in the horizontal bed region where the water depth is constant and is incident upon a plane beach of constant slope where it creates a swash event.

3.3.1 The large wave flume

The LWF is a flume of length 104 m, width 3.7 m and depth 4.6 m deep equipped with a piston-type wavemaker installed at one end of the flume and a plane beach of slope 1:12 at the other end. A schematic of the LWF setup is shown in Figure 3.3. The flume side walls and floor are made of concrete and the plane beach is made of discrete concrete panels of length 3.7 m, width 3.7 m and thick-

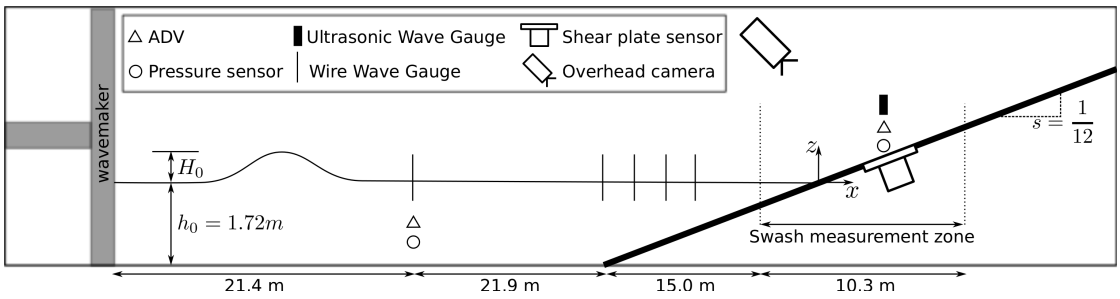

Figure 3.3: Schematic of the experimental setup in the large wave flume.

ness 0.3 m. These panels are held in place with metal brackets that are bolted to the side walls. A custom-built test platform replaced one of the concrete panels and housed the instruments to make measurements of the bed shear stress and near-bed flow quantities. The test platform was made of marine plywood painted with a water-resistant paint and reinforced with Aluminium beams underneath. Photographs of the test platform are shown in Figure 3.4.

A large water depth in the constant depth region, h_0 = 1.72 m, was used to ensure high Reynolds number swash events relevant to field conditions since it is known that, in small-scale experiments, swash tongues become laminar and viscosity and surface tension become important (Mahony and Pritchard, 1980; Liu *et al.*, 1991; Pedersen *et al.*, 2013). Measurements of free-surface displacement, water particle velocity and dynamic pressure were made in the constant depth region, at a distance of 21.4 m from the wavemaker, when it was in its fully retracted position. There were additional measurements of the free-surface displacement at the toe of the beach and further onshore. The free-surface displacement measurements were made using custom-built resistance-type wave gauges, which were calibrated by the standard method of lowering systematically into water and recording the output voltage. The gauges were calibrated at the start and end of every day and the calibration coefficients used for each

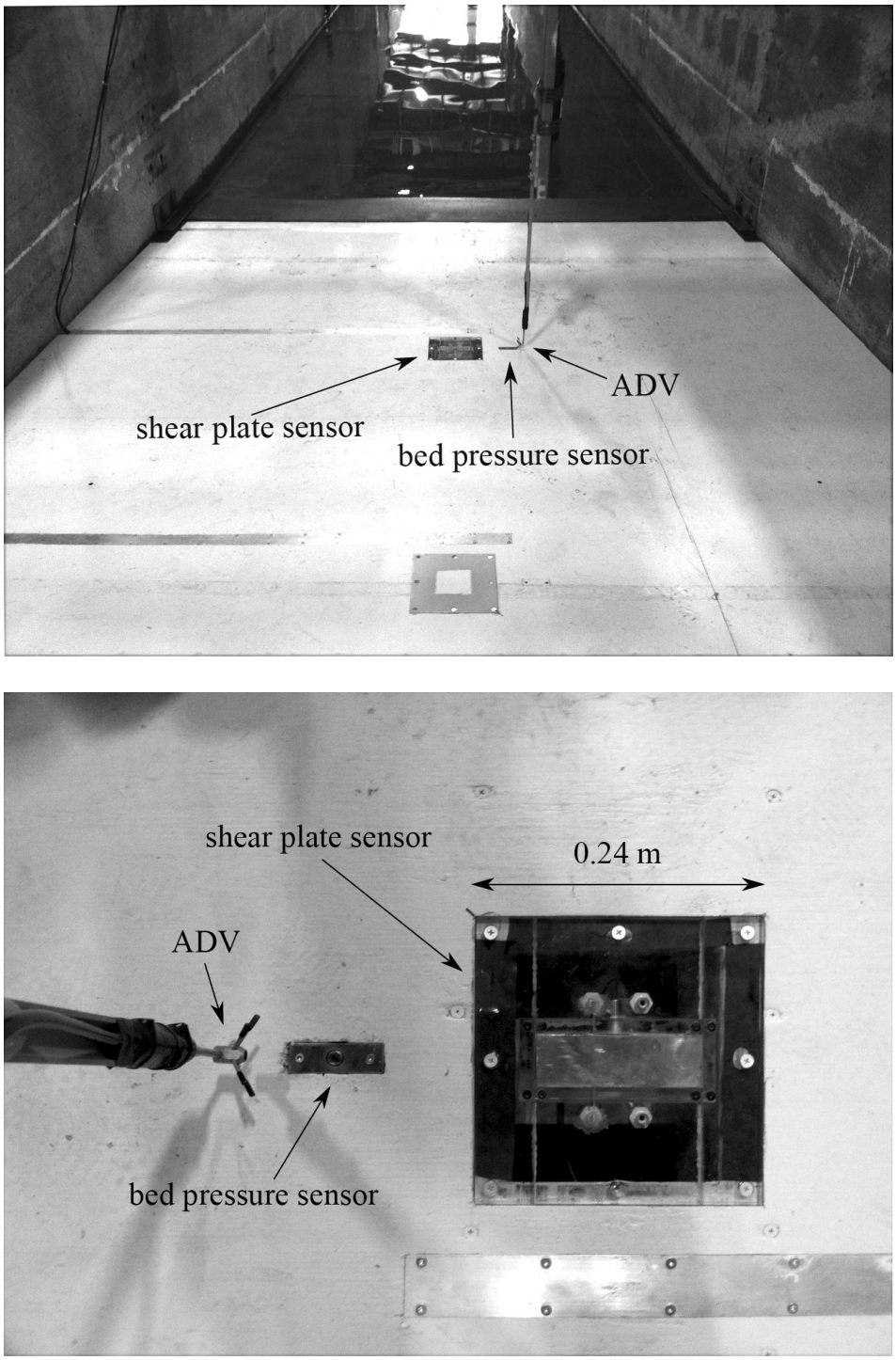

Figure 3.4: Photographs of the test platform installed in the large wave flume. *Top*: looking down the sloping beach towards the wave-maker; *bottom* top view of setup of instruments.

experimental run were values linearly interpolated in time. This procedure was followed because it was found that the calibration coefficients were prone to drift – thought to be a combination of the changing chemical composition of the water, which changes the resistivity, and changing surface conditions on the wires, which changes their conductivity (*e.g.*, Dibble and Sollitt, 1989). The water particle velocity was measured using an acoustic doppler velocimeter (ADV, Nortek Vectrino with plus firmware) mounted at a height of $z = -1.1$ m and the dynamic pressure was measured using a pressure transducer (Druck PDCR 830; accuracy 30 Pa) mounted at a height of $z = -1.41$ m.

3.3.2 Measurements in the swash

Measurements of local bed shear stress, free-surface level, bed pressure and near-bed velocity were made in the swash measurement zone (see Figures 3.3-3.4) at nine different locations. The local bed shear stress was measured using the shear plate sensor. The free-surface elevation was measured using an ultrasonic wave gauge (Senix TS-30S1 series; accuracy 1 mm), the bed pressure was measured using a pressure transducer (Druck PDCR 830; accuracy 30 Pa) that was installed with its measurement face flush with the bed, and the near-bed velocity was measured using a side-looking ADV (also Nortek Vectrino with plus firmware) mounted with its measurement volume at a height of 2 cm above the bed. All measurements in the swash measurement zone are collocated in the cross-shore direction. The ultrasonic wave gauge was installed directly over the center of the shear plate sensor and the ADV was installed such that its measurement volume was directly above the pressure transducer. The test platform had three separate sites for installation of the shear plate sensor and bed pressure

transducer and the test platform was in turn installed in three separate positions on the plane beach replacing a different concrete panel each time. Relative to the stillwater shoreline, the co-ordinates of the measurement locations are shown to scale in Figure 3.5. Each wave case was regenerated for each measurement location. The data taken at different locations were synchronized using the start of the wavemaker motion. The incident waves aligned in phase in this way were found to be very repeatable; the largest time-averaged standard deviation of separate runs of the same wave was less than 1.5 mm. At locations onshore of the stillwater shoreline ($x > 0$ in Fgure 3.5), the ADV was only submerged in water of sufficient depth for a short duration of time in which the signal to noise ratio (SNR) was above a threshold value of 15 dB. Thus, the near-bed velocity measurements are only available during the uprush after the swash tip, carrying entrained air, had passed and during the downrush before the water depth becomes less than approximately 5 cm. All instruments were recorded at a rate of 50 Hz using a data acquisition system (National Instruments PXI-6259) and all instrument positions were recorded using a surveying system (Nikon NPL-352; resolution 5 mm).

The pressure gradient in the flow direction was estimated via measurements of the pressure difference between the pressure tappings upstream and downstream of the shear plate using a differential pressure transducer (Omega engineering PX409 series; accuracy 2.5 Pa). It was found that the magnitude of the estimated pressure gradient force on the shear plate reached as high as 25% of the total force when the shear plate sensor was located offshore of the stillwater shoreline (locations L1 and L2). Under these circumstances, it is important to use both terms in Eq. (2.2) to obtain the bed shear stress. At locations onshore of the stillwater shoreline (locations L3–9), the magnitude of the largest esti-

mated pressure gradient force only reached 10% of the total force. For breaking waves, this ratio was even smaller at 5%. However, the pressure gradient measurements were found to be unreliable for breaking waves at locations onshore of the stillwater shoreline, likely because the pressure difference was very small and the vibration noise created by the breaking waves caused a disturbance to the differential pressure sensor that led to drifts in the measurements and shifts in the zero level. Fortunately, as mentioned above, the highest ratio of the pressure gradient force to the total force on the shear plate sensor in these cases was 5%. Thus, a conservative estimate of the accuracy of the bed shear stress measurements can be considered to be ±5%, but its actual accuracy for the majority of the swash cycle is closer to the accuracy of the sensor, ±1%. The bed shear stress measurements suffered from an additional issue related to the large-scale nature of the facility. The discrete composition of the plane beach meant that small gaps, protrusions and recessions at the edges of the test platform and between the test platform and sidewalls were unavoidable. The gaps and recessions were filled with plywood planks and expanding foam and re-levelled. Thus, at locations close to the edge of the test platform, the shear plate sensor did not capture the shear stress near the swash tip accurately. Locations L1, L3, L4 and L6 suffered from this issue and hence flow quantities near the swash tip at these locations show disrupted signals.

Additionally, the shoreline motion was also tracked using overhead cameras. Two cameras (Panasonic AW-HE60) were mounted above the flume and recorded the experiments at 59.94 Hz. With the instruments located at location L1 (Figure 3.5), the stillwater shoreline and the entire swash was visible to the cameras. A small LED was installed that was visible in the camera frame, which turned on to indicate the start of the data acquisition system. In this way,

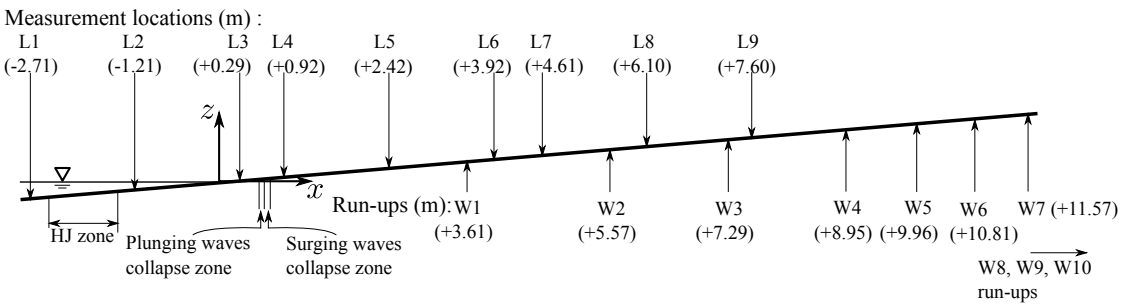

Figure 3.5: A diagram that shows , to scale, of the swash measurement zone. L1, L2, *etc.* are the measurement locations. The diagram also shows the zone of wave collapse during uprush, the run-up, R, of all ten wave cases (W1, W2, *etc.*), and the zone where the hydraulic jump occurs, i.e., the run-down limit, R_d, for all ten wave cases. Numbers in brackets are values for the x-coordinate.

the data from the camera were synchronized to the rest of the data to within one data sample (±0.02 s). Regularly spaced markings on the concrete panels were used to remove camera distortion and perspective by mapping these points from the camera data to their true location, which was known from survey measurements. The camera data was then interpolated onto a horizontal plane with a new uniform resolution of 1 pixel/cm. The original resolution of the camera was higher than 1 pixel/cm in the swash measurement zone so the accuracy of the shoreline tracking near the shoreline was not limited by camera resolution. After this image processing, a tracking algorithm was used, which looked for strong spatial gradients in the middle third (in the spanwise sense) of the flume, to track the position of the shoreline at each time step. This method of tracking the position of the shoreline was only successful for the uprush flow. The receding shoreline was somewhat ambiguous since the water depth gradually decreased to zero on the wetted beach and there was no sharp optical signature.

Wave	H_0 (m)	ϵ_0 (-)	L_0 (m)	T_0 (s)	U_0 (ms^{-1})	a_0 (m)	Re_0 $\left(\times 10^5\right)$
W1	0.085	0.050	56.6	13.4	0.20	0.42	0.6
W2	0.128	0.074	46.1	10.8	0.30	0.51	1.1
W3	0.173	0.100	39.6	9.2	0.40	0.58	1.7
W4	0.226	0.131	34.7	7.9	0.51	0.67	2.4
W5	0.261	0.151	32.3	7.3	0.58	0.71	2.9
W6	0.295	0.171	30.4	6.8	0.65	0.75	3.5
W7	0.345	0.199	28.1	6.2	0.74	0.81	4.3
W8	0.410	0.237	25.8	5.6	0.85	0.86	5.2
W9	0.443	0.256	24.8	5.4	0.92	0.88	5.8
W10	0.493	0.286	23.5	5.0	1.00	0.91	6.5

Table 3.1: Properties of incident solitary waves.

3.4 Incident waves

With the water depth kept constant at $h_0 = 1.72$ m throughout the experiments, solitary waves of ten different wave heights were generated at the wavemaker. The wave heights were measured at the wave gauge in the constant depth region and used to calculate the effective wavelength and effective period, Eq. (1.6). The Reynolds number, Eq. (1.12), was calculated using the ADV measurements in the constant depth region – the velocity scale was the maximum u-velocity measured by the ADV and the horizontal water particle half-excursion length was calculated from the u-velocity data of the ADV as

$$a_0 = \frac{1}{2}\int_{-T_0/2}^{T_0/2} u\mathrm{d}t \tag{3.17}$$

by numerical integration of the data. All properties of the incident solitary waves are given in Table 3.1. The incident wave non-linearity, ϵ_0, and the solitary wave Reynolds number, Re_0, span an order of magnitude. The horizontal

distance from the wavemaker to the still water shoreline was 58.3 m, which was roughly equal to the wavelength of the longest wave generated and roughly twice the wavelength of the shortest wave generated. Since the waves only travelled small multiples of their wavelength in the flume, wave damping was negligible.

Figures 3.6-3.8 show measurements of the free-surface displacement and velocity in the constant depth region for waves W3, W5, W10. The Boussinesq and Grimshaw solutions for solitary waves are also plotted for comparison. The data matches these theoretical solutions very well. The Boussinesq solution provides a slightly better match for the free-surface displacement, perhaps due to the fact that the wave-maker trajectory is based on the Boussinesq solution. The Grimshaw solution provides a better match for the water particle velocities, especially the vertical velocity.

3.4.1 Wave breaking and the slope parameter

Solitary waves travelling from a region of constant depth onto a sloping beach can interact with the beach in different ways. The first distinction is whether the wave will break or not, and if the wave does break, different regimes of breaking can be defined analogous to regular waves, *e.g.*, surging, collapsing, plunging, or spilling as described by Galvin (1972) and classified by Battjes (1974) using a surf similarity parameter that compared the slope of the beach to the local steepness of the wave. For solitary waves, Grilli *et al.* (1994, 1997) studied the shoaling and breaking numerically by solving the Laplace equation for the velocity potential without further assumptions using a boundary element method.

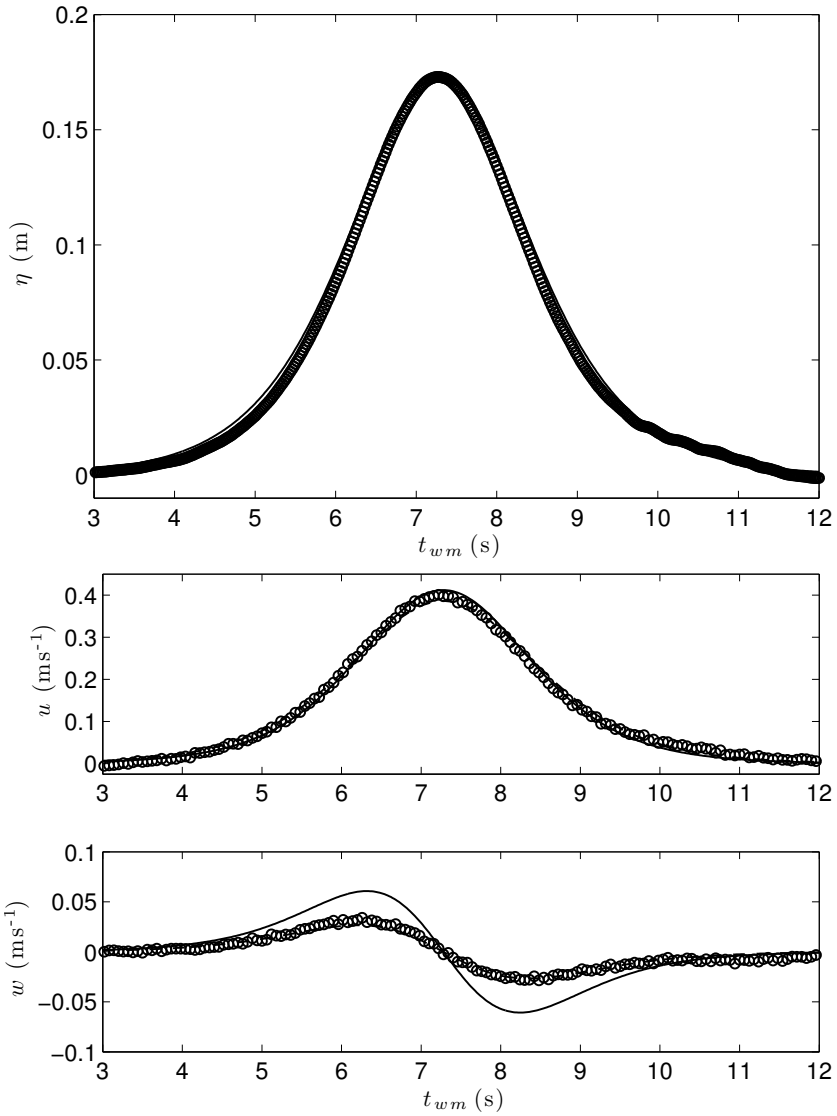

Figure 3.6: Free-surface displacement and velocity in the constant depth region for W3 (NB, H_0 = 0.173 m, ϵ_0 = 0.100): ∘, data; ——, Boussinesq solution; — —, Grimshaw solution. *Top*: free-surface displacement; *bottom*: velocity.

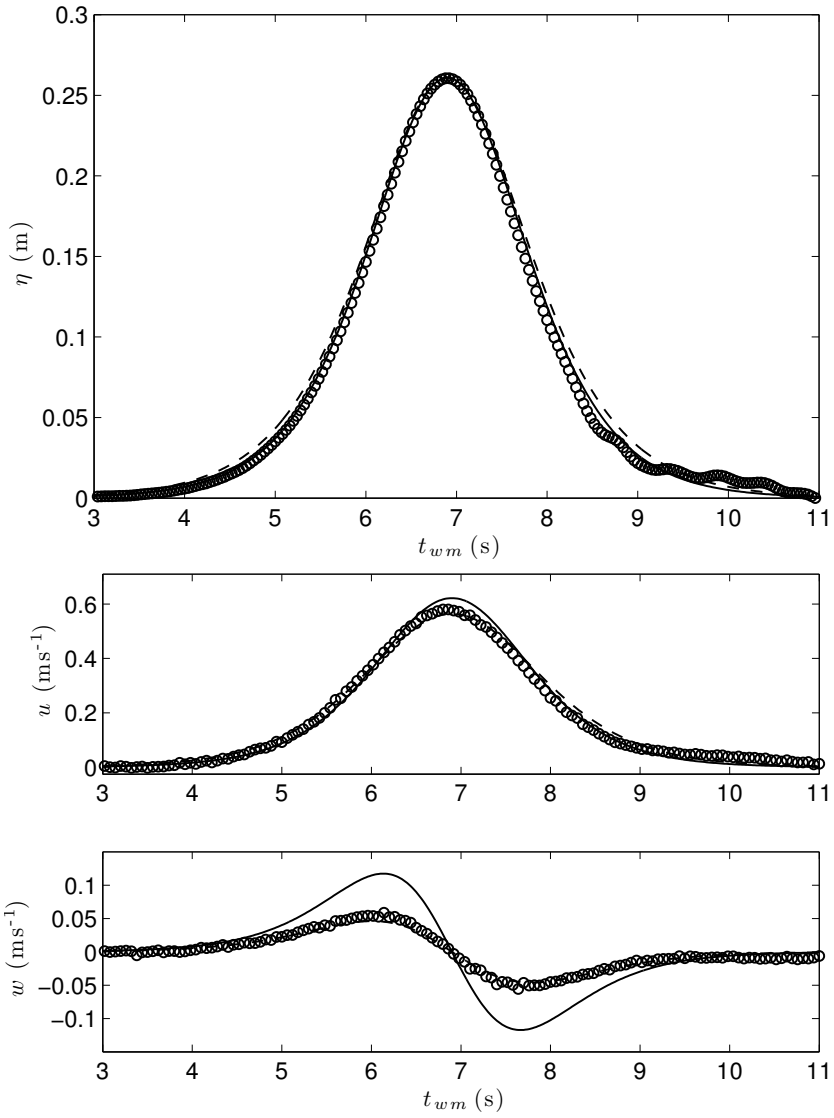

Figure 3.7: Free-surface displacement and velocity in the constant depth region for W5 (SU, H_0 = 0.261 m, ϵ_0 = 0.151): ∘, data; ——, Boussinesq solution; — —, Grimshaw solution. *Top*: free-surface displacement; *bottom*: velocity.

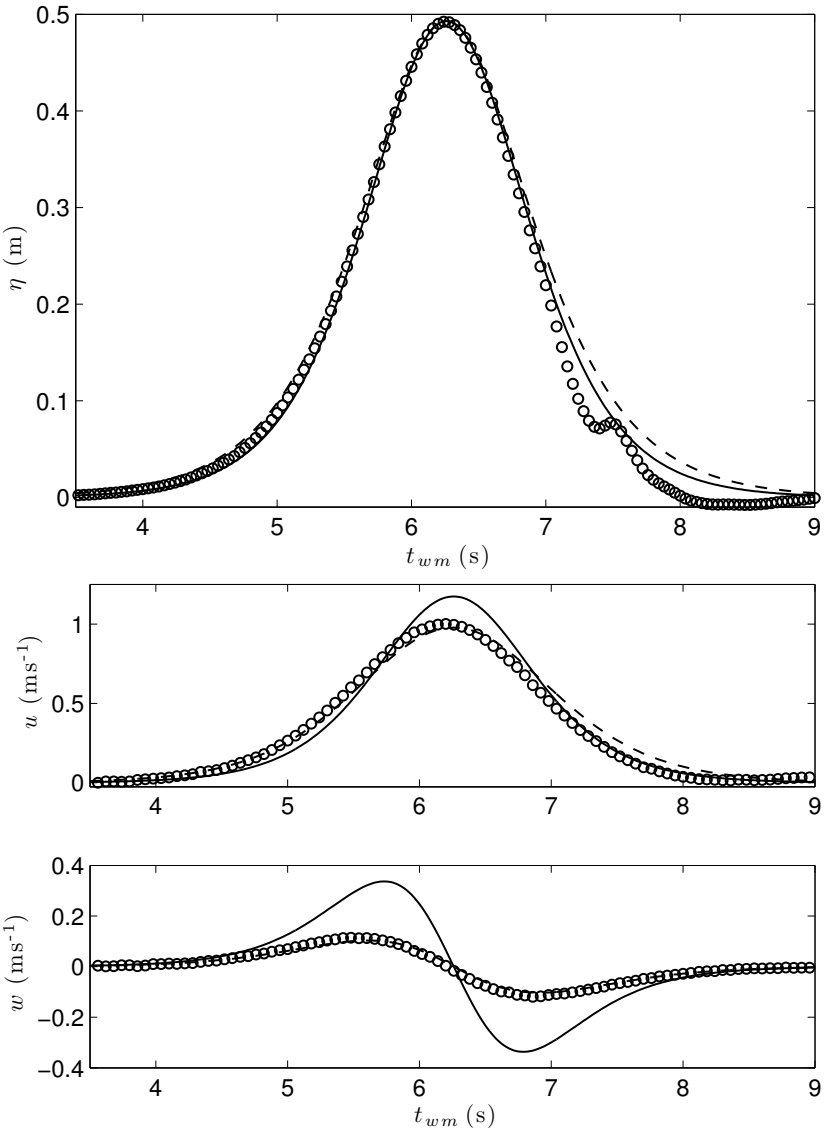

Figure 3.8: Free-surface displacement and velocity in the constant depth region for W10 (PL, H_0 = 0.493 m, ϵ_0 = 0.286): ∘, data; ——, Boussinesq solution; — —, Grimshaw solution. *Top*: free-surface displacement; *bottom*: velocity.

Computations of the free-surface could continue until the wave overturned and the overturning jet of the breaking wave reconnected with the fluid in front. Solitary waves were generated in the region of constant depth in their model using a numerical wavemaker simulating the motion of a physical piston-type wavemaker. To characterize the type of interaction a solitary wave has with the plane beach, Grilli *et al.* (1997) defined a solitary wave slope parameter as the ratio between the horizontal lengthscale of the wave to the horizontal length of the slope from the toe to the stillwater shoreline, which gives $S_0 = sL/h_0$. They chose the lengthscale, L, to be the length between the points that have the maximum slope on a solitary wave described by the Boussinesq solution. Using their numerical data for solitary wave breaking, they provided an empirical breaking criterion in terms of the slope parameter:

$$S_0 = 1.521\frac{s}{\sqrt{H_0/h_0}}; \text{breaker type} = \begin{cases} \text{No breaking}, & \text{if } S_0 > 0.37, \\ \text{Surging}, & \text{if } 0.3 < S_0 < 0.37, \\ \text{Plunging}, & \text{if } 0.025 < S_0 < 0.3, \\ \text{Spilling}, & \text{if } S_0 < 0.025. \end{cases} \tag{3.18}$$

The coefficient 1.521 could easily be dropped from Grilli *et al.*'s definition of the slope parameter, but has been kept as a useful reminder that its form and its value to demarcate different regimes of breaking are related to the Boussinesq solution to solitary waves.

In the incident waves generated in the experiments, two types of breakers were observed: surging breakers and plunging breakers (see Table 3.2). For plunging breakers, the overturning crest formed a jet that hit the dry land onshore of the stillwater shoreline and for surging breakers, the front face of the

Wave	H_0 (m)	ϵ_0 (-)	n (-)	S_0 (-)	Breaker type	R (m)	R_d (m)	T_s (s)	$U_{d,L2}$ (ms^{-1})	$Fr_{d,L2}$ (-)
W1	0.085	0.050	-0.17	0.57	NB	0.30	0.13	8.5	1.59	1.90
W2	0.128	0.074	-0.15	0.47	NB	0.46	0.17	8.5	1.95	2.31
W3	0.173	0.100	-0.13	0.40	NB	0.61	0.18	7.9	1.99	2.38
W4	0.226	0.131	-0.11	0.35	SU	0.75	0.20	7.8	1.97	2.35
W5	0.261	0.151	-0.11	0.33	SU	0.83	0.20	7.6	2.11	2.52
W6	0.295	0.171	-0.11	0.31	SU	0.90	0.19	7.4	2.21	2.59
W7	0.345	0.199	-0.11	0.28	PL	0.96	0.20	7.4	2.19	2.57
W8	0.410	0.237	-0.11	0.26	PL	1.09	0.21	7.5	2.29	2.72
W9	0.443	0.256	-0.11	0.25	PL	1.16	0.21	7.6	2.41	2.89
W10	0.493	0.286	-0.10	0.24	PL	1.23	0.21	7.7	2.54	2.97

Table 3.2: Integral properties of the climb and swash of solitary waves. NB is a non-breaking wave, SU is a surging breaker, PL is a plunging breaker.

wave became very steep as it moved past the stillwater shoreline and then collapsed. Visual observations confirmed that the breaker type matched the prediction of the slope parameter, S_0, defined in Eq. (3.18). Consequently, the results of the experiments are presented in terms of S_0 so that properties of the swash can be studied in terms of the breaker type.

The breaking point is defined as the location at which some part of the free-surface (usually near the wave crest) first becomes vertical; this definition corresponds to the mathematical interpretation of breaking that leads to the theoretical breaking criteria, Eq. (3.14) and (3.15). According to these criteria, all waves with $\epsilon_0 > 0.0517$ would break during uprush, whereas waves up to $\epsilon_0 = 0.1$ were observed to show no signs of breaking. Whether wave breaking occurred was decided by whether the surface of the water remained smooth and free of entrained air during the uprush, which was determined from the images taken by the overhead camera. The underestimation in the wave amplitude required

for breaking in the Synolakis (1987) theory is likely due to the shallow water approximation that neglects the effects of dispersion, which act against wave steepening and may locally alter whether the free-surface becomes vertical. The Synolakis (1987) theory is also restricted to incident solitary waves of low nonlinearity ($\epsilon_0 \ll 1$) and thus the theory may be inappropriate for the larger amplitude solitary waves used in this study.

Since there was no opportunity to observe the waves from the side in the experiments to gather data on instantaneous wave shape, it was not possible to locate the breaking points. If the wave broke, the location onshore of the stillwater shoreline at which the surface of the water was no longer smooth was identified by the overhead camera data. This location is called the collapse point, partly to distinguish it from the breaking point, but mainly because of the rapid process of conversion of potential energy to kinetic energy, analogous to bore collapse, that followed. The collapse points for all breaking waves, given in Table 3.3, fall within a narraw region onshore of the stillwater shoreline $0.1 < x < 0.3$ m as seen in figure 3.5, which also shows that surging breakers collapsed further onshore than plunging breakers. The time at which this collapse occured is called the collapse time and also given in Table 3.3. Figures 3.9 and 3.10 show measurements of the bed pressure and bed shear stress at location L2 and show fluctuations at times corresponding to the collapse times. The wave collapsing process made a large noise and imparted a sudden force on the beach. It is likely that the fluctuations seen in Figures 3.9 and 3.10 are the result of vibrations of the beach and the instruments; the consequences of the collapse process on the flow dynamics are not fully understood. Similar fluctuations at the collapse times are also observed in the bed shear stress and bed pressure signals at other locations.

Wave	S_0 (-)	Breaker type	Collapse location (m)	Collapse time (s)
W1	0.57	NB	-	-
W2	0.47	NB	-	-
W3	0.40	NB	-	-
W4	0.35	SU	0.71	16.9
W5	0.33	SU	0.66	16.7
W6	0.31	SU	0.58	16.3
W7	0.28	PL	0.60	16.0
W8	0.26	PL	0.54	15.6
W9	0.25	PL	0.55	15.3
W10	0.24	PL	0.54	15.1

Table 3.3: Breaking and collapse in the swash of solitary waves. NB is a non-breaking wave, SU is a surging breaker, PL is a plunging breaker. Collapse location gives the x-coordinate and the collapse time gives the time, t_{wm}, of the collapse points.

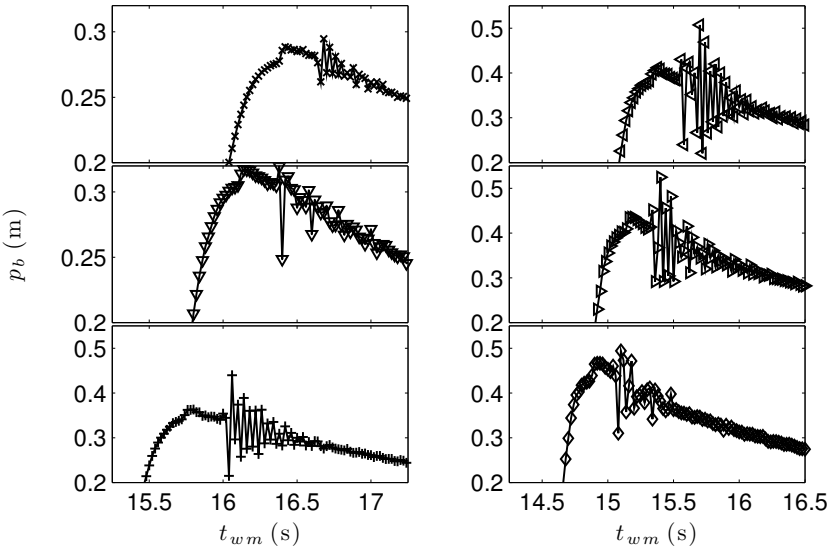

Figure 3.9: Bed pressure, p_b, of waves W5–10 at location L2 ($x = -1.21$ m, $h = 0.10$ m). Left panel, from top to bottom: W5–7; right panel, from top to bottom: W8–10.

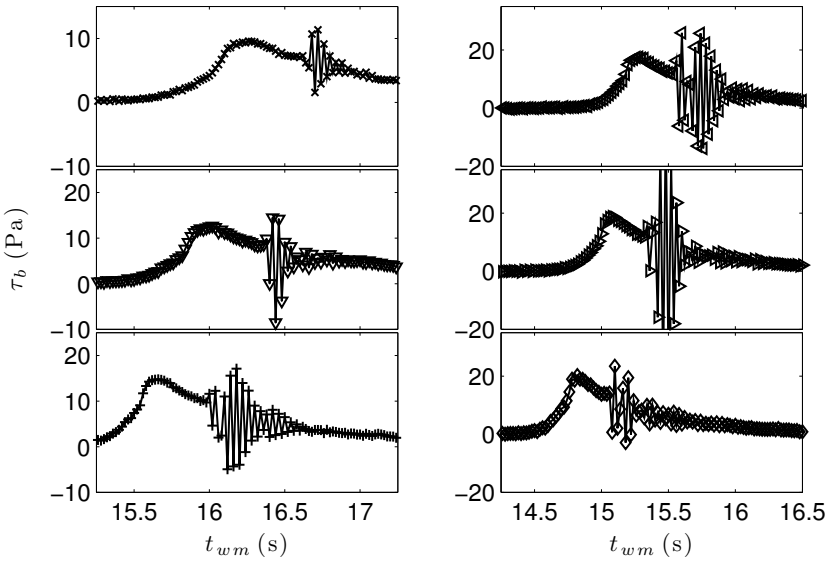

Figure 3.10: Bed shear stress, τ_b, of waves W5–10 at location L2 ($x = -1.21$ m, $h = 0.10$ m). Left panel, from top to bottom: W5–7; right panel, from top to bottom: W8–10.

3.5 Integral properties of the swash

For any swash event, there are integral properties that can be assigned to it. These include the run-up, the run-down and the time duration of the swash (swash period). The initial growth rate of the solitary wave as it moves from a region of constant depth to a plane sloping beach is also included in this section. For all cases, the results from the current, and where available previous studies, are re-scaled and discussed in terms of the solitary wave slope parameter, S_0.

3.5.1 Initial growth of wave height on sloping beach

As a solitary wave climbs the sloping beach, its height grows in a process referred to as shoaling. The shoaling of a solitary wave on a plane beach has

been previously studied, but no shoaling laws (theoretical or empirical) exist to predict the shoaling rate for a wide range of slopes and incident wave heights. Peregrine (1967) pointed out that as long as the water depth is much larger than the bottom boundary layer thickness and the celerity of the waveform is much higher than the velocity of the water so that rotational velocities in the boundary layer are not carried with the wave, the shoaling process is not influenced by the viscosity and the value of the offshore water depth, h_0, also does not influence shoaling results. Green's law, which states that $H \sim h^{-1/4}$, is originally a result from regular, linear, long waves (for a review, see Synolakis and Skjelbreia, 1993). Synolakis (1991) presented a theoretical result that showed that solitary waves would also evolve according to Green's law near the toe of the beach if the incident wave non-linearity at the toe of the beach is negligible. Thus, Green's law is only applicable to a limited range of parameters for solitary wave shoaling. The other known result is the Boussinesq law for shoaling of a solitary wave, which states that the wave height grows as $H \sim h^{-1}$. It was derived by assuming that the total energy of the wave is conserved without change of shape (Boussinesq, 1872), but in laboratory studies, wave steepening distorts the wave shape. Ippen and Kulin (1954) conducted extensive experiments testing solitary waves with incident non-linearities spanning the range $0.2 < \epsilon_0 < 0.7$ on slopes in the range $1/43.5 < s < 1/15.4$ and found that the shoaling rate decreases as the slope becomes steeper. Synolakis and Skjelbreia (1993) proposed a 'two-zone' evolution of solitary waves based on their own experimental results as well as those of Camfield and Street (1969); Saeki *et al.* (1971); Synolakis (1986); Skjelbreia (1987): a 'zone of gradual shoaling' following Green's law and a 'zone of rapid shoaling' just before wave breaking occurs following Boussinesq's law. As they noted, shoaling according to the Boussinesq law just before wave break-

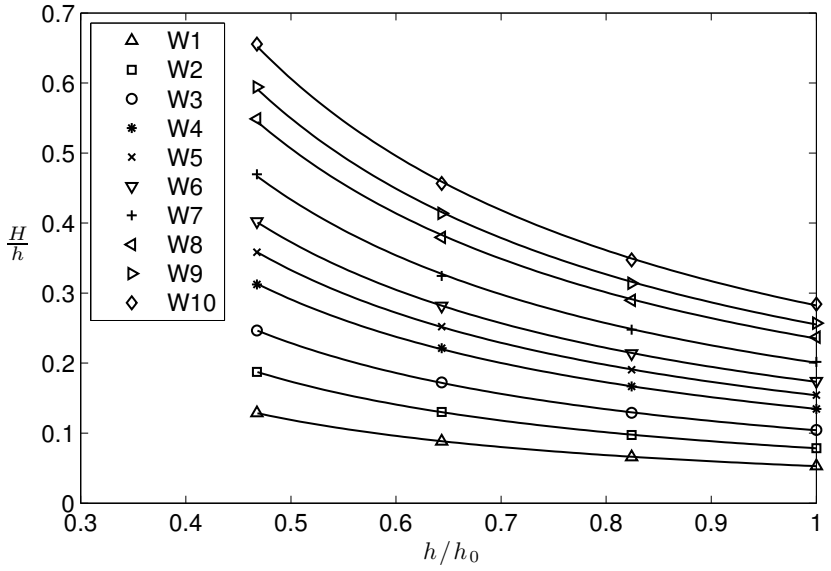

Figure 3.11: Growth of wave height as a function of local depth: *symbols*, wave gauge data; ——, power law fits, Eq. (3.19).

ing is a purely empirical result since the shape of the wave is changing very rapidly in this zone. Only data on slopes of $s = 1/20$ or milder are considered in their analysis. Hsiao *et al.* (2008) conducted experiments on a slope of $s = 1/60$ and found the two zone model to agree qualitatively with their data. Results of the numerical studies of Grilli *et al.* (1994) show that on the mildest slope they considered, $s = 1/35$, their results agreed qualitatively with the two-zone model; solitary waves approximately follow Green's law of shoaling until the local wave non-linearity becomes $H/h \approx 0.5$ and the Boussinesq law just before breaking. On steeper slopes, they concluded that there was no general law able to predict the shoaling rate and on very steep slopes, wave height is unchanged or even decreases as the wave travels up the slope.

The three wave gauges on the slope and the wave gauge at the toe provided wave height data for $0.47 < h/h_0 < 1$. The data from repeated waves was averaged and fitted to a power law of the form

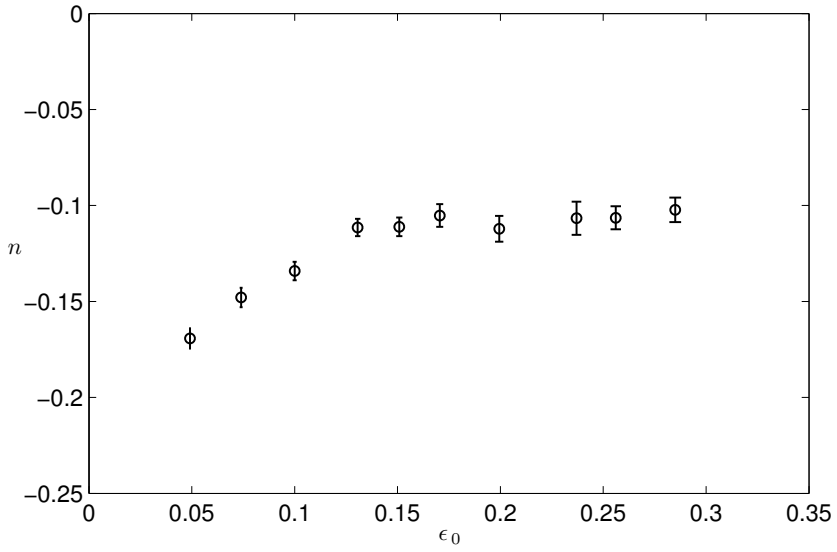

Figure 3.12: Shoaling rate exponent, n, calculated from a power law fit to data, Eq. (3.19), as a function of incident wave non-linearity, ϵ_0. Vertical bars show the uncertainty.

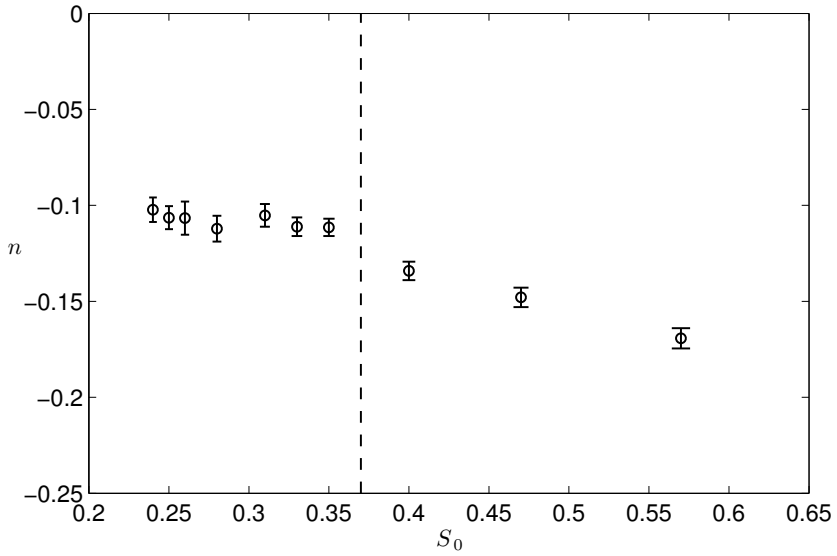

Figure 3.13: Shoaling rate exponent, n, calculated from a power law fit to data, Eq. (3.19), as a function of slope parameter, S_0. Vertical bars show the uncertainty. — —, Grilli *et al.* (1997) breaking criterion, Eq. (3.18).

$$H \propto h^n, \tag{3.19}$$

and plotted in Figure 3.11. The exponent of the power law, n, is given in Table 3.2 and plotted in Figure 3.12 as a function of the incident wave non-linearity, ϵ_0, and in Figure 3.13 as a function of the slope parameter, S_0. The uncertainty in the exponent, n, is found by applying the bootstrap technique (Efron and Tibshirani, 1993) to the residuals of the power law fit. The data show that the breaking waves (W4–10) covering a wide range of incident wave non-linearity, $0.13 < \epsilon_0 < 0.29$, and a wide range of breaker types, $0.24 < S_0 < 0.35$, the shoaling rate remains almost constant, $-0.12 < n < -0.10$. Over the full range of incident waves, the absolute value of the shoaling exponent decreases with increasing incident wave height but for this slope, there seems to be a limit near $n = -0.1$ for how slowly the wave height grows. For the smallest incident waves, the shoaling rate is approaching that of Green's law ($n = -0.25$). Thus, the data are consistent with the conclusions drawn in the literature: (i) the shoaling of a solitary wave is independent of the incident wave height if the incident wave non-linearity is non-negligible; (ii) when the incident wave non-linearity is small, the shoaling rate near the toe, before the local wave non-linearity grows too large, approaches Green's law. The current experiments do not show evidence of the two zones of shoaling, although Li and Raichlen (1998) pointed out that on steeper slopes, the waves tend to break before they have a chance to evolve due to the effect of the slope.

Figure 3.14 shows that wave fronts are very steep for waves W5-10 at location L2 (stillwater depth $h = 0.10$ m), although the waves still have smooth, rounded crests. Thus, the power law growth rate, n, derived from the fit to the

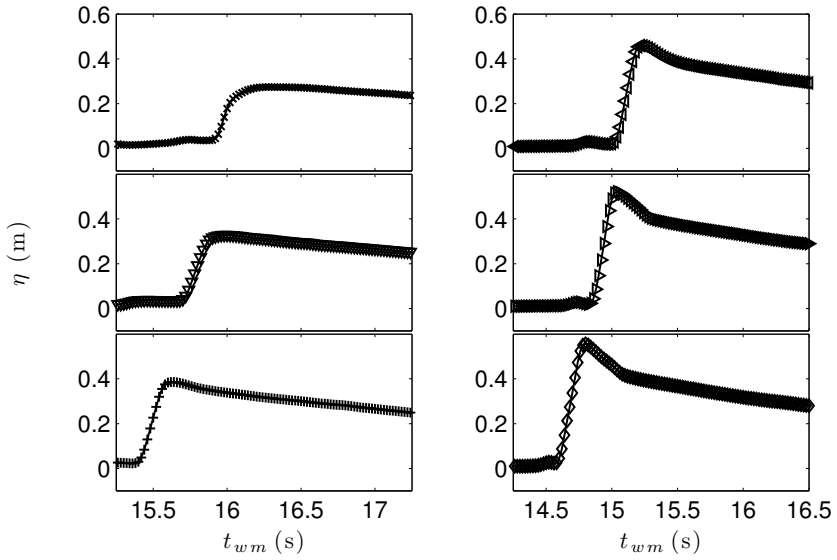

Figure 3.14: Free-surface displacement, η, of waves W5–10 at location L2 ($x = -1.21$ m, $h = 0.10$ m). Left panel, from top to bottom: W5–7; right panel, from top to bottom: W8–10.

wave height data from near the toe of the beach can be extrapolated to location L2 to see how well the initial growth rate of wave height predicts the wave height very close to the breaking point. The wave height at location L2 predicted in this way is denoted $H_{L2,n}$ and listed in Table 3.4 and compared to the measured wave height at location L2, H_{L2}. The actual wave height is lower than predicted suggesting that the growth rate near the stillwater shoreline is slower than the initial growth rate near the toe of the beach.

3.5.2 Run-up

Most studies of soltiary wave run-up do not consider the effects of bottom friction, turbulent dissipation or the surface tension and so the variables of interest are reduced to those shown in Figure 3.2. Analytical solutions are avail-

Wave	ϵ_0 (-)	H_{L2} (m)	$H_{L2,n}$ (m)
W1	0.050	0.119	0.148
W2	0.074	0.158	0.207
W3	0.100	0.205	0.264
W4	0.131	0.262	0.320
W5	0.151	0.274	0.366
W6	0.171	0.328	0.405
W7	0.199	0.386	0.478
W8	0.237	0.460	0.551
W9	0.256	0.522	0.598
W10	0.286	0.556	0.654

Table 3.4: Wave height of solitary waves at location L2 ($x = -1.21$ m, $h = 0.10$ m), measurements (H_{L2}) and predictions from growth rate near the toe of the beach ($H_{L2,n}$) fitted to Eq. (3.19)

able for the run-up of non-breaking solitary waves, Eq. (3.13) and (3.16), but only empirical relationships are available for breaking solitary waves (Li and Raichlen, 2003; Fuhrman and Madsen, 2008; Lo *et al.*, 2013). For periodic waves, a surf similarity parameter, introduced by Battjes (1974), has been used to predict run-up. Mei (1989) showed that the form of the surf similarity parameter for monochromatic waves is consistent with the breaking criterion from the Carrier and Greenspan (1958) theory and following this pattern for solitary waves, Lo *et al.* (2013) introduced a solitary wave surf parameter, $s(H_0/h_0)^{-9/10}$, where the breaking criterion from Synolakis (1987), Eq. (3.14), is reduced to its fundamental form by removing all constants. A similar solitary wave surf parameter, in which the exponent is -1 instead of $-9/10$, was introduced by Kobayashi and Karjadi (1994) and given an explicit form by Fuhrman and Madsen (2008).

Intuitively, for a given offshore water depth and slope of the plane beach, the highest run-up normalized by the incident wave height, R/H_0, should be

expected to occur for a solitary wave that almost breaks. The reasoning behind this intuition is that large waves that break far offshore form fully-developed bores by the time they reach the shoreline and in doing so they lose energy that would have been converted to potential energy of the run-up. On the other hand, for non-breaking waves, the higher the incident wave height, the larger the incoming energy and the larger the run-up is expected to be. So it is reasonable to expect that the dimensionless run-up, R/H_0, should be a function of a breaking criterion. The Grilli *et al.* (1997) slope parameter, S_0, is a reliable breaking criterion for a wide range of incident solitary wave non-linearities. In fact, the Synolakis (1987) run-up law, Eq. (3.13), can be re-expressed using the slope parameter to give

$$\frac{R}{H_0} = 3.49 S_0^{-\frac{1}{2}}, \tag{3.20}$$

which is valid for $S_0 \ll 5.28$. Fuhrman and Madsen (2008) also identified a form of S_0 without any constants as a solitary wave run-up parameter.

The run-up of solitary waves in the experiments is given in Table 3.2. The current data and data from previous laboratory studies of solitary wave run-up, R/H_0, is plotted together against the solitary wave slope parameter, S_0, in Figure 3.15. It can be seen that the highest run-up is in the vicinity of the breaking criterion, $S_0 = 0.37$, confirming that S_0 is a relevant parameter. If the highest dimensionless run-up is expected from waves that almost break, the data suggests that the Grilli *et al.* (1997) breaking criterion overestimates the incident wave amplitude and that waves of a slightly lower incident amplitude are likely to break so that the breaking criterion should be $S_0 \approx 0.4 - 0.5$. Given that Grilli *et al.*'s numerical model was two-dimensional and solved the inviscid Euler's

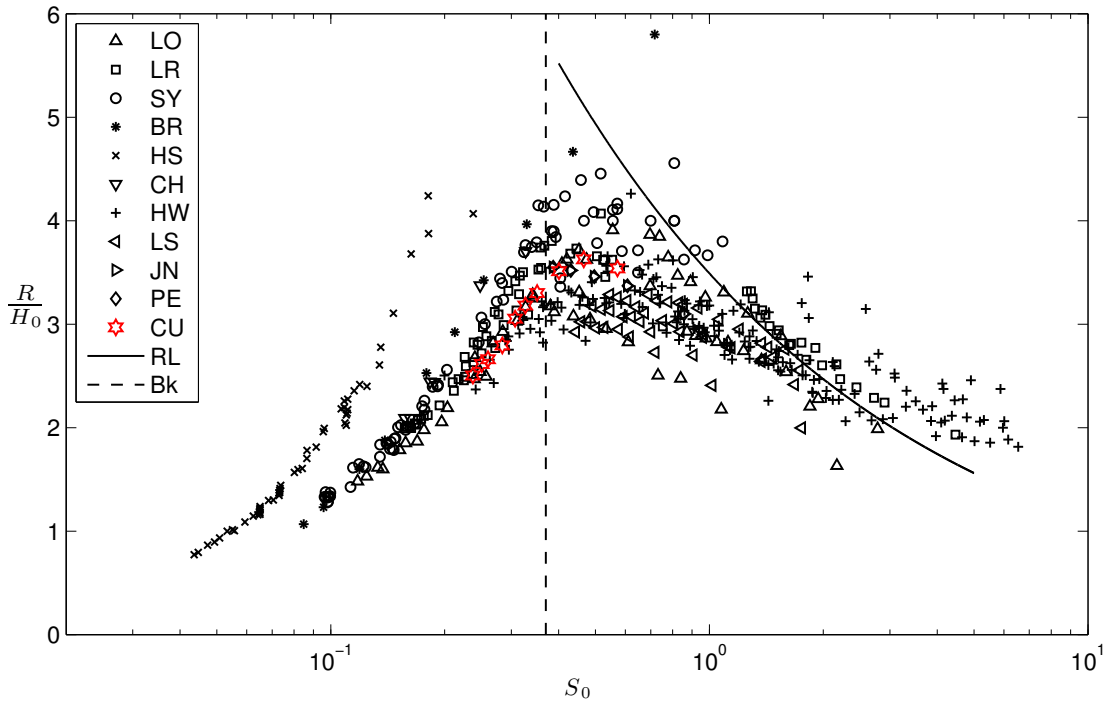

Figure 3.15: Run-up of solitary waves plotted against the slope parameter: *LO*, Lo *et al.* (2013); *LR*, Li and Raichlen (2001, 2002); *SY*, Synolakis (1987); *BR*, Briggs *et al.* (1995); *HS*, Hsiao *et al.* (2008); *CH*, Chang *et al.* (2009); *HW*, Hall and Watts (1953); *LS*, Langsholt (1981); *JN*, Jensen *et al.* (2003); *PE*, Pedersen *et al.* (2013); *CU*, Current data; ——, Synolakis (1987) run-up law, Eq. (3.20); — —, Grilli *et al.* (1997) breaking criterion, Eq. (3.18).

equations and thereby did not include effects of spanwise instabilities and viscosity (both of which might be important in the early onset of breaking), it is reasonable to expect that breaking in laboratory experiments starts to happen earlier than predicted by the numerical model. The Hsiao *et al.* (2008) data was conducted at a slope of $s = 1/60$ and shows the same trend as the rest of the data for which the range of slopes spans $1/30 \leq s \leq 1$. Plotted against the slope parameter, the data also show that Synolakis's run-up law, Eq. (3.20), provides an upper bound for the run-up of non-breaking waves (as might be expected from a theory that doesn't consider frictional effects) for values of the slope parame-

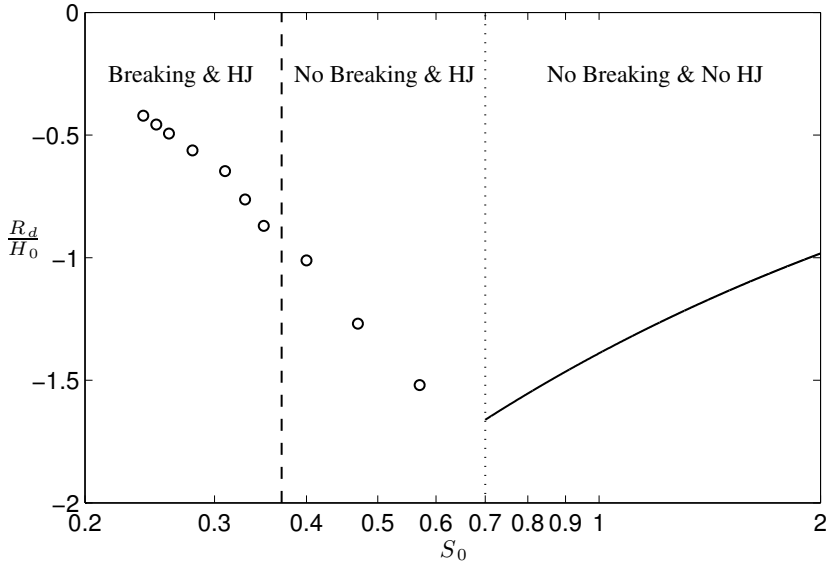

Figure 3.16: Run-down of solitary waves plotted against the slope parameter: ∘, data; ——, Madsen and Schäffer (2010) run-down law, Eq. (3.21); — —, Grilli *et al.* (1997) breaking criterion, Eq. (3.18); ·····, $S_0 = 0.70$ (value of slope parameter that corresponds to downrush breaking criterion, Eq. (3.15), for $s = 1/12$).

ter larger than $S_0 \approx 0.54$. The Hall and Watts (1953) data shows higher run-ups than Eq. (3.20), but it is known that the generation mechanism for their solitary waves was rudimentary and thus the run-up measurements are of limited accuracy. The current data differs somewhat from previous data since it is taken at a much larger scale than typical laboaroty measurements. However, it fits within the scatter of the rest of the data. Even though the parameter introduced by Lo *et al.* (2013) also provides a collapse of the data, Figure 3.15 shows that S_0 provides a credible parameterization of the run-up as well as the breaker type and that the two phenomena are invariably linked.

3.5.3 Run-down

When the supercritical downrush flow meets the near-quiescent offshore water body, a hydraulic jump is created. This hydraulic jump is also referred to as downrush breaking, due to the similarities it shows to conventional wave breaking during uprush. The occurrence of the hydraulic jump was identified by the overhead cameras and the region where it occurred for all waves is shown in Figure 3.5. The Madsen and Schäffer (2010) downrush breaking criterion, Eq. (3.15), predicts that for this slope ($s = 1/12$), all waves with $\epsilon_0 > 0.0325$ would exhibit downrush breaking. All incident waves were above this threshold and they were all observed to break during downrush creating a hydraulic jump. As previously mentioned, the run-down result in the Madsen and Schäffer (2010) theory is for waves that do not break during downrush, and since all waves in this study showed evidence of a hydraulic jump during downrush, a comparison to the theory cannot be made. For waves where a hydraulic jump does occur, the run-down is defined as the vertical extent below the stillwater shoreline that the hydraulic jump occurs and this data is given in Table 3.2. Unlike uprush breaking, no general downrush breaking criterion in terms of S_0 based on solutions to fully non-linear potential flow equations exists, but the run-down is nonetheless plotted against the solitary wave slope parameter, S_0, in Figure 3.16. The Madsen and Schäffer (2010) run-down result, Eq. (3.16), is re-expressed using the slope parameter to give

$$\frac{R_d}{H_0} = -1.39 S_0^{-\frac{1}{2}}, \tag{3.21}$$

and also plotted in Figure 3.16. Vertical lines demarcate the values for S_0 for which the wave will break during uprush, the wave will not break during up-

rush but will create a hydraulic jump during downrush, or the wave will not break during uprush or downrush. Similar to the run-up, the trend is that the magnitude of R_d/H_0 decreases either side of the value of S_0 where the downrush breaking is first predicted to occur for this slope. The effects of friction on downrush breaking are expected to be larger than those for uprush breaking because friction is expected to cause a reduced run-up, which causes the downrush to begin earlier. Due to the effects of friction, the downrush flow meets the main water body with less momentum than a frictionless case, causing an earlier hydraulic jump.

The strength of the hydraulic jump is determined by computing the Froude number before the hydraulic jump occurs. Figure 3.5 shows that the hydraulic jumps for all waves occur offshore of location L2. The maximum offshore-directed velocity measured by the ADV at location L2 is denoted as $U_{d,L2}$ and also listed in Table 3.2. The value of the local water depth when the velocity reaches $U_{d,L2}$ is typically around 7 cm. After the water depth decreases beyond this point, the ADV is no longer able to make reliable measurements. $U_{d,L2}$ is used as an approximate depth-averaged velocity in the flow at location L2 and combined with the measurement of the free-surface elevation at that time to estimate the maximum Froude number that the flow at location L2 reaches, $Fr_{d,L2}$. The values for this estimated Froude number are also shown in Table 3.2. It can be seen that Froude numbers as large as $Fr_{d,L2} \approx 3$ are reached for wave W10.

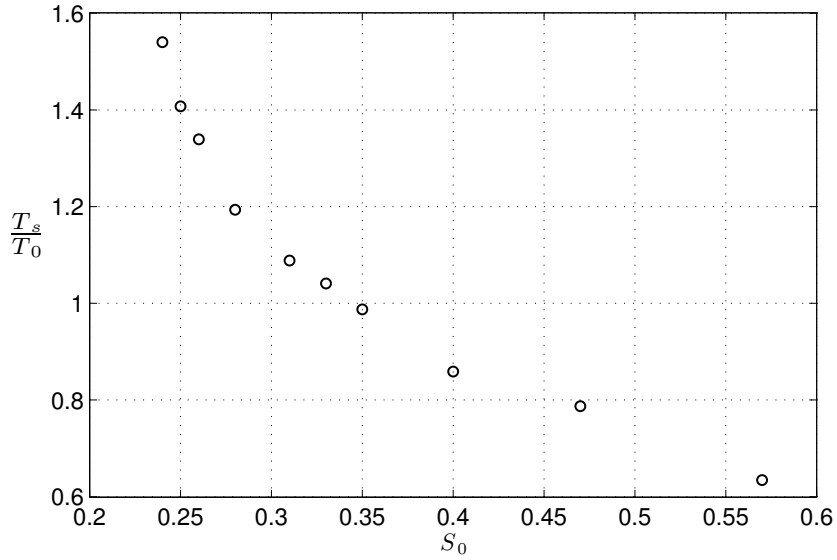

Figure 3.17: Dimensionless swash period, T_s/T_0, plotted against the slope parameter, S_0.

3.5.4 Swash period

The time duration of the swash is called the swash period and denoted by T_s herein. It is defined as the time from when the wave collapses in the uprush to the time when the hydraulic jump forms during downrush. For non-breaking waves, the swash period is defined as the time from when the shoreline starts to move in uprush until the hydraulic jump forms in the downrush. Table 3.2 gives the data of T_s. The ratio of the swash period to the incident wave period is then T_s/T_0 and it is plotted in Figure 3.17. The data shows that as S_0 decreases, i.e., as wave breaking becomes more pronounced, the dimensionless swash period increases. Therefore the swash period does not increase with incident wave period. For the wave cases that are barely breaking ($S_0 \approx 0.37$), $T_s/T_0 \approx 1$, whereas for non-breaking waves, $T_s/T_0 < 1$, and for breaking waves, $T_s/T_0 > 1$.

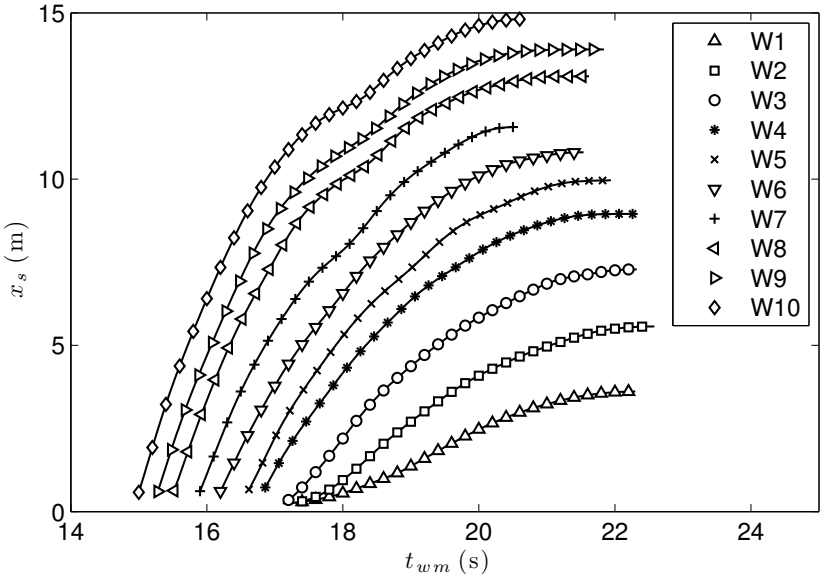

Figure 3.18: Shoreline position, $x_s(t)$, for all waves: W1–3, NB; W4–6, SU; W7–10, PL.

3.6 Shoreline motion

The tracked shoreline position along the slope, $x_s(t)$, for all waves is plotted in Figure 3.18. A second-order accurate finite difference scheme was used to obtain the shoreline velocity along the slope, $u_s(t)$, and plotted in Figures 3.19–3.20 against the shoreline position. For waves that break, the shoreline motion tracking begins when it is already moving with a large velocity immediately following the collapse point. During the breaking process, the shoreline position is undefined as the wave crest curls over the stillwater shoreline. The shoreline accelerations seen in the initial stages of the surging and plunging breakers are caused by the steepness of the wave front (a pressure gradient that is favorable in the onshore direction), which is lost when the collapse is completed. A similar feature was observed in numerical study of Hibberd and Peregrine (1979). For the plunging breakers, the collapse point occurs just after the still-

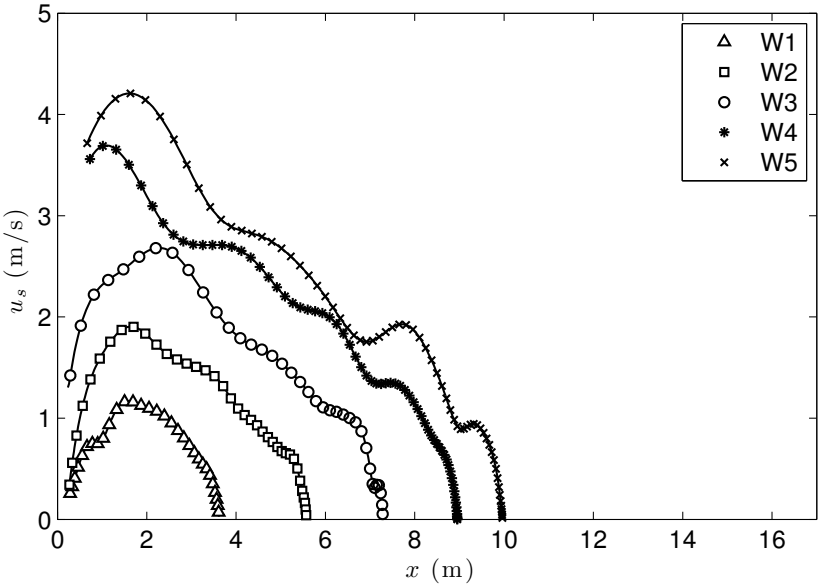

Figure 3.19: Shoreline velocity, $u_s(t)$, for W1–5. (W1–3, NB; W4–6, SU; W7–10, PL.)

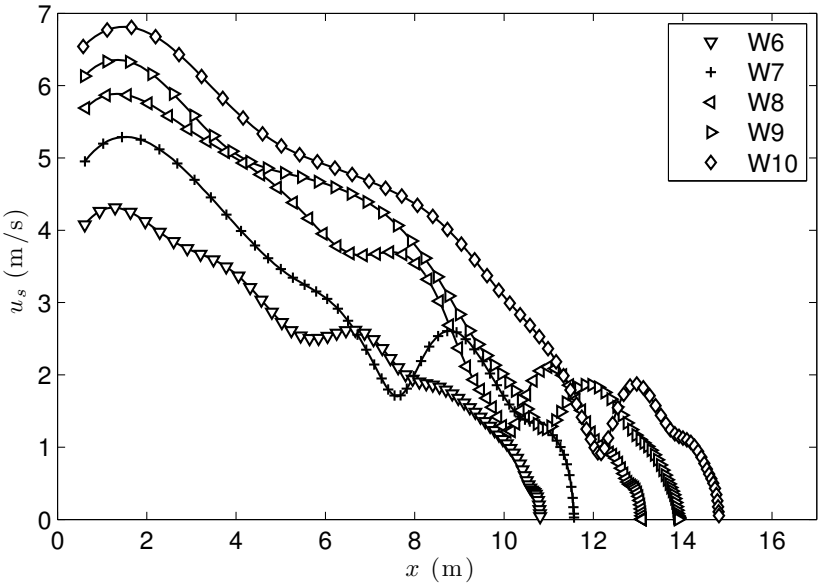

Figure 3.20: Shoreline velocity, $u_s(t)$, for W5–10. (W1–3, NB; W4–6, SU; W7–10, PL.)

water shoreline so that the shoreline shows a very short acceleration phase. For the surging breakers, the collapse point occurs further onshore (see Figure 3.5) and thus the shoreline acceleration persists slightly longer. For non-breaking waves, the shoreline accelerates gradually from rest at the stillwater shoreline and reaches a maximum velocity before a gradual deceleration until the run-up is reached.

The shoreline velocity of the plunging breakers, *e.g.*, W9 and W10 in Figure 3.20, show a sudden increase near x = 11 m before falling to zero when the run-up is reached. This feature was also observed by Yeh *et al.* (1989) and Zhang and Liu (2008), who called it a 'mini-collapse'. Zhang and Liu (2008) examined the velocity field in the vicinity of the mini-collpase and showed that there was a build up of fluid behind the swash tip due to the effects of bed friction at the swash tip. The built up fluid resembled a small bore that created a 'mini-collapse' when it caught up to the shoreline.

3.6.1 Swash initiation shoreline velocity for breaking waves

The very steep wave fronts of waves W5–10 in Figure 3.14 show that the waves have undergone sufficient non-linear steepening to make the use of NSWE, Eq. (3.1), appropriate. The steep fronts can be treated as bore fronts in the context of Eq. (3.1) and the wave heights at location L2 as the height of the bores. If the bore strength is high enough, we expect bore evolution to be governed by Whitham's formula, Eq. (3.5), as the bore approaches the stillwater shoreline. Then, the swash initiation shoreline velocity, U_s, is expected to be well-predicted by the solution to Whitham's formula, Eq. (3.8), in which the bore height at lo-

Wave	ϵ_0 (-)	H_{L2} (m)	$(H/h)_{L2}$ (-)	M_{L2} (-)	$U_{s,p}$ (ms^{-1})	U_s (ms^{-1})	$U_{s,m}$ (ms^{-1})	$U_{\alpha,(x>0)}$ (ms^{-1})
W1	0.050	0.119	1.19	-	-	-	1.2	-
W2	0.074	0.158	1.58	-	-	-	1.9	-
W3	0.100	0.205	2.05	-	-	-	2.7	-
W4	0.131	0.262	2.62	1.25	4.1	3.6	3.7	4.8
W5	0.151	0.274	2.74	1.26	4.2	3.7	4.2	5.0
W6	0.171	0.328	3.28	1.31	4.7	4.1	4.3	5.3
W7	0.199	0.386	3.86	1.36	5.2	5.0	5.3	5.4
W8	0.237	0.460	4.60	1.41	5.7	5.7	5.9	5.5
W9	0.256	0.522	5.22	1.46	6.2	6.2	6.4	5.6
W10	0.286	0.556	5.56	1.49	6.5	6.6	6.8	5.7

Table 3.5: Properties of solitary waves at location L2 ($x = -1.21$ m, $h = 0.10$ m), measurements (U_s) and predictions ($U_{s,p}$) of the swash initiation shoreline velocity, and constant value of the characteristic variable, α, as determined from measurements in the swash ($U_{\alpha,(x>0)}$).

cation L2 provides the initial condition. Table 3.5 lists the values of the swash initiation shoreline velocity: (i) predicted using Whitham's formula, $U_{s,p}$; (ii) measured immediately after collapse, U_s; (iii) measured maximum during uprush, $U_{s,m}$.

Figure 3.21 plots these predicted and measured swash initiation shoreline velocities, made dimensionless by the offshore linear, long wave celerity, $\sqrt{gh_0}$. There are two sources of uncertainty in the measurement of the shoreline velocity: the truncation error in the finite difference scheme to calculate the shoreline velocity from the shoreline position data and the uncertainty in the position of the shoreline at each datapoint. The uncertainty in the shoreline position dominates in this case and it is propagated to an uncertainty in the shoreline velocity to give the error bars in the measured swash initiation shoreline velocity (*e.g.*, Taylor, 1997). The overall agreement between the predicted and measured val-

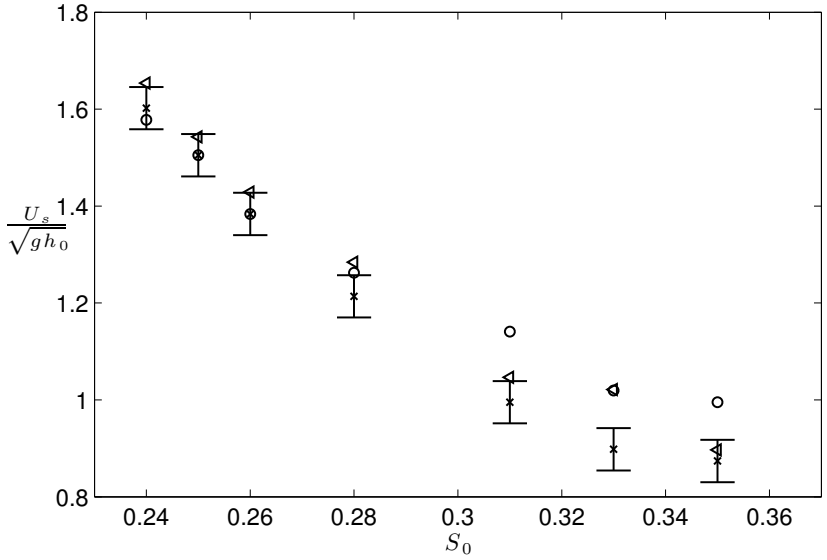

Figure 3.21: Swash intitiation shoreline velocity – comparison of predictions and measurements: ∘, $U_{s,p}$; ×, U_s; ◁, $U_{s,m}$. Error bars represent uncertainty in measurement of the shoreline velocity and are not shown for the maximum measure shoreline velocity, $U_{s,m}$, for reasons of space.

ues of the swash initiation shoreline velocity verifies the theory of Ho and Meyer (1962), who showed that the evolution of the bore during collapse is only very weakly influenced by the details of the bore. However, it can be seen that while the predicted values for the swash initiation shoreline velocity match the measured values very well for plunging breakers ($0.025 < S_0 < 0.3$), the measured values for the surging breakers ($0.3 < S_0 < 0.37$) are slightly lower than those predicted. The source of this discrepancy for surging breakers is likely the fact that surging breakers do not completely collapse by the time the shoreline starts to move. A similar agreement in the predicted and measured swash initiation shoreline velocity was also observed by Yeh *et al.* (1989), who found that for undular bores (or weak bores), the swash initiation shoreline velocity predicted by Whitham's formula matched the measured value, but it occurred slightly onshore of the stillwater shoreline. The description of the collapse of undular bores

matches that of the plunging breakers in this study, *i.e.*, the collapse occurred via overturning of the fluid onto the dry land onshore of the stillwater shoreline. For fully-developed bores (or strong bores), Yeh *et al.* (1989) found that the bore exchanges momentum with the wedge-shaped fluid in front of the bore and pushes this fluid onshore to initiate the swash. This momentum exchange causes a lower initial shoreline velocity than predicted by Whitham's formula. Such a transition might be expected for solitary waves that form spilling breakers.

Figure 3.21 also shows that the swash initiation shoreline velocity for solitary waves that barely break ($S_0 \approx 0.35$) is close to the offshore linear, long wave speed, $\sqrt{gh_0}$. As S_0 decreases towards plunging breakers, U_s increases to around $1.6\sqrt{gh_0}$, and it may increase further for even larger waves. Overall, the relationship between $U_s/\sqrt{gh_0}$ and S_0 provides a link between the velocity scale of the swash, *i.e.*, the swash initiation shoreline velocity, and the offshore water depth by using S_0 to predict the breaker type. There may be an additional slope dependency not captured by S_0 since the slope is of primary importance in determination of increases in wave height during shoaling.

3.7 Swash flow evolution

Given that the bore collapse theory is able to predict the swash initiation shoreline velocity, it is natural to ask whether the flow evolution in the swash follows the swash solution, Eq. (3.10), since it was shown that bore collapse provides a valid initial condition for the swash solution (section 3.2.1). Figure 3.22 and Figure 3.23 plot the characteristic variable, α, as a function of time for all locations

onshore of the stillwater shoreline ($x > 0$) for a surging breaker, wave W5, and a plunging breaker, wave W10, respectively. The value of $\alpha = \overline{u} + 2c + gst_s$ is calculated from measurements: the free-surface elevation is used to compute the local long wave celerity, $c = \sqrt{g\eta}$, the near-bed velocity, u, is assumed to approximate the depth-averaged velocity, $\overline{u}$, during the mid-swash duration when ADV data is available (vertical variation of horizontal velocity in the swash is weak, *e.g.*, Pedersen *et al.*, 2013), and the collapse point is taken to be $(x, t) = (0, 0)$. Since α was found not vary appreciably in x for all breaking waves, Figure 3.24 plots α as a function of time for all breaking waves (W4–10). The data in Figure 3.24 shows that $\alpha \approx$ const. throughout the swash flow, except near the swash tip, where the effects of bed friction reduces the depth-averaged velocity locally reducing α, and towards the end of the downrush, where the effects of bed friction delays the water depth falling to zero increasing α. A constant α is in accordance with the swash solution, but unlike the swash solution, the data in Figure 3.24 shows that the constant is not necessarily equal to the measured swash initiation shoreline velocity, U_s. By taking a time-average of the the values of α in Figure 3.24 during the mid-swash duration where $\alpha \approx$ const., the constant value of α in the swash is calculated. This constant value is called $U_{\alpha,(x>0)}$ and is listed in Table 3.5 for all breaking waves (W4–10).

Figures 3.25–3.27 plot the free-surface elevation and the near-bed velocity for the surging breakers (W4–6) at two separate locations (L5, L8) and compare the data to the swash solution, Eq. (3.10), which is calculated using $U_{\alpha,(x>0)}$ instead of the measured U_s. Figures 3.28–3.31 show the same plots for the plunging breakers (W7–10) at the same locations (L5, L8). The data match the swash solution very well, as expected since the value of $U_{\alpha,(x>0)}$ was determined from the data. However, the more meaningful result is that the flow evolution in the swash for

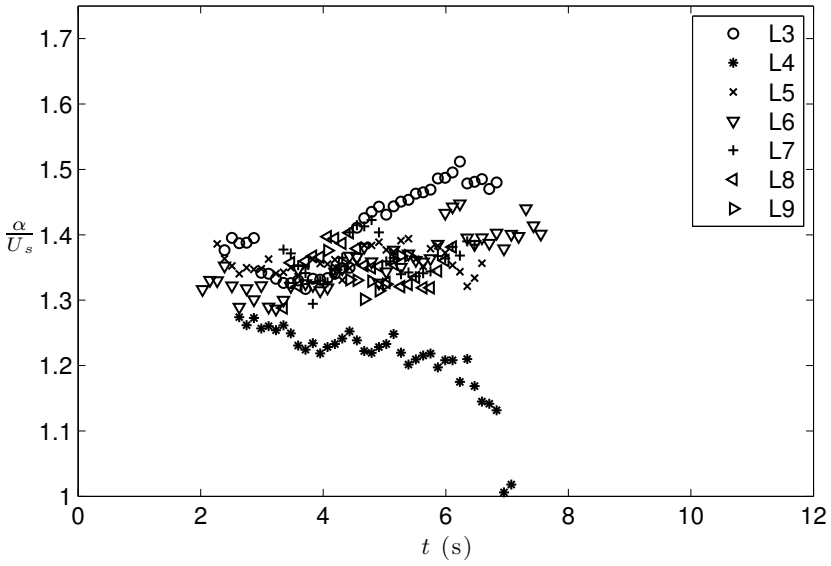

Figure 3.22: The characteristic variable, α, calculated from experimental data and made dimensionless by the measured swash initiation shoreline velocity, U_s, as a function of time for wave W5 (SU, H_0 = 0.261 m, ϵ_0 = 0.151) for locations onshore of the stillwater shoreline, L3–9.

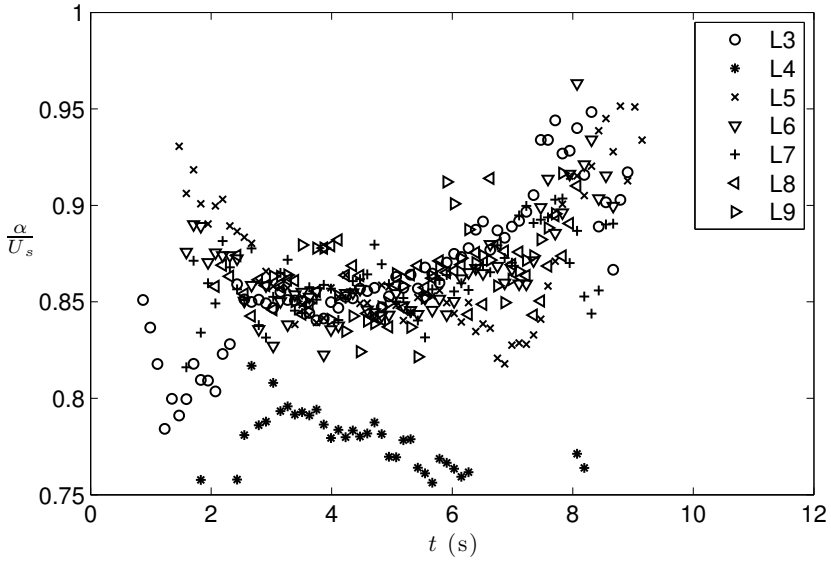

Figure 3.23: The characteristic variable, α, calculated from experimental data and made dimensionless by the measured swash initiation shoreline velocity, U_s, as a function of time for wave W10 (PL, H_0 = 0.493 m, ϵ_0 = 0.286) for locations onshore of the stillwater shoreline, L3–9.

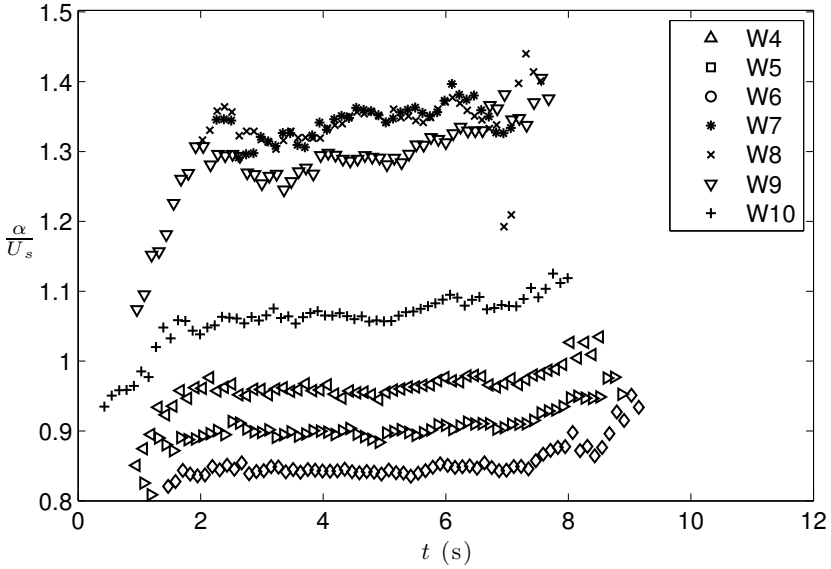

Figure 3.24: The characteristic variable, α, calculated from experimental data and made dimensionless by the measured swash initiation shoreline velocity, U_s, as a function of time for all breaking waves: W4–10.

breaking solitary waves does follow the swash solution, since $\alpha \approx$ const., but the constant, which is also the only free-parameter in the swash solution, must be correctly scaled. Then, important quantities such as the maximum flow depth and time of flow reversal at a given location can be accurately determined. With the knowledge that the flow evolution of the swash of breaking solitary waves follows the swash solution, the following salient features of this flow can be pointed out. The time of flow reversal does not necessarily occur in phase with the maximum flow depth – the free-surface starts to decrease while the velocity is still positive. Flow reversal occurs earlier further down the slope and the location where flow reversal occurs climbs the slope stretching and thinning the swash flow. The free-surface gradient, $\partial\eta/\partial x$, is positive, or equivalently, the total fluid particle acceleration is negative, for the majority of the swash. These features are discussed in more detail in the context of field measurements by

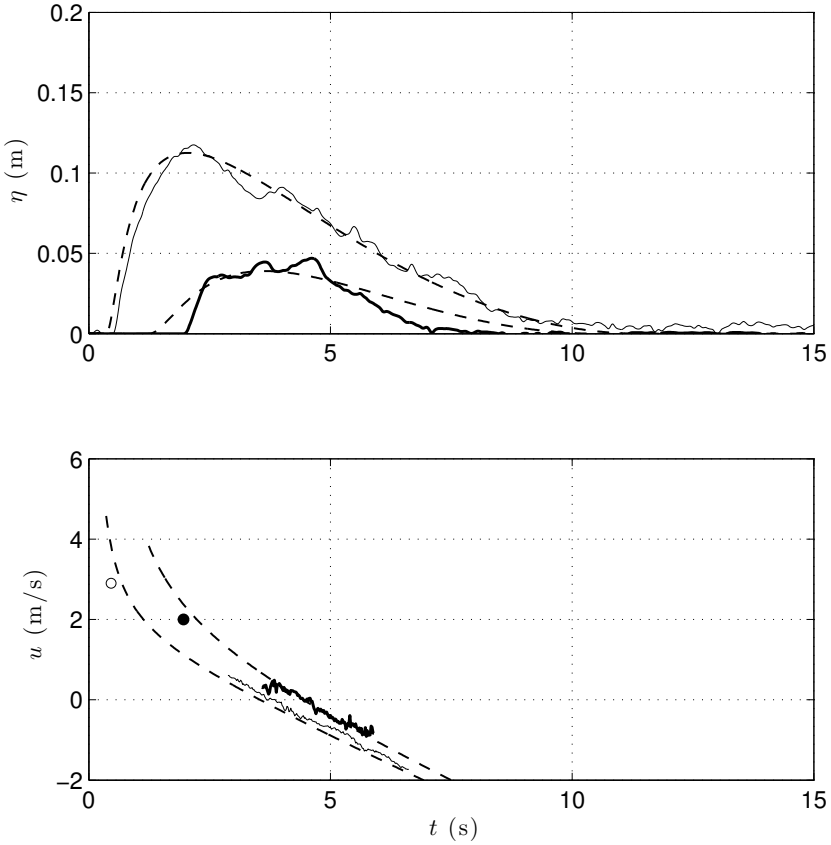

Figure 3.25: Free-surface elevation, η, and near-bed velocity, u, for W4 (SU, H_0 = 0.226 m, ϵ_0 = 0.131) at locations L5 (x = 2.42 m), L8 (x = 6.10 m) and comparisons to swash solution, Eq. (3.10), scaled using $U_{\alpha,(x>0)}$. Top panel: ——, η at L5; ——, η at L8; — —, η from swash solution, Eq. (3.10). Bottom panel: ——, u at L5; ——, u at L8; — —, u from swash solution, Eq. (3.10); ∘, shoreline velocity, u_s, at L5; •, shoreline velocity, u_s, at L8.

Baldock and Hughes (2006).

In Figures 3.26 and 3.27, the hollow and filled circles show the measurement of velocity of the shoreline at locations L5 and L8, respectively. At location L5, the shoreline arrives at the time predicted by the swash solution and the frictionless shoreline motion, Eq. (3.9), but the velocity is lower than predicted due to the effects of bed friction. Consequently, at location L8, the shoreline arrives at a later time than predicted by the frictionless shoreline motion. In Figures

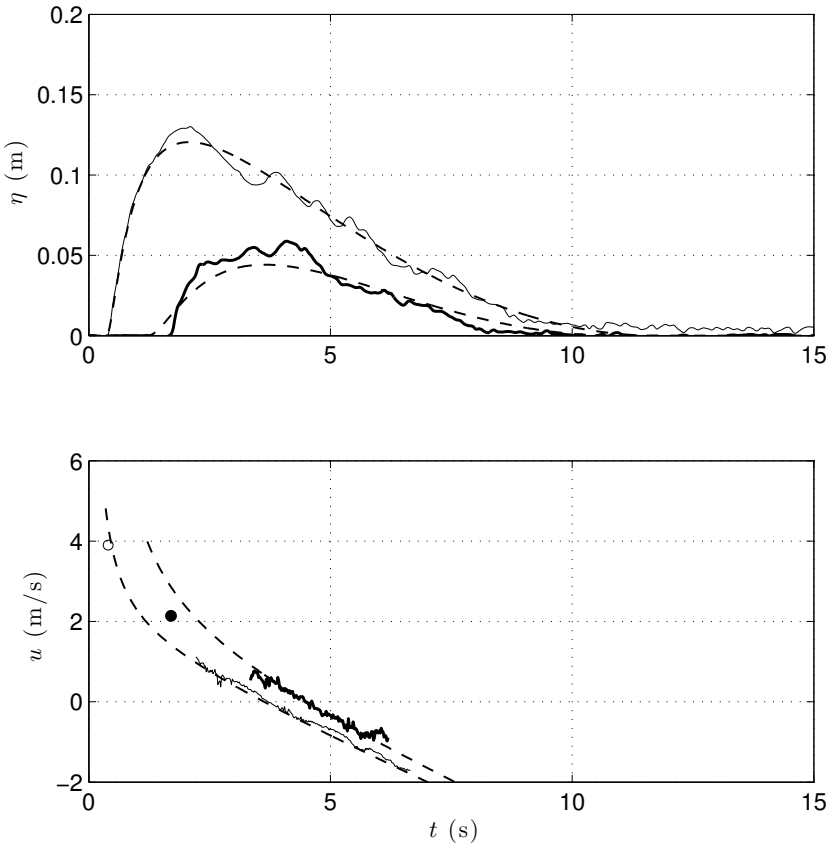

Figure 3.26: Free-surface elevation, η, and near-bed velocity, u, for W5 (SU, H_0 = 0.261 m, ϵ_0 = 0.151) at locations L5 (x = 2.42 m), L8 (x = 6.10 m) and comparisons to swash solution, Eq. (3.10), scaled using $U_{\alpha,(x>0)}$. Top panel: ——, η at L5; ——, η at L8; — —, η from swash solution, Eq. (3.10). Bottom panel: ——, u at L5; ——, u at L8; — —, u from swash solution, Eq. (3.10); ∘, shoreline velocity, u_s, at L5; •, shoreline velocity, u_s, at L8.

3.29 and 3.31, the shoreline velocity at location L5 and L8 matches, or exceeds the predicted value from the frictionless motion due to the acceleration of the shoreline during the wave collapse process.

To compare the various estimates and measurements of the swash initiation shoreline velocity, Figure 3.32 plots the direct measurement of the initial shoreline velocity, U_s, the prediction of the swash initiation shoreline velocity from wave height measurements at location L2, $U_{s,p}$, and the costant value of the

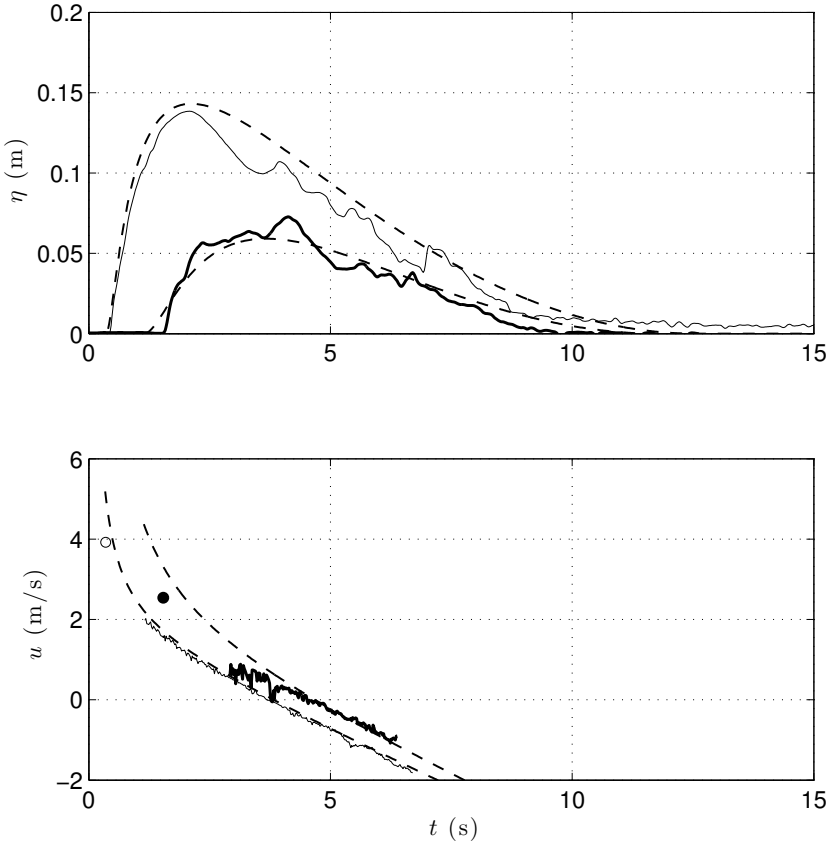

Figure 3.27: Free-surface elevation, η, and near-bed velocity, u, for W6 (SU, H_0 = 0.295 m, ϵ_0 = 0.171) at locations L5 (x = 2.42 m), L8 (x = 6.10 m) and comparisons to swash solution, Eq. (3.10), scaled using $U_{\alpha,(x>0)}$. Top panel: ——, η at L5; ——, η at L8; — —, η from swash solution, Eq. (3.10). Bottom panel: ——, u at L5; ——, u at L8; — —, u from swash solution, Eq. (3.10); ∘, shoreline velocity, u_s, at L5; •, shoreline velocity, u_s, at L8.

characteristic variable, α, determined from measurements in the swash, $U_{\alpha,(x>0)}$, against the slope parameter, S_0. As S_0 decreases, i.e., as breaker type moves from surging to plunging, the relative magnitudes of the three swash initiation shoreline velocity scales changes from $U_{\alpha,(x>0)} > U_{s,p} > U_s$ to $U_{\alpha,(x>0)} < U_{s,p} < U_s$, although the difference between U_s and $U_{s,p}$ is not appreciable for the plunging breakers.

For surging breakers, the corresponding physical interpretation is that the

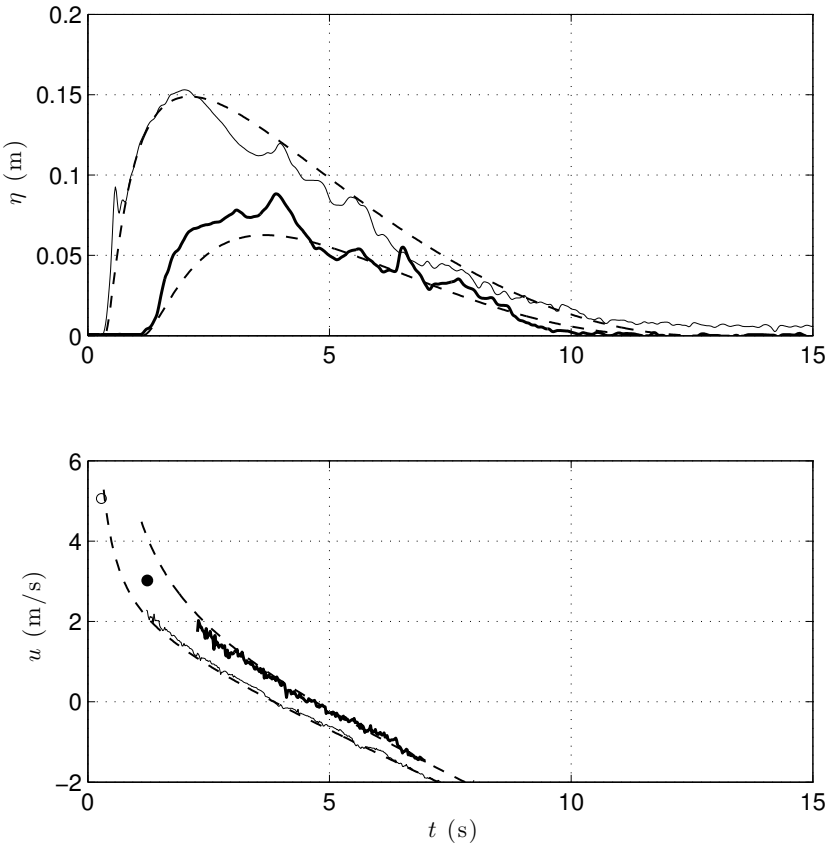

Figure 3.28: Free-surface elevation, η, and near-bed velocity, u, for W7 (SU, H_0 = 0.345 m, ϵ_0 = 0.199) at locations L5 (x = 2.42 m), L8 (x = 6.10 m) and comparisons to swash solution, Eq. (3.10), scaled using $U_{\alpha,(x>0)}$. Top panel: ——, η at L5; ——, η at L8; — —, η from swash solution, Eq. (3.10). Bottom panel: ——, u at L5; ——, u at L8; — —, u from swash solution, Eq. (3.10); ∘, shoreline velocity, u_s, at L5; •, shoreline velocity, u_s, at L8.

flow in the swash zone is driven by a larger initial energy than that predicted by bore collapse theory, which in turn is larger than the energy corresponding to the velocity of the shoreline when it first begins moving the initial energy. The initial shoreline velocity for surging breakers is lower than that predicted by bore collapse theory because the theory assumes that the height of the bore collapses to zero, and the conversion between potential energy of the bore to kinetic energy of the swash is complete, by the time the shoreline starts to move. Due

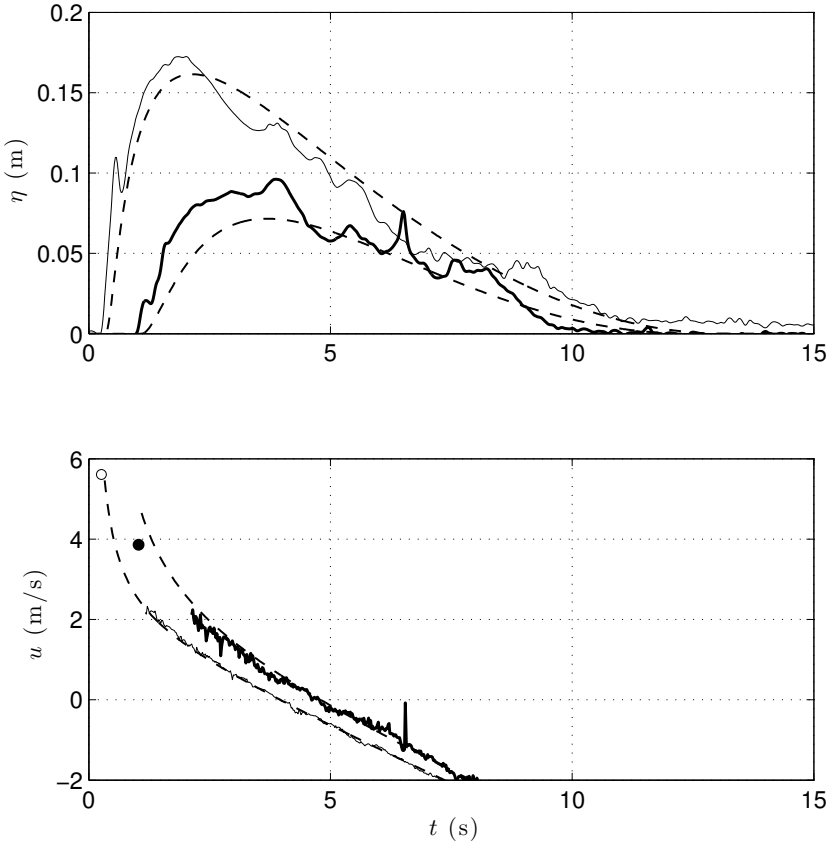

Figure 3.29: Free-surface elevation, η, and near-bed velocity, u, for W8 (PL, H_0 = 0.410 m, ϵ_0 = 0.237) at locations L5 (x = 2.42 m), L8 (x = 6.10 m) and comparisons to swash solution, Eq. (3.10), scaled using $U_{\alpha,(x>0)}$. Top panel: ——, η at L5; ——, η at L8; — —, η from swash solution, Eq. (3.10). Bottom panel: ——, u at L5; ——, u at L8; — —, u from swash solution, Eq. (3.10); ∘, shoreline velocity, u_s, at L5; •, shoreline velocity, u_s, at L8.

to the kinematics of surging breakers (detailed measurements of velocity and acceleration fields near the stillwater shoreline for a surging breaker are shown in Jensen *et al.*, 2003), this transformation is not complete when the shoreline starts to move. The same idea can be also be interpreted as an ambiguity in the location and time of collapse, $(x, t) = (0, 0)$, in the context of the bore collapse theory. The prediction from bore collapse theory, $U_{s,p}$, may be an underestimate for surging breakers because, as measured at location L2, they may not

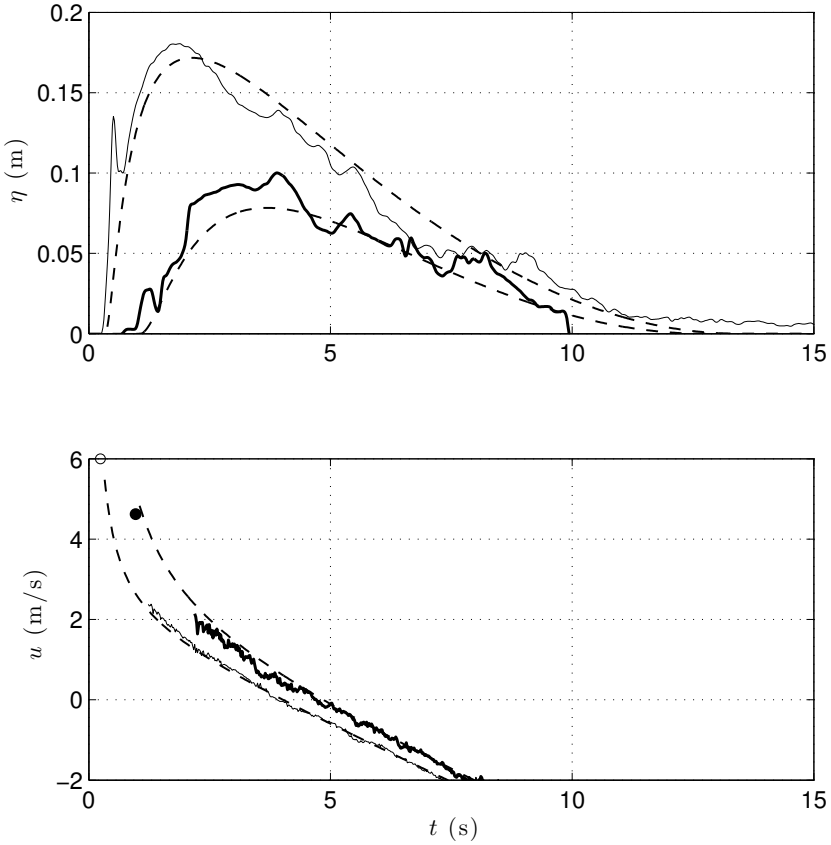

Figure 3.30: Free-surface elevation, η, and near-bed velocity, u, for W10 (PL, H_0 = 0.443 m, ϵ_0 = 0.256) at locations L5 (x = 2.42 m), L8 (x = 6.10 m) and comparisons to swash solution, Eq. (3.10), scaled using $U_{\alpha,(x>0)}$. Top panel: ——, η at L5; ——, η at L8; — —, η from swash solution, Eq. (3.10). Bottom panel: ——, u at L5; ——, u at L8; — —, u from swash solution, Eq. (3.10); ∘, shoreline velocity, u_s, at L5; •, shoreline velocity, u_s, at L8.

be a good approximation to bores of high strength, i.e., their dynamics are not the same as a bore of the same height. The milder wave fronts of waves W5–7 compared to waves W8–10 in Figure 3.14 show evidence for this argument. Or alternatively, for surging breakers, data is required from closer to the stillwater shoreline than location L2 to use bore collapse theory. For plunging breakers, $U_s \approx U_{s,p}$ to within the uncertainty of measurement suggesting that bore collapse theory is valid, but $U_{\alpha,(x>0)} < U_s$. The reason for a swash zone flow that is

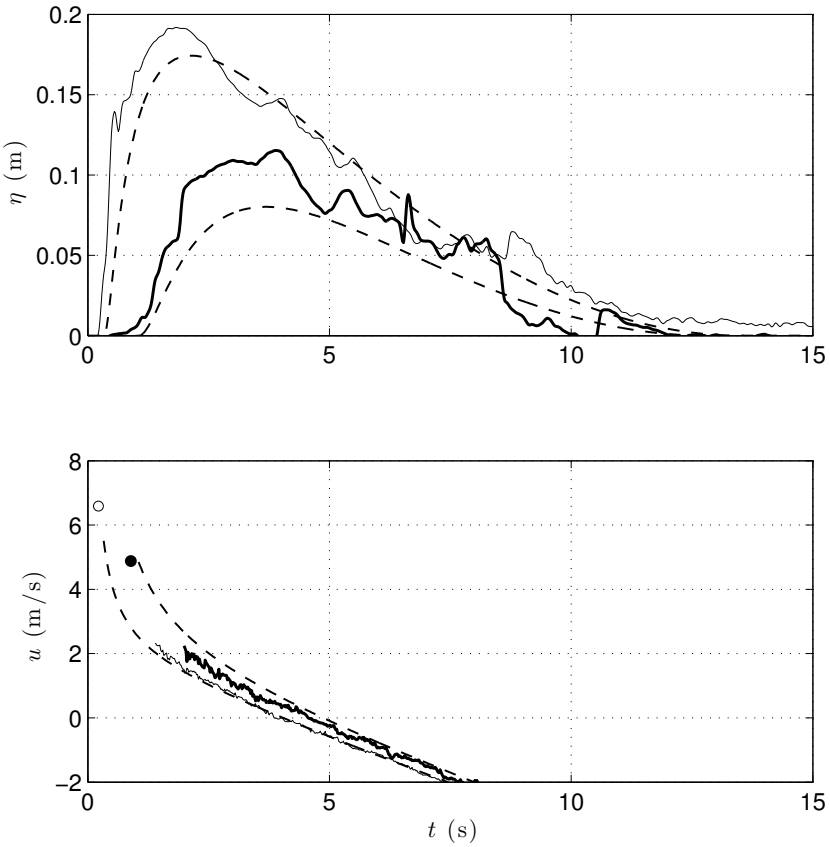

Figure 3.31: Free-surface elevation, η, and near-bed velocity, u, for W10 (PL, H_0 = 0.493 m, ϵ_0 = 0.286) at locations L5 (x = 2.42 m), L8 (x = 6.10 m) and comparisons to swash solution, Eq. (3.10), scaled using $U_{\alpha,(x>0)}$. Top panel: ——, η at L5; ——, η at L8; — —, η from swash solution, Eq. (3.10). Bottom panel: ——, u at L5; ——, u at L8; — —, u from swash solution, Eq. (3.10); ∘, shoreline velocity, u_s, at L5; •, shoreline velocity, u_s, at L8.

driven by a lower initial energy than that corresponding to the initial shoreline velocity is likely the loss of energy from the mean flow to turbulent kinetic energy in the violent breaking process that occurs in plunging breakers. Overall, for the range of breaker types investigated, the swash zone flow is driven by an initial energy that corresponds to a swash initiation shoreline velocity in the range $1.1\sqrt{gh_0} < U_{\alpha,(x>0)} < 1.4\sqrt{gh_0}$.

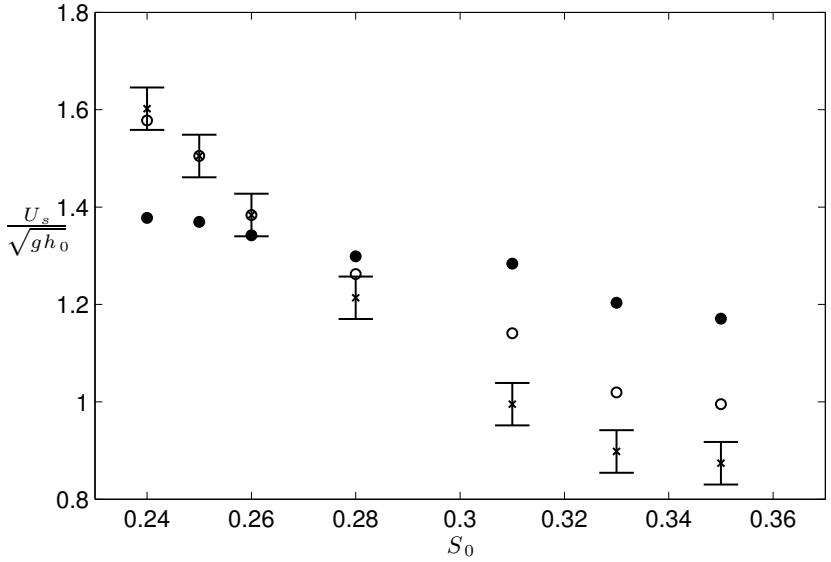

Figure 3.32: Comparisons of different estimates for the swash intitiation shoreline velocity: ∘, $U_{s,p}$, predicted from Whitham's formula for bore collapse, Eq. (3.5)–(3.8); ×, U_s, measured initial shoreline velocity; •, $U_{\alpha,(x>0)}$, constant value of characteristic variable, α, from measurements in the swash.

3.8 Bed shear stress

The time series of the bed shear stress and near-bed velocity in the swash measurement zone for three representative locations (L2, L5 and L8) for three representative waves (W3 - non breaking, W5 - surging breaker, W10 - plunging breaker) are shown in Figures 3.33, 3.34 and 3.35. The sign convention for the bed shear stress is positive when it is directed onshore and negative when it is directed offshore. The fluctuations in the bed shear stress, previously discussed in section 3.4.1, are seen again. The shoreline velocity for each wave for locations onshore of the stillwater shoreline (L5, L8) are also plotted. The free-surface elevation and bed pressure for the same waves at the same locations are shown in Figures 3.36, 3.37 and 3.38. At location L2, none of the waves have reached their breaking point, but at location L5, all waves that break have fully collapsed.

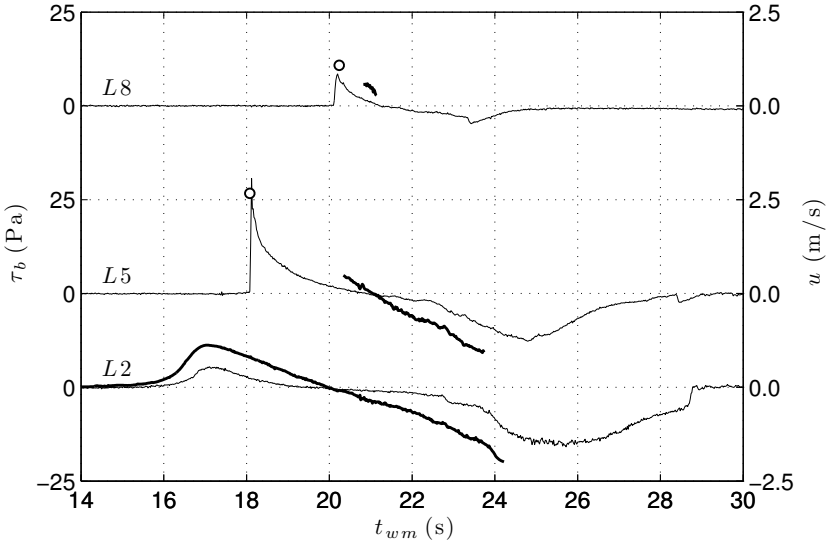

Figure 3.33: Bed shear stress and near-bed velocity for wave W3 (NB, H_0 = 0.173 m, ϵ_0 = 0.100): ——, bed shear stress, τ_b; ——, near-bed velocity, u; ∘, shoreline velocity, u_s. Locations: L2 (x = −1.21 m); L5 (x = 2.42 m); L8 (x = 6.10 m).

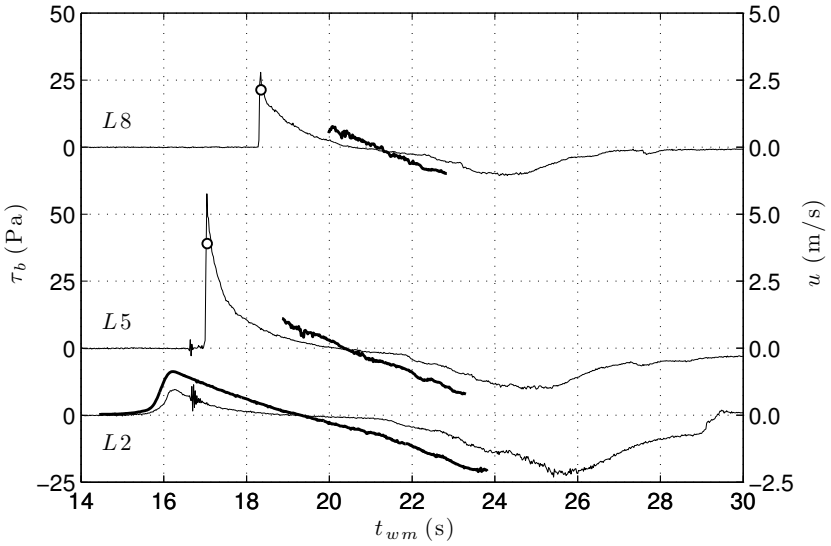

Figure 3.34: Bed shear stress and near-bed velocity for wave W5 (SU, H_0 = 0.261 m, ϵ_0 = 0.151): ——, bed shear stress, τ_b; ——, near-bed velocity, u; ∘, shoreline velocity, u_s. Locations: L2 (x = −1.21 m); L5 (x = 2.42 m); L8 (x = 6.10 m).

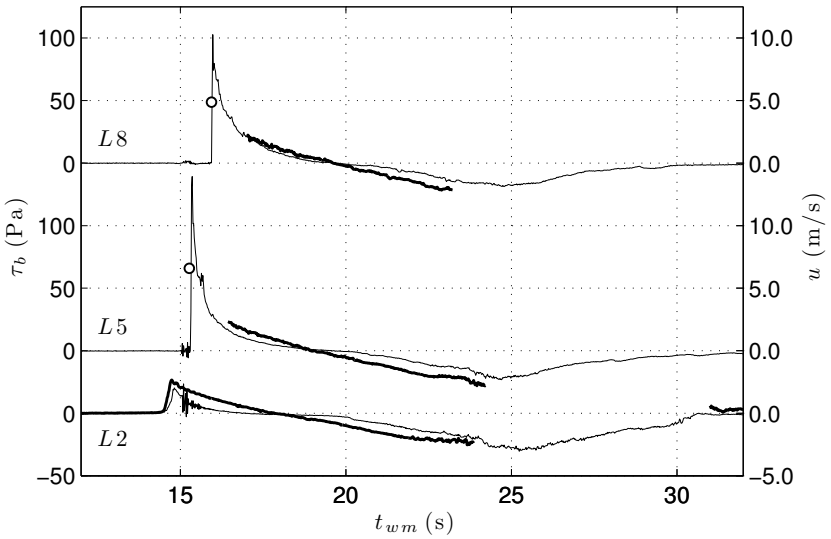

Figure 3.35: Bed shear stress and near-bed velocity for wave W10 (PL, H_0 = 0.493 m, ϵ_0 = 0.286): ——, bed shear stress, τ_b; ——, near-bed velocity, u; ∘, shoreline velocity, u_s. Locations: L2 (x = −1.21 m); L5 (x = 2.42 m); L8 (x = 6.10 m).

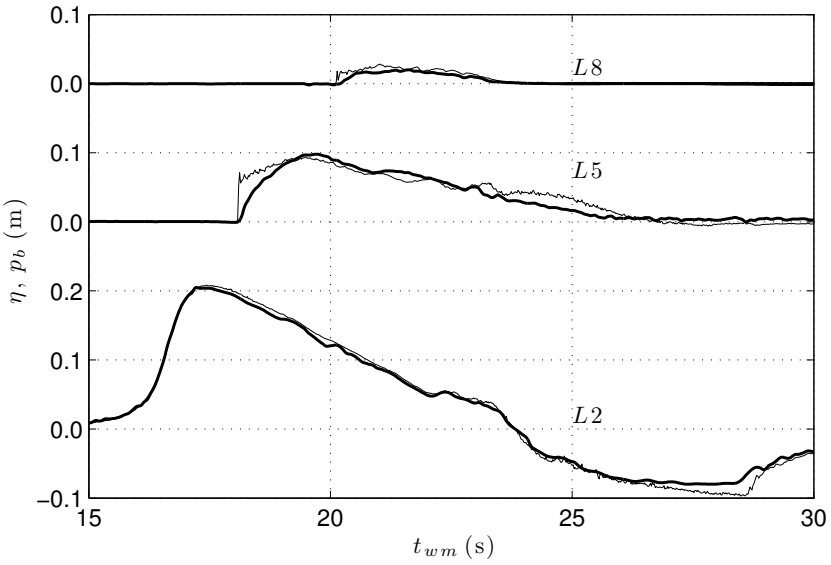

Figure 3.36: Free-surface elevation and bed pressure for wave W3 (NB, H_0 = 0.173 m, ϵ_0 = 0.100): ——, free-surface elevation, η; ——, bed pressure, p_b. Locations: L2 (x = −1.21 m); L5 (x = 2.42 m); L8 (x = 6.10 m).

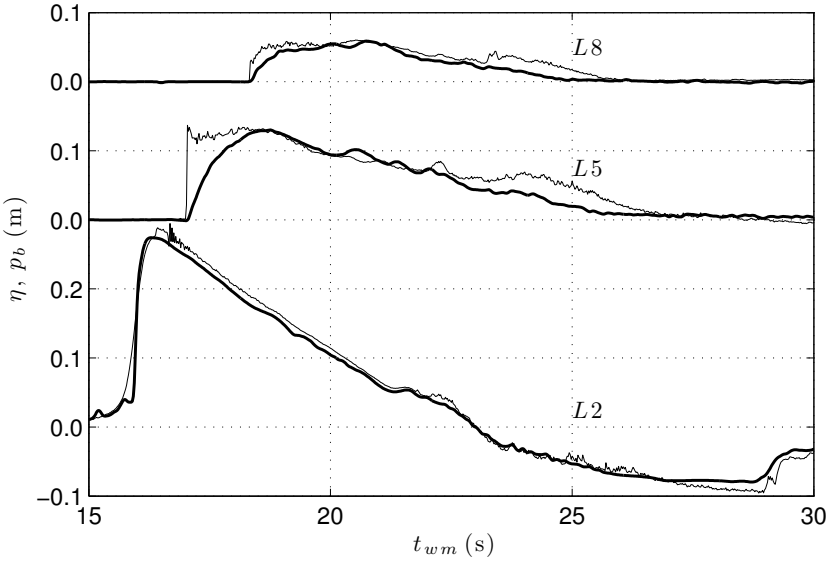

Figure 3.37: Free-surface elevation and bed pressure for wave W5 (SU, H_0 = 0.261 m, ϵ_0 = 0.151): ——, free-surface elevation, η; ——, bed pressure, p_b. Locations: L2 (x = −1.21 m); L5 (x = 2.42 m); L8 (x = 6.10 m).

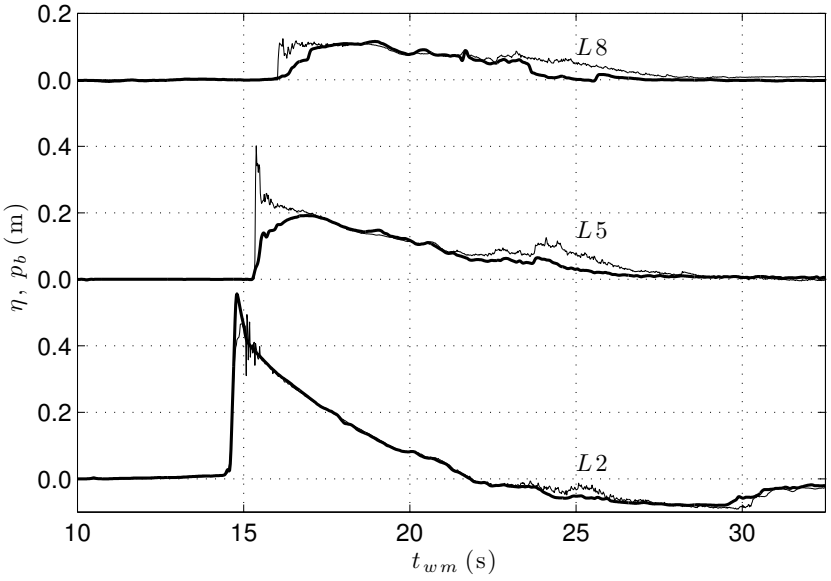

Figure 3.38: Free-surface elevation and bed pressure for wave W10 (PL, H_0 = 0.493 m, ϵ_0 = 0.286): ——, free-surface elevation, η; ——, bed pressure, p_b. Locations: L2 (x = −1.21 m); L5 (x = 2.42 m); L8 (x = 6.10 m).

For the swash cycle at a location onshore of wave collapse, the highest bed shear stress occurs when the swash tip first arrives during uprush, where the water particle velocity must equal the shoreline velocity (Figures 3.33–3.35). In the same region, the bed pressure rises faster than the free-surface (Figures 3.36–3.38) implying large vertical accelerations, although quantitative comparisons between the bed pressure and the free-surface elevation at the swash tip are not attempted because the free-surface is somewhat ill-defined at the swash tip due to a large amount of entrained air that rises to the surface. Furthermore, the spatial resolution of the free-surface elevation measurement is coarser than the bed pressure measurement due to the differences in sensor sizes and principles of operation. The high values of bed shear stress at the swash tip are thought to be due to the continually developing boundary layer and bore-generated turbulence from the contiuous breaking at the leading edge of the swash. Measurements of the velocity near the swash tip have so far proven difficult due to the presence of air bubbles, highly unsteady nature of the swash tip and its fast translational velocity (*e.g.* O'Donoghue *et al.*, 2010; Kikkert *et al.*, 2012), but Pedersen *et al.* (2013) have measured and computed velocity profiles close to a laminar swash tip in a small-scale laboratory study. Baldock *et al.* (2014) have also studied a laminar swash tip by using a highly viscous fluid. They showed that there is flow convergence at the swash tip as the fluid near the surface travels faster than the fluid near the bed and impinges onto the bed creating high strain rates that lead to high values of bed shear stress. The impingement of the fluid onto the bed may also explain why the bed pressure is measured to be higher than the hydrostatic pressure. Sumer *et al.* (2011) showed similar trends for the bed shear stress in the swash of a plunging solitary wave. They used a hot-film sensor that was 0.5 mm x 0.5 mm. With its small size, they were also

able to capture some of the turbulent fluctuations of the bed shear stress. In the swash zone, they showed that the instantaneous bed shear stress at the swash tip could be twice the mean bed shear stress, which they obtained through ensemble averaging. Behind the swash tip, the bed shear stress decays rapidly and the pressure returns to hydrostatic. The low values of the bed shear stress are in phase with the velocity due to absence of strong pressure gradients, unlike boundary layers under waves in water of constant depth where the bed shear stress leads the velocity (*e.g.*, Nielsen, 1992; Liu *et al.*, 2007). The flow in this part of the swash cycle, the mid-swash duration, is a gravity-driven flow that follows the evolution predicted by the swash solution, Eq. (3.10).

Towards the end of the downrush, the bed shear stress values are also high (and directed offshore). The flow velocities during this period are also difficult to measure due to the very shallow depths, but the velocity data before the flow depth becomes too shallow show that the flow is accelerated down the slope by gravity and the magnitude of the bed shear stress increases to slow down the flow while the flow depth continues to reduce. The bed shear stress reaches a peak negative value after which it reduces to zero as the water runs out. The velocity must also reduce to zero as the water runs out and thus at some intermediate stage, the offshore-directedvelocity must reach a maximum magnitude when there is a temporary balance between the gravitational acceleration and the bed shear stress (the streamwise velocity gradient and the streamwise pressure gradient are not expected to be of leading order importance in the momentum balance). During this period, the bed pressure measurements are also higher than the free-surface elevation measurements, implying the existence of vertical accelerations. Though the flow is very shallow, the free-surface must be rising relative to the bed in the flow direction, i.e., $\partial\eta/\partial x < 0$, because the

water depth further onshore of the measurement location reduces to zero earlier than the water depth further offshore of the measurement location. Thus, locally, there may exist some streamline curvature that would explain the non-hydrostatic pressure measurements. At location L5, around $t \approx 22$ s, there is a sudden increase in the magnitude of the bed shear stress in the negative direction for all waves plotted in Figures 3.33–3.35. A similar feature is observed for other locations. Sumer *et al.* (2011) also identified this feature in their results and using the ensemble averaging procedure to decompose the bed shear stress into mean and fluctuating components, concluded that this point was where the fluctuating component of the bed shear stress was large. Thus, they indicated that this must be the time when the downrush flow boundary layer becomes turbulent generating fluctuations in the bed shear stress and causing a sudden increase in its mean magnitude.

The flow behaviour near the swash tip and towards the end of downrush is not very well understood, but these are the regions in the swash cycle when the bed shear stress is most significant. However, in the mid-swash duration, the flow is well-understood and to attempt to parameterize the bed shear stress in this part of the flow, a local, time-varying friction coefficient and Reynolds number can be calculated using the near-bed velocity, free-surface elevation and the bed shear stress signals. The friction coefficient is defined as

$$C_f' = \frac{\tau_b}{\frac{1}{2}\rho u^2}, \tag{3.22}$$

where the prime refers to the fact that it is a local, time-varying quantity. The Reynolds number is calculated as

$$Re' = \frac{u\eta}{\nu}, \tag{3.23}$$

where the local water depth, η, is chosen as the relevant lengthscale and the prime once again refers to the fact that it is a local, time-varying quantity. These quantities are plotted in Figures 3.39, 3.40 and 3.41 for location L5 for waves W3, W5 and W10, respectively. It can be seen that the friction coefficient is not well-defined around the time when the flow changes from uprush to downrush and the velocity goes to zero. Furthermore, values for C_f' and Re' are not available near the swash tip and near the end of downrush where velocity data are unavailable. During downrush, the data show that for different incident waves, the values of Re' fall within the range $0.5 \times 10^5 < Re' < 10^5$ with a corresponding range of $0.005 < C_f' < 0.01$. Barnes *et al.* (2009) investigated the variation in C_f' with Re' and location within the swash using depth averaged velocities obtained from a NSWE hydrodynamic model. They found that during uprush, C_f' tends to decrease with increasing Re', which is the trend for steady flows, but at locations further up the slope in the swash, the same Re' gives a lower C_f' than at locations further down the slope. During downrush, C_f' initially decreases with increasing Re' and then the trend is reversed during the later stages of downrush. They also compared their data to the Colebrook-White formula for steady, turbulent, open-channel flow and found that C_f' was under-predicted during uprush and over-predicted during downrush. These results have been corroborated by the results of O'Donoghue *et al.* (2010) and Kikkert *et al.* (2012), who used a log-law fitting to estimate the bed shear stress from velocity data obtained from PIV measurements in the swash. The same conclusions can be drawn from the current data, with the trend of decreasing C_f' with increasing Re' during uprush and a mixed dependence of C_f' on Re' during downrush vis-

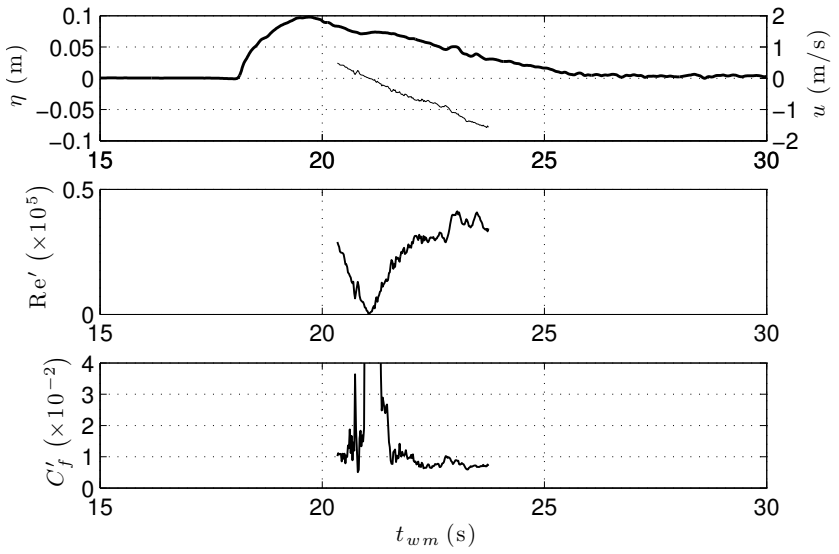

Figure 3.39: Top panel: ——, free-surface elevation, η; ——, near-bed velocity, u. Middle panel: local, time-varying Reynolds number, Re'. Bottom panel: local, time-varying friction coefficient, C'_f. Location L5 (x = 2.42 m) for wave W3 (NB, H_0 = 0.173 m, ϵ_0 = 0.100).

ible in Figures 3.39–3.41. Thus, for the data in this study, C'_f is not a universal function of Re', likely because the swash flow is unsteady.

From the point of view of the flow dynamics, it is more important to parameterize the maximum magnitudes of bed shear stresses since these occur when bed friction significantly alters the flow: at the swash tip and at the end of the downrush. The maximum magnitude of the bed shear stress during uprush and downrush at a given location are denoted as $\tau_{b,u}$ and $\tau_{b,d}$, respectively. The sign convention is retained so that $\tau_{b,d}$ is a negative quantity referring to the fact that the downrush stress is offshore-directed. These quantities are shown in figure 3.42. For the breaking waves, W5 and W10, there is an $O(6)$-fold and $O(7)$-fold increase in the maximum uprush bed shear stress across the collapse points, respectively. Sumer *et al.* (2011) observed similar increase across breaking for their

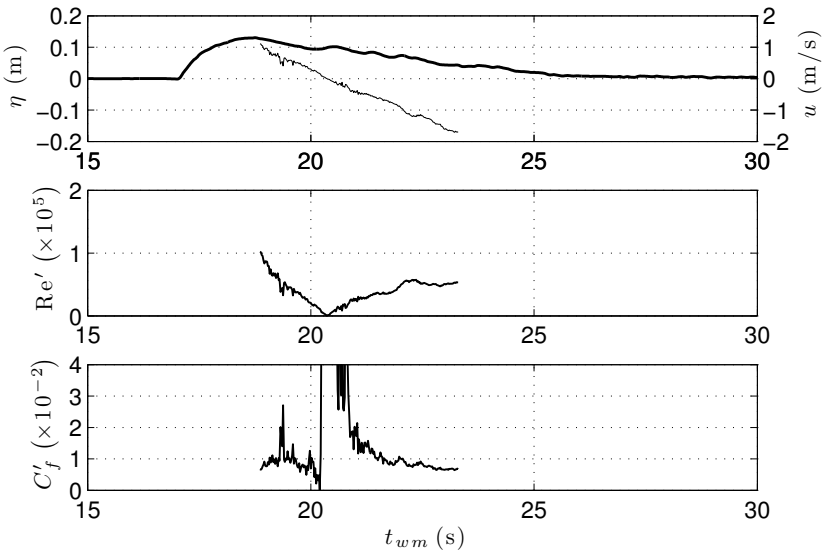

Figure 3.40: Top panel: ——, free-surface elevation, η; ——, near-bed velocity, u. Middle panel: local, time-varying Reynolds number, Re'. Bottom panel: local, time-varying friction coefficient, C'_f. Location L5 (x = 2.42 m) for wave W5 (SU, H_0 = 0.261 m, ϵ_0 = 0.151).

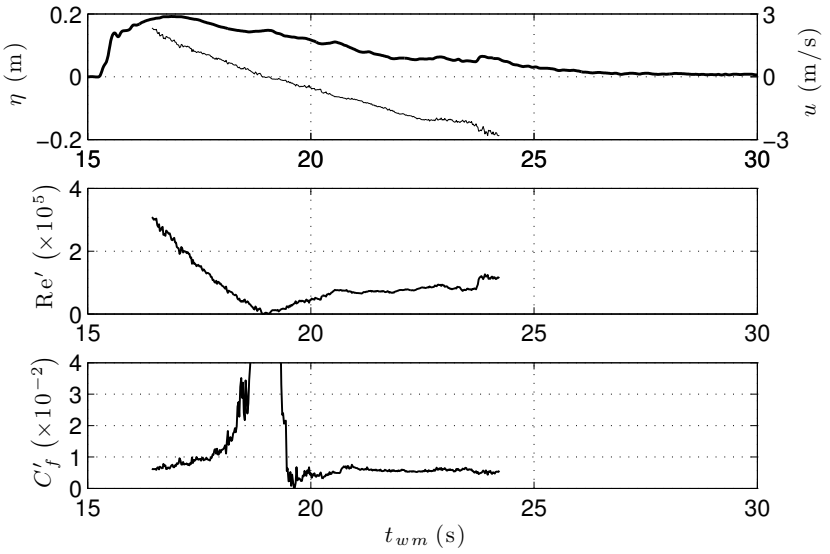

Figure 3.41: Top panel: ——, free-surface elevation, η; ——, near-bed velocity, u. Middle panel: local, time-varying Reynolds number, Re'. Bottom panel: local, time-varying friction coefficient, C'_f. Location L5 (x = 2.42 m) for wave W10 (PL, H_0 = 0.493 m, ϵ_0 = 0.286).

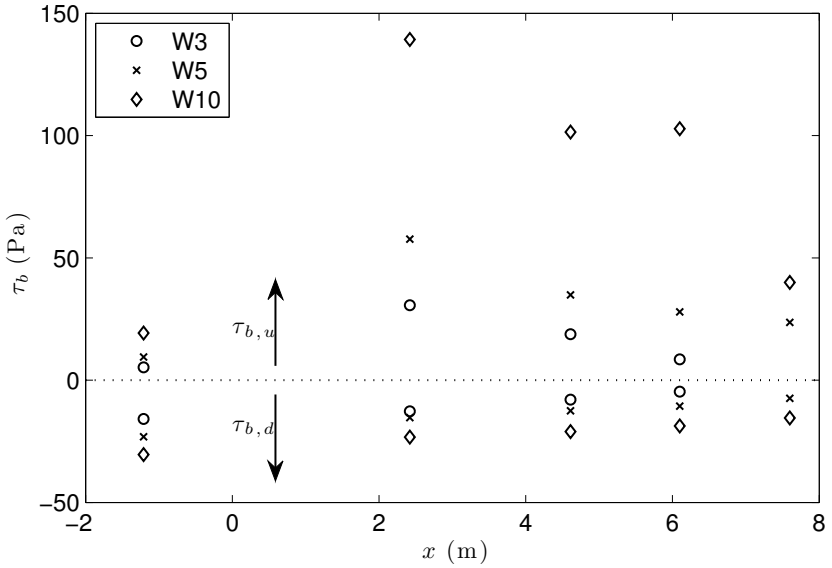

Figure 3.42: Maximum magnitudes of the bed shear stress for W3 (NB, H_0 = 0.173 m, ϵ_0 = 0.100), W5 (SU, H_0 = 0.261 m, ϵ_0 = 0.151) and W10 (PL, H_0 = 0.493 m, ϵ_0 = 0.286) as a function of distance from the stillwater shoreline, x.

plunging wave case. This increase is attributed to the effects of breaking and collapse, which produce high-velocity, turbulent flow at the swash tip. However, the non-breaking wave W3 also shows an $O(6)$-fold increase in the maximum uprush bed shear stress across the stillwater shoreline indicating that the swash tip generates a much higher bed shear stress than wave-induced boundary layer even when there is no breaking. There is also an asymmetry in the swash, with larger values of $\tau_{b,u}$ than $\tau_{b,d}$, which has been previously noted by Barnes *et al.* (2009) and others. This asymmetry is less pronounced further up the slope.

To compare the values of the maximum magnitudes of the bed shear stress in the uprush and downrush for different breaking waves, the maximum magnitudes of the uprush and downrush bed shear stress need to be made dimensionless. The swash initiation shoreline velocity has been identified as the largest and defining velocity scale of the swash in previous sections and thus it is the

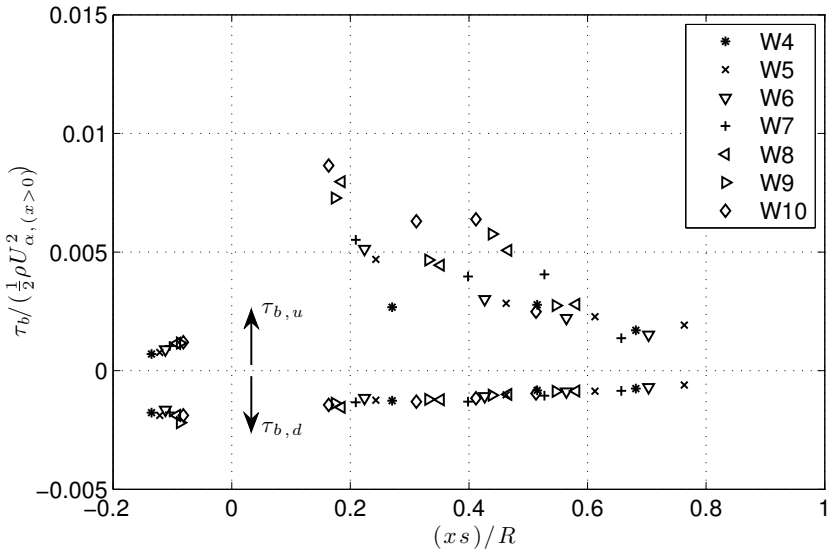

Figure 3.43: Dimensionless maximum magnitudes of the bed shear stress for all breaking waves, W4–10, as function of dimensionless distance from the stillwater shoreline.

appropriate velocity scale to make the maximum magnitudes of the bed shear stress dimensionless. Thus, a dimensionless measure of the maximum magnitudes of the uprush and downrush shear stress at a given location can be defined as

$$\frac{\tau_{b,u}}{\frac{1}{2}\rho U^2_{\alpha,(x>0)}}, \tag{3.24a}$$

$$\frac{\tau_{b,d}}{\frac{1}{2}\rho U^2_{\alpha,(x>0)}}, \tag{3.24b}$$

where the estimate of the swash initiation shoreline velocity obtained from measurements in the swash zone, $U_{\alpha,(x>0)}$, is used above other measurements and estimates of the same quantitiy because it is derived from the data. Figure 3.43 shows that the dimensionless maximum magnitudes of bed shear stress for different incident waves collapse under this normalization giving further confidence of the importance of this velocity scale in the swash. The maxi-

mum magnitude for the uprush dimensionless maximum bed shear stress is $\tau_b/(0.5\rho U^2_{\alpha,(x>0)}) \approx 0.01$, which occurs just after the collapse region. The maximum magnitude for the downrush dimensionless maximum bed shear stress is $\tau_b/(0.5\rho U^2_{\alpha,(x>0)}) \approx 0.002$, which occurs just before the hydraulic jump. The asymmetry of the bed shear stress between the uprush and downrush is also evident in Figure 3.43.

If different velocity scales are chosen for the uprush and downrush, so that $\tau_{b,u}$ is made dimensionless by the measured swash initiation shoreline velocity, U_s, and $\tau_{b,d}$ is made dimensionless by $U_{d,L2}$, the maximum offshore-directed velocity measured by the ADV at location L2 before the hydraulic jump occurs, the dimensionless maximum bed shear stress for uprush and downrush have similar magnitudes and similar decreasing trend in the swash for different breaking waves. Figure 3.44 plots these results. Now, the maximum magnitude for the uprush and downrush dimensionless bed shear stress is $\tau_{b,u}/(0.5\rho U_s^2) \approx \tau_{b,d}/(0.5\rho U^2_{d,L2}) \approx 0.01$.

3.9 Integral model of swash tip during uprush

The run-up measurements can be used to calculate a hypothetical initial shoreline velocity of a frictionless swash that follows the swash solution, Eq. (3.9)–(3.10) but reaches the same run-up as the measured shoreline. This hypothetical initial shoreline velocity is given by $\sqrt{2gR}$. The discrepancy between this velocity and the measured swash initiation shoreline velocity gives the scale of the energy dissipation in the swash tip. The implied assumptions are that the energy dissipation is dominantly from friction at the swash tip and the work

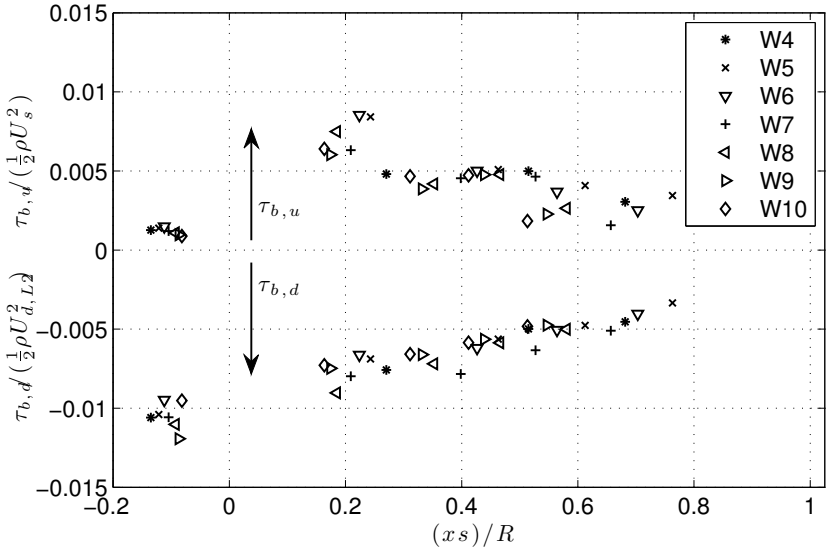

Figure 3.44: Dimensionless maximum magnitudes of the bed shear stress for all breaking waves, W4–10, as function of dimensionless distance from the stillwater shoreline. Maximum bed shear stress in uprush made dimensionless by U_s, and maximum bed shear stress in downrush made dimensionless by $U_{d,L2}$.

done by pressure on the swash tip from the frictionless flow behind the swash tip is negligible. Figure 3.45 shows the comparisons between frictionless shoreline velocity and the measured shoreline velocity for a surging breaker, W5, and a plunging breaker, W10. It can be seen that the plunging breaker achieves a shoreline velocity of roughly $1.4\sqrt{2gR}$. Since energy is proportional to velocity squared, this shows that only just over 50% of the initial energy of the shoreline is converted to the potential energy of the run-up and the rest is lost to dissipation. For the surging breaker, the frictionless shoreline velocity gives a good predictor of the measured shoreline velocity and almost 90% of the initial energy is converted to potential energy of the run-up.

Svendsen (2006) provided a treatment of friction at the leading edge of the swash by adding a term to model friction (of the form fu^2/h) to the friction-

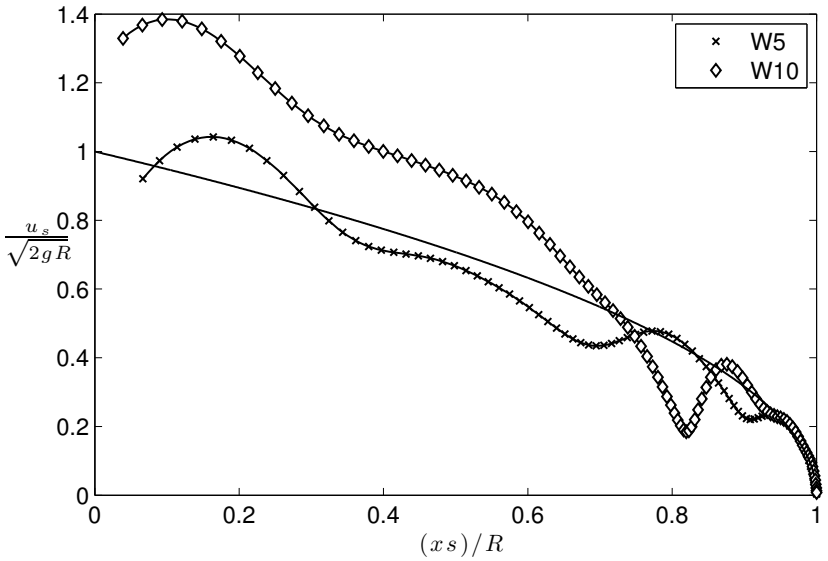

Figure 3.45: Comparison of shoreline velocity data to frictionless shoreline velocity for Waves W5 (SU, H_0 = 0.261 m, ϵ_0 = 0.151) and W10 (PL, H_0 = 0.493 m, ϵ_0 = 0.286): *symbols*, data; ——, frictionless shoreline motion, Eq. (3.9).

less dynamics described by Eq. (3.9), while also neglecting the influence of the flow behind the swash tip. However, the applicability of a frictional term using a depth-averaged velocity as the water depth goes to zero at the leading edge of the swash tip is questionable as recently discussed by Antuono *et al.* (2012). Therefore, to give due consideration to the all the forces on the swash tip, including the force of pressure from behind the swash tip from the frictionless flow, the 'Pohlhausen method', originally employed by Whitham (1955) to model the tip of a dam-break flow on a horizontal bed, is extended to the swash tip during uprush. The applicability of this integral method arises from the fact that the swash tip region is governed by a different dynamical balance than the frictionless flow behind the swash tip, analogous to a boundary layer in flow over a flat plate. As a first approximation, the velocity in the swash tip is assumed to be uniform. In this integral treatment of the swash tip, the bed shear stress is

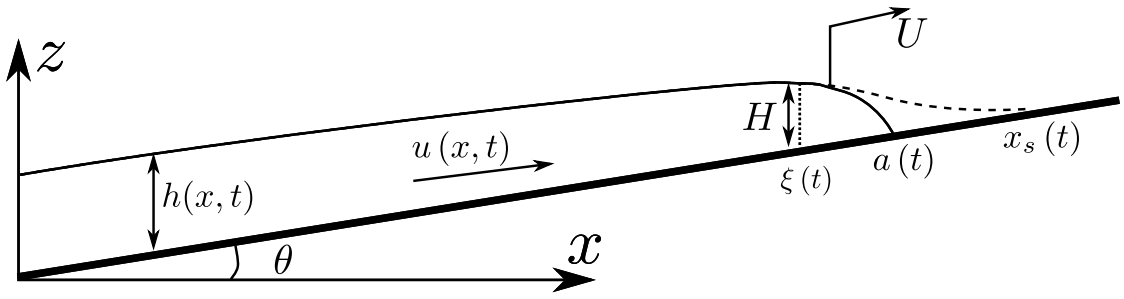

Figure 3.46: Definition sketch for analysis of the motion of the swash tip during uprush. $h(x,t)$ and $u(x,t)$ are the frictionless flow variable known from the swash solution, Eq. 3.10. $a(t)$ is the location of the moving shoreline, $\xi(t)$ is the interface between the swash tip region and the frictionless flow.

constant and modelled using the form $K\rho U^2$, where U is the bulk velocity of the swash tip, and the difficulty in modelling the friction as the water depth goes to zero at the leading edge is avoided. The effects of surface tension at the leading edge of the swash tip are neglected.

Figure 3.46 shows the swash tip during uprush. The frictionless shoreline is approached with free-surface tangential to the bed, but the effects of friction give the swash tip a 'blunt nose' and consequently, the shoreline position, $a(t)$, is behind the frictionless shoreline position, $x_s(t)$. $\xi(t)$ is the interface between the friction-affected swash tip and the frictionless flow, and thus $(a-\xi)$ is the extent of the swash tip. The momentum balance for the swash tip can be written as

$$\frac{dP}{dt} = \rho UH\left(U - \frac{d\xi}{dt}\right) + \frac{1}{2}\rho gH^2 - \rho KU^2(a-\xi) - Mgs, \tag{3.25}$$

where $P(t)$ is the momentum of the swash tip region, $M(t)$ is its mass, $U(t)$ is its velocity, and $H(t)$ is the water depth at the interface, $\xi(t)$. ρ is the fluid density and K is a dimensionless constant from the parameterization of the bed shear stress, $K = \tau_b/\rho U^2$. The first term on the right hand side of Eq. (3.25) accounts

for the flux of momentum across the interface between the swash tip and the frictionless flow, the second term accounts for the force of the frictionless flow on the swash tip (the pressure in the frictionless flow is hydrostatic), the third term models the frictional force, and the last term is due to the gravitational force. The position of the interface, $\xi(t)$, is an unknown to be solved.

The momentum of the swash tip region can be written as $P(t) = M(t)\,U(t)$, since the flow motion in that region is averaged. The mass of the swash tip is the same as the mass of the frictionless flow, Eq. (3.10), between $x = \xi(t)$ and $x = x_s(t)$. Thus,

$$\begin{aligned} M(t) &= \int_{\xi}^{x_s} \rho h dx, \\ &= \frac{\rho t}{8g}\left(U_s - gst - U\right)^3. \end{aligned} \tag{3.26}$$

The balance of mass in the swash tip is given by:

$$\frac{dM}{dt} = \rho H\left(U - \frac{d\xi}{dt}\right). \tag{3.27}$$

Now, substituting $dP/dt = M(dU/dt) + U(dM/dt)$ and Eq. (3.27) into Eq. (3.25), gives the governing equation for the swash tip,

$$M\frac{dU}{dt} = \frac{1}{2}\rho g H^2 - \rho K U^2 (a - \xi) - Mgs. \tag{3.28}$$

Using Eq. (3.10), the depth-averaged velocity and the water depth at the interface, $x = \xi(t)$, can be found in terms of U to be

$$\xi = \frac{3}{2}Ut - \frac{1}{2}U_s t + gst^2, \tag{3.29}$$

$$H = \frac{1}{4g}\left(U_s - U - gst\right)^2, \tag{3.30}$$

and these expressions for $\xi(U)$ and $H(U)$ are substituted into the momentum equation, which is re-expressed in terms of a, $da/dt \equiv U$, and $d^2a/dt^2 \equiv dU/dt$ to give

$$4t\left(U_s - gst - \frac{da}{dt}\right)^3\left(\frac{d^2a}{dt^2} + gs\right) = \left(U_s - gst - \frac{da}{dt}\right)^4 - 32Kg\left(\frac{da}{dt}\right)^2 \times\left(a - \frac{3}{2}\frac{da}{dt}t + \frac{1}{2}U_s t - gst^2\right). \tag{3.31}$$

When friction is neglected, i.e., $K = 0$, the frictionless shoreline motion, Eq. (3.9), can be recovered from the above governing equation. To make the problem more tractable in the case where friction is not neglected, i.e., $K \neq 0$, the dimensionless position of the swash tip, α, and the dimensionless time, τ, are introduced as follows:

$$\alpha = \frac{Kg}{U_s^2}\left(U_s t - \frac{1}{2}gst^2 - a\right),\ \tau = \frac{Kg}{U_s}t, \tag{3.32}$$

where α is proportional to how far the front lags behind the frictionless front, x_s. The form of α and τ are similar to those in Whitham (1955), but modified to suit the swash uprush. In terms of the dimensionless variables, $U_s\left(d\alpha/d\tau\right) = U_s - gst - da/dt$ and $d^2\alpha/d\tau^2 = -s/K - (1/Kg)\,d^2a/dt^2$. The dimensionless momentum equation can be derived from Eq. (3.31) as

$$4\tau\dot{\alpha}^3\ddot{\alpha} + \dot{\alpha}^4 = 16\left[1 - \dot{\alpha} - \left(\frac{s}{K}\right)\tau\right]^2 (3\tau\dot{\alpha} - 2\alpha), \tag{3.33}$$

where the dot notation represents differentiation with respect to τ, so that $\dot{\alpha} \equiv d\alpha/d\tau$ and $\ddot{\alpha} \equiv d^2\alpha/d\tau^2$.

Following Whitham (1955), the parameters $p = \dot{\alpha}$ and $\tau = f'(p)$ are introduced to transform the dimensionless momentum equation so that $\dot{\alpha}$ becomes the independent variable and τ becomes the dependent variable. Note, the prime notation denotes differentiation of f. Under this transformation, $\alpha = \int \dot{\alpha} d\tau$, which with $\alpha(0) = 0$, leads to $\alpha = pf'(p) - f(p)$ and $\ddot{\alpha} = d\dot{\alpha}/d\tau = 1/f''(p)$. The momentum equation, Eq. (3.33), becomes

$$4f'p^3 + p^4 f'' = 16f''\left[1 - p - \left(\frac{s}{K}\right)f'\right]^2 (f'p + 2f). \tag{3.34}$$

At small time, near the initial shoreline position, $p = \dot{\alpha}$ is small and the function $f(p)$ can be represented as a Taylor series expansion about $p = 0$ to give

$$f(p) = c_0 f(0) + c_1 f'(0)\, p + c_2 f''(0)\, p^2 + c_3 f^{(3)}(0)\, p^3 + c_4 f^{(4)}(0)\, p^4 + \ldots . \tag{3.35}$$

From the initial conditions, at $\tau = 0$, $\alpha = \dot{\alpha} = 0$ and therefore $f(0) = f'(0) = 0$. Furthermore, since $\ddot{\alpha} \to \infty$ at $\tau = \dot{\alpha} = 0$, $f''(0) = 0$ and $f^{(3)}(0) = 0$. Thus, the first term in Taylor series expansion of $f(p)$ is proportional to p^4. The coefficient for the term proportional to p^4 can be found by substituting the Taylor series expansion, Eq. (3.35), into Eq. (3.34). Thus, an explicit solution for the shoreline motion at small time that includes the leading order effect of friction is given by

$$f'(p) = \frac{7}{72}p^3 + O\left(p^4\right), \tag{3.36}$$

which can be re-expressed in the original variables to give

$$\frac{da}{dt} = U_s - gst - \left(\frac{72}{7}U_s^2 Kgt\right)^{1/3}, \tag{3.37}$$

where the last term represents the correction due to friction. Note, Whitham's analytical solution to an equation similar to Eq. (3.34) was possible because the terms in the square brackets were reduced to $(2-p)$, which allowed further approximations to the governing equation, but the presence of an additional term proportional to f' in Eq. (3.34) does not allow the same analytical approach to be used. The Taylor series approximate solution for shoreline velocity can be integrated with the initial condition $a(0) = 0$ to give the shoreline position as

$$a(t) = U_s t - \frac{1}{2}gst^2 - \frac{3}{4}t^{4/3}\left(\frac{72}{7}U_s^2 Kg\right)^{1/3}. \tag{3.38}$$

The Taylor series expansion requires that $p = \dot{\alpha}$ is small, but the theory is expected to break down anyway when the position of the interface, ξ, excessively separates from the leading tip, $a(t)$, and moves back to the origin, i.e., $\xi = 0$, because then the swash tip region covers the entire swash. From Eq. (3.29), when $\xi = 0$, $\dot{\alpha} = (2/3)\left[1 - (gst/U_s)\right]$ and $da/dt = (1/3)(U_s - gst)$, so that the shoreline velocity is $(1/3)$ of the frictionless shoreline velocity, u_s. Since we only consider the uprush, $gst/U_s < 1$ and therefore $\dot{\alpha} < 2/3$ while $\xi > 0$. The Taylor series solution ignores terms of $O\left(p^4\right)$ and higher powers of p, and so we can calculate that the largest error in $\dot{\alpha}$ due to truncation of the series, before the theory breaks down, is less than $(2/3)^4 \approx 20\%$.

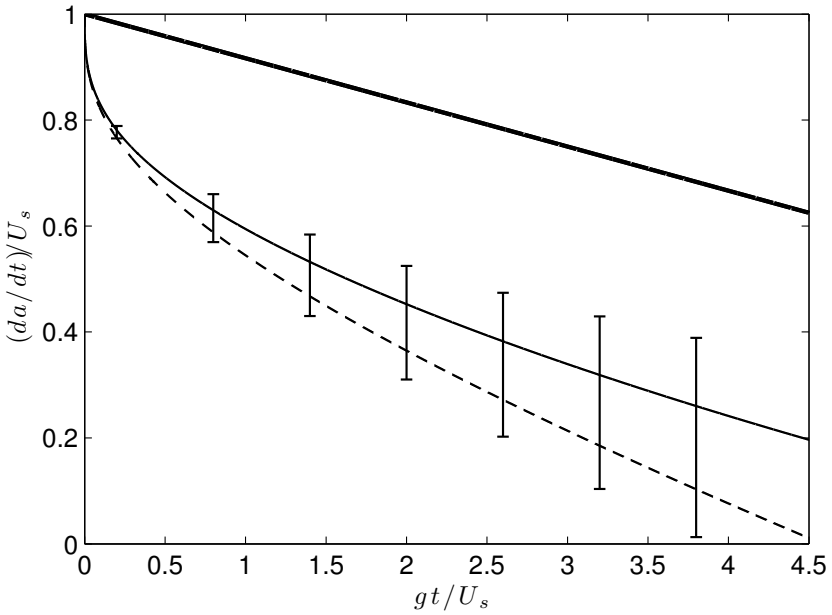

Figure 3.47: Dimensionless shoreline velocity. ——, frictionless solution, Eq. (3.9) with $s = 1/12$; ——, numerical solution, Eq. (3.33), with $s = 1/12$ and $K = 0.005$; — —, Taylor series approximate solution, Eq. (3.37), with $s = 1/12$ and $K = 0.005$. Vertical bars show the bounds for the numerical solution, Eq. (3.33), for $0.0025 < K < 0.01$.

The Taylor series solution to shoreline velocity, Eq. (3.37), is used as an initial condition to numerically solve Eq. (3.33) using a fourth-order Runge-Kutta algorithm. The full numeical solution, the Taylor series solution and the frictionless shoreline velocity are plotted together in Figure 3.47 for the parameters $s = 1/12$ and $K = 0.005$. The time at which $\xi = 0$ for these parameters is $gt/U_s = 4.31$ and it can be seen in Figure 3.47 that the deceleration approaches the frictionless deceleration due to gravity as dimensionless time approaches $gt/U_s = 4.31$.

From Figures 3.43–3.44, the value of K in the initial stages of the swash is $K = 0.005$ for a range of breaking solitary waves, but Figure 3.47 also shows the sensitive of the theory to the value of K: vertical bars show the numerical

solution for values of $K = 0.0025$ and $K = 0.01$. Changing the value of K by a factor of two does not drastically alter the results. Thus, using $s = 1/12$ and $K = 0.005$ the shoreline velocity and position of the plungin breakers (W7–10) are compared to the results of the above theory.

The formulation of the theory assumes that the frictionless part of the flow follows the swash solution, Eq. (3.10), from $t = 0$ onwards, but as Peregrine and Williams (2001) pointed out, the swash solution is not valid near the origin of $(x, t) = (0, 0)$, where it is singular and shows large vertical accelerations that are neglected in the governing equations. Therefore, the results of the theory are only applicable after a small time, say $t > t_0$, when the flow of breaking waves follows the swash solution (see sketches in Figure 3.48). Therefore, a constant is added to the shoreline velocity, given in dimensionless form by

$$\frac{(\triangle U_s)}{U_s} = \left(\frac{72}{7}\frac{Kgt_0}{U_s}\right)^{1/3}, \tag{3.39}$$

to compensate for the initial deceleration due to the frictional term during $0 \leq t \leq t_0$. Figure 3.49 plots the data of shoreline velocity of W7–10 made dimensionless by their measured swash initiation shoreline velocity, U_s. Figure 3.49 also plots the numerical solution of Eq. (3.33) and the Taylor series approximate solution, Eq. (3.37), with $s = 1/12$ and $K = 0.005$ to match the experiments. Both the numerical solution and the Taylor series approximate solution have been vertically shifted up by a constant calculated using Eq. (3.39) with $gt_0/U_s = 0.3$ to compare the applicable portion of the theoretical solutions to the data. The value $gt_0/U_s = 0.3$ was chosen as the time after which the shoreline velocity in the experiments starts decelerating and the flow could be assumed to follow the swash solution. It can be seen that the theoretical solutions match the data

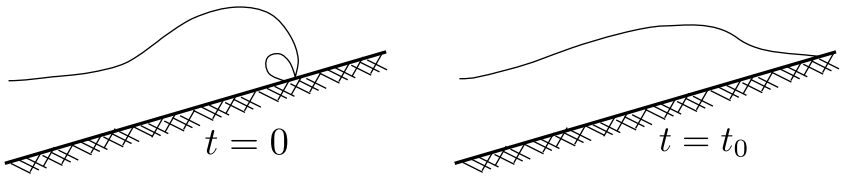

Figure 3.48: Sketches of plunging breakers near the stillwater shoreline. *Left*: $t = 0$ is the time the overturning jet hits the land onshore of the stillwater shoreline; *right*: the flow away from the shoreline starts to follow the swash solution, Eq. (3.10), after some time, $t = t_0$.

remarkably well in the period $0.3 \leq gt/U_s \leq 3$, with the Taylor series approximate solution showing a slightly better match to the data thereafter suggesting that the shoreline in the experiments decelerates faster than predicted by the theory. For $s = 1/12$ and $K = 0.005$, the time at which $\xi = 0$ is $gt/U_s = 4.31$, but the solutions are shown nonetheless for larger times. In the time range, $4 \leq gt/U_s \leq 6$, the experimental data shows an accelerating behaviour, which has been linked to a 'mini-collapse' caused by a build up of fluid behind the shoreline as it comes to a halt (see Yeh *et al.*, 1989; Zhang and Liu, 2008) and this feature is not captured by the theory, of course.

The shoreline position from the experimental data made dimensionless by U_s^2/g is plotted in Figure 3.50 with the theoretical solutions of the shoreline position. Since the overturning jet of the plunging breakers crashed onshore of the stillwater shoreline, the data for shoreline position do not begin at $a = 0$. The average starting position for the plunging breakers is $ag/U_s^2 = 0.29$ and the theoretical solutions are also initialized at this value. The theoretical solutions provide an excellent match to the experimental data up to $gt/U_s = 3$, after which there is some deviation between the data of different waves, the Taylor series approximate solution and the numerical solution.

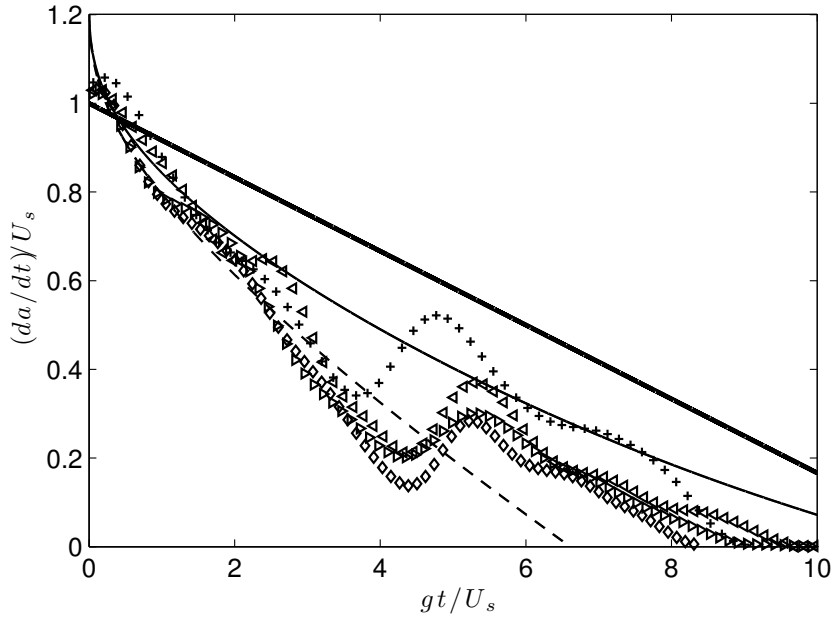

Figure 3.49: Dimensionless shoreline velocity, comparison of experimental data to theoretical solutions. +, W7 data; ◁, W8 data; ▷, W9 data; ◇, W10 data; ——, frictionless solution, Eq. (3.9) with $s = 1/12$; ——, numerical solution, Eq. (3.33) with $s = 1/12$ and $K = 0.005$; — —, Taylor series solution, Eq. (3.37) with $s = 1/12$ and $K = 0.005$.

The run-up, R, is presented in Table 3.6 from four sources: (i) experimental data, R; (ii) predictions of numerical solution to Eq. (3.33), R_{num}; (iii) predictions of the Taylor series approximate solution, R_{Tay}; (iv) predictions from the frictionless solution, $R_{\text{frictionless}}$. The Taylor series approximate solution under-predicts the run-up, whereas the numerical solution over-predicts it, but both provide a significant improvement to the predictions of the frictionless solution despite the fact that the results of the theory are difficult to interpret at large times.

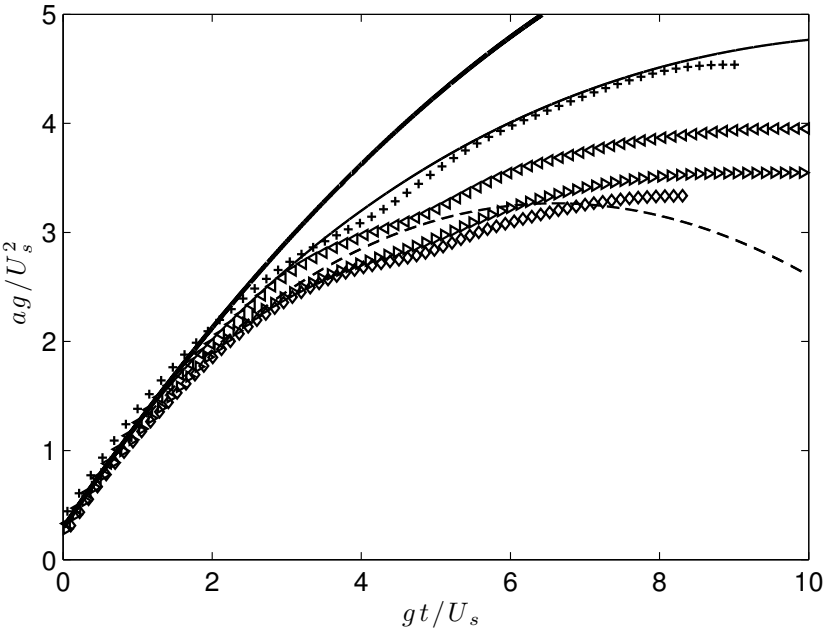

Figure 3.50: Dimensionless shoreline position, comparison of experimental data to theoretical solutions. +, W7 data; ◁, W8 data; ▷, W9 data; ◇, W10 data; ——, frictionless solution, Eq. (3.9) with $s = 1/12$; ——, numerical solution, Eq. (3.33) with $s = 1/12$ and $K = 0.005$; — —, Taylor series solution, Eq. (3.37) with $s = 1/12$ and $K = 0.005$.

Wave	ϵ_0 (-)	U_s (ms^{-1})	R (m)	R_{Tay} (m)	R_{num} (m)	$R_{\text{frictionless}}$ (m)
W7	0.199	5.0	0.96	0.69	1.03	1.27
W8	0.237	5.7	1.09	0.90	1.33	1.66
W9	0.256	6.2	1.16	1.07	1.58	1.96
W10	0.286	6.6	1.23	1.21	1.78	2.22

Table 3.6: Comparison of run-up predictions to data. The value of the friction coefficient used in the calculations of run-up from the theoretical solutions is $K = 0.005$.

3.10 Concluding remarks

The shoaling, swash zone flow and run-up of solitary waves were investigated using large-scale experiments that allowed the study of single swash events at scales relevant to the field scale and the results compared to known theoretical results, where available. Ten solitary waves with systematically varying amplitudes that span the range of incident non-linearity $0.05 \leq \epsilon_0 \leq 0.3$ were used. This range spans from the longest wavelength solitary wave that would fit in the wave flume to the largest amplitude wave that can be resonably generated using a piston-type wavemaker. The generated solitary waves were incident upon a plane, impermeable beach of slope $s = 1/12$ to generate swash events of non-breaking waves, surging breakers and plunging breakers. The variation of the solitary wave amplitude near the toe of the beach was investigated to find that wave amplitude increases as the local water depth decreases following a power law, where the exponent in the power law decreased in magnitude for larger amplitude waves, indicating that larger amplitude waves do not significantly alter their wave height as they run into shallower water and break. Smaller amplitude waves show a wave amplitude increase that approaches that given by Green's law, consistent with previous results in the literature.

Measurements in the swash zone showed that during uprush, the bed shear stress is most significant near the swash tip when the flow has a significant amount of entrained air, and during downrush, near the end of the downrush when the water depth is very shallow. For the duration inbetween, the bed shear stress is low, and the flow of breaking solitary waves is controlled by gravity and follows the swash solution, Eq. (3.10). Furthermore, bore collapse as described by Whitham's rule, Eq. (3.5), was shown to provide an initial condition compat-

ible with the swash solution. The controlling scale of the swash, which is also a measure of the initial energy of the swash, was shown to be the only free parameter in the swash solution, the swash initiation shoreline velocity. This velocity scale was measured or predicted in three different ways: (i) using Whitham's rule, Eq. (3.5), and measurements of the height of the solitary wave just before it breaks; (ii) measurements of the shoreline velocity immediately after wave collapse; (iii) calculation of the characteristic variable, $\alpha = \overline{u} + 2c + gst_s$, using measurements in the swash. How the kinematics of different breaker types affects the swash initiation shoreline velocity was investigated and the variation of this velocity with breaker type was plotted. Further data is necessary to understand the dependency of the swash initiation shoreline velocity on the breaker type on different slopes. From an engineering perspective, it would be useful to be able to predict the defining scale of the swash, U_s, based on knowledge of incident ocean waves, but currently, there are no analytical methods available to do this (Svendsen, 2006).

A large increase ($O(7)$-fold) in the maximum magnitude of the uprush bed shear stress for breaking waves compared to pre-breaking magnitudes was observed, as expected, but a large increase ($O(6)$-fold) was also observed for non-breaking waves across the stillwater shoreline. This data suggests that the mechanism that generates much higher values of the bed shear stress in the swash zone compared to pre-breaking wave boundary layer is the continually developing boundary layer in the tip of the swash. For the same reason, the maximum onshore-directed bed shear stresses observed were significantly larger than the maximum offshore-directed bed shear stresses. The maximum onshore- and offshore-directed bed shear stresses in the swash for different breaker types were collapsed under a new normalization that used the swash

initiation shoreline velocity. The fact that data from different types of breakers collapsed under this normalization provides confidence that the swash initiation shoreline velocity is also an important scale for the bed shear stress in the swash.

The run-up of non-breaking and breaking solitary waves was shown to be well-parameterized by the solitary wave slope parameter and it was shown that the maximum dimensionless run-up is $R/H_0 \approx 4$ and it occurs for waves that barely break ($S_0 \approx 0.4$). The run-down measurements showed that the magnitude of the dimensionless run-down, R_d/H_0, is also maximum for waves that barely break during downrush, i.e., they cause the weakest hydraulic jump during downrush.

A theory was developed to treat the swash tip and the effects of bed friction in an integral sense during the swash uprush by extending the 'Pohlhausen method' used by Whitham (1955). The swash tip was modelled as a friction-affected region of uniform velocity and behind the swash tip, the flow evolution was given by the frictionless swash solution, Eq. (3.10). The theory was used to obtain trajectories of the shoreline, which were compared to the data of plunging breakers. The theory demonstrated the ability to capture the leading order dynamical balance at the moving shoreline during the initial stages of the swash and also provided predictions of the run-up that agreed well with experimental data without the need for *ad hoc* assumptions.

Finally, the total time duration of a swash event can be of importance in the overall mechanics of the swash zone, particularly so if there are interactions of swash events (Masselink and Puleo, 2006). The interaction of swash events is considered in the following chapter.

CHAPTER 4

SWASH OF TWO SUCCESSIVE SOLITARY WAVES

4.1 Introduction

In chapter 3, the use of solitary waves as an input to the swash offered the advantage that a single swash event could be studied in isolation. This was a limitation imposed to avoid the complexities that arise when the swash of one wave interacts with the swash of the next wave, but the swash zone on natural beaches is often characterized by the interaction of successive swash events and this interaction has been identified as an important feature for sediment transport (Puleo and Butt, 2006; Hughes and Moseley, 2007), run-up (Erikson *et al.*, 2005) and the generation of low frequency waves (Watson *et al.*, 1994; Brocchini and Baldock, 2008). Thus, the interaction of waves in the swash now considered.

Recent studies (Alsina *et al.*, 2012; Cáceres and Alsina, 2012) have shown the importance of swash-swash interactions – such interactions produce events that are significant for suspended sediment concentrations and there is a need to analyse the swash zone on a wave-by-wave basis, rather than looking at data averaged over many waves. Along such a line of enquiry, Lo *et al.* (2013) studied the run-up of successive solitary waves with varying separation times between successive wave crests. The focus was on the run-up, but the interactions between swash events was not explored. Therefore, the experiments presented in this chapter were conducted: to study the incteraction of swash events from successive solitary waves, focusing on two specialized cases of two successive solitary waves that result in two qualitatively different types of swash-swash interactions.

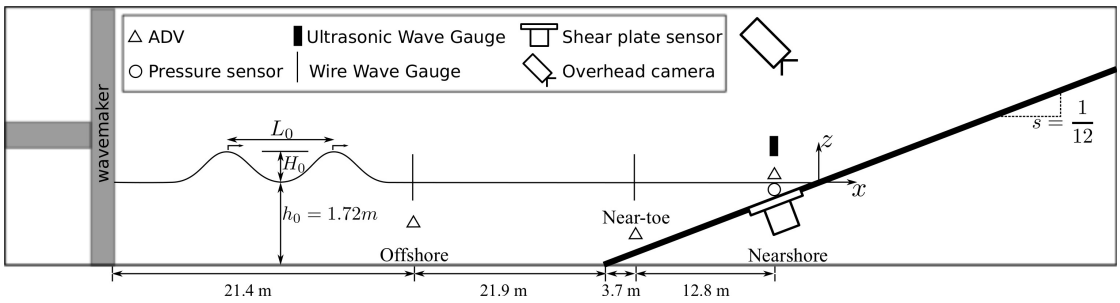

Figure 4.1: Schematic of experimental setup. The local stillwater depths at the near-toe location and nearshore location were h = 1.42 m and h = 0.1 m, respectively.

4.2 Experimental setup

The experimental setup was essentially the same as described in chapter 3: experiments were conducted in the Large Wave Flume (LWF) at the Hinsdale Wave Research Laboratory at Oregon State University, which is a flume of length 104 m, width 3.7 m and depth 4.6 m deep equipped with a piston-type wavemaker installed at one end of the flume and a plane beach of slope 1:12 at the other end. The water depth was kept constant at h_0 = 1.72 m throughout the experiments. The setup is shown in Figure 4.1. The incident waves were measured at the 'offshore location' that was at a distance of 21.4 m from the the wave-maker in its fully retracted position. Measurements were made of the free-surface displacement using a resistance-type wave gauge and the water particle velocity using an ADV installed at a depth of 1.1 m below the stillwater free-surface. Further measurements of the free-surface displacement and water particle velocity (using an ADV installed at a depth of 0.8 m below the stillwater free-surface) were also made at a location near the toe of the beach, the 'near-toe location', where the local stillwater depth was h = 1.42 m.

To allow the study of the interaction between the downrush of the first wave

and the uprush of the second wave, additional measurements were made at the 'nearshore location', situated at $x = -1.21$ m (location L2 in chapter 3). The local stillwater depth at the neashore location was $h = 0.10$ m. Measurements were made to study the interaction between the downrush of the first wave and the uprush of the second wave: the local bed shear stress was measured using the shear plate sensor, the free-surface elevation was measured directly above the center of the shear plate sensor using an ultrasonic wave gauge (Senix TS-30S1 series; accuracy 1 mm), the bed pressure was measured using a pressure transducer (Druck PDCR 830; accuracy 30 Pa) at the same cross-shore location but shifted in the long-shore direction from the shear plate, and the near-bed velocity was measured using a side-looking ADV (Nortek Vectrino with plus firmware) with its measurement volume centred at a height of 2 cm above the bed pressure sensor. The instrument setup at the nearshore location was the same as for location L2, described in chapter 3. The setup of the instruments is shown in the photographs in Figure 3.4. The near-bed velocity measurements were not available when the water depth was less than approximately 7 cm because the ADV failed to make reliable measurements. As before, a minimum threshold of 15 dB for the signal to noise ratio (SNR) was applied to the ADV measurements. Apart from the measurements in the swash, the shoreline motion was also tracked as described in chapter 3.

4.3 Incident waves

Two wave cases, denoted as SW1 and SW2, were used to study the interaction of swash events. Each wave case consisted of two successive solitary waves and the letters A and B are used to refer to the first and the second wave, respec-

Wave	H_0 (m)	ϵ_0 (-)	L_0 (m)	T_0 (s)	T_{sep}/T_0 (-)	S_0 (-)	Breaker type	R (m)	R_d (m)
SW1A	0.169	0.098	40.3	9.3	0.96	0.41	NB	0.60	0.17
SW1B	0.170	0.098	40.0	9.3		N/A	SU	0.48	0.18
W3	0.173	0.100	39.6	9.2	N/A	0.40	NB	0.61	0.18
SW2A	0.334	0.193	28.6	6.3	0.93	0.29	PL	0.96	N/A
SW2B	0.331	0.191	28.7	6.4		N/A	SU	0.45	0.25
W7	0.345	0.199	28.1	6.2	N/A	0.28	PL	0.96	0.20

Table 4.1: Properties of incident successive solitary waves and measurements of run-up, R, and run-down, R_d. NB is a non-breaking wave, SU is a surging breaker, PL is a plunging breaker. T_{sep} is the separation time between successive wave crests at the offshore location.

tively. An additional run of SW2 was conducted and the data from the repeated runs are plotted together to demonstrate the high degree of repeatability in the experiments. Table 4.1 gives the properties of the incident waves in the constant depth region and integral properties of the swash such as values of the run-up and run-down. The single solitary wave cases W3 and W7 in chapter 3 correspond very closely to the solitary waves in SW1 and SW2, respectively, which allowed successive solitary wave data to be compared to a single solitary wave case. The values for the effective wavelength, L_0, and the effective period, T_0, are given in Table 4.1 are calculated according to Eq. (1.6) using measurements of the wave height at the offshore location.

Successive solitary waves were generated by creating a composite wavemaker trajectory where the trajectory for a single solitary wave was performed twice successively with no time delay in between so that the separation of wave crests was approximately T_0. Figure 4.2 shows the wavemaker trajectory for two successive solitary waves compared to the wavemaker trajectory for single

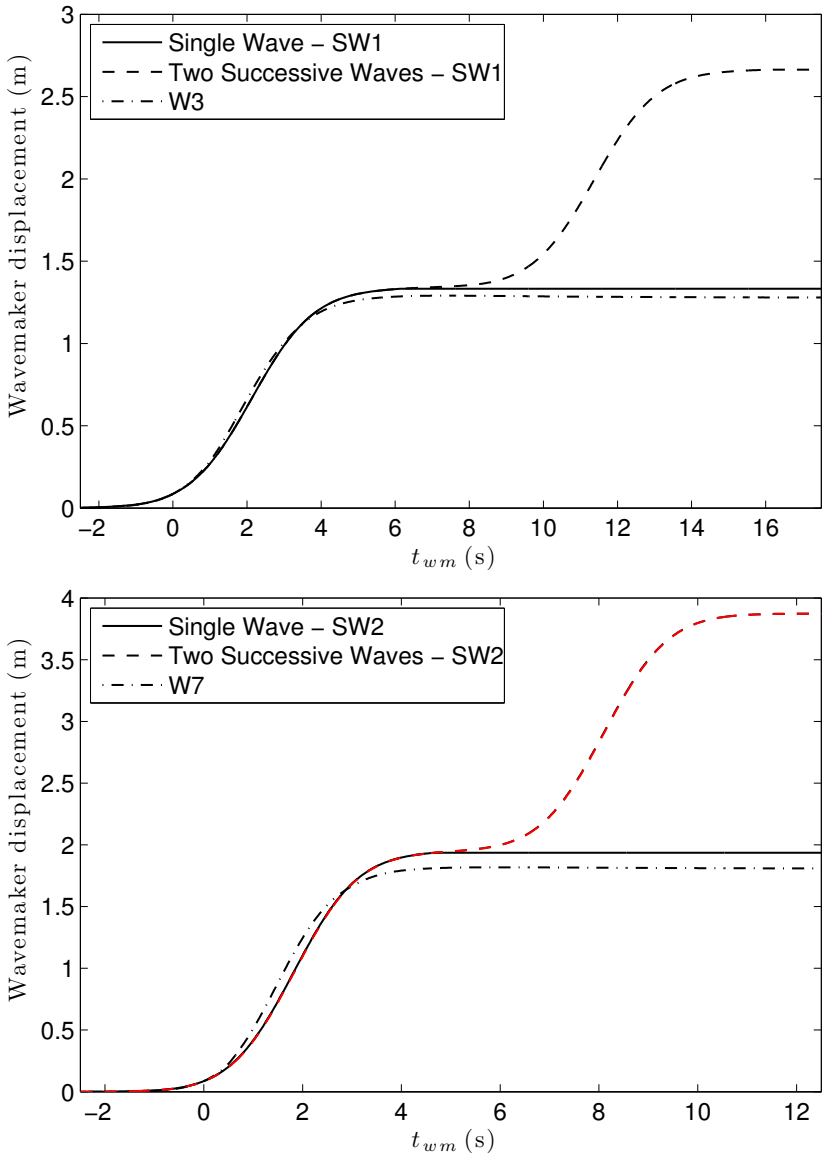

Figure 4.2: Wavemaker trajectories for incident successive solitary waves. *Top*: SW1; *Bottom*: SW2, data from the repeated run is plotted in red and shows a very good match to the first run..

solitary wave. The successive waves were thus generated with identical wavemaker motion, but a slow evolution led to slightly different wave heights. This slow evolution of successive waves had negligible influence on the results of interest - even the shortest wave, SW2A, travelled a horizontal distance of only approximately twice its own wavelength before reaching the toe of the sloping beach - and the swash was essentially driven by two successive identical solitary waves separated by the wavelength of a single solitary wave (Table 4.1).

At the offshore location, the free-surface displacement of the waveforms are compared to the Boussinesq solution in Figure 4.3. Wave A in both cases matches the Boussinesq solution very well, whereas the trailing edge of wave B shows some discrepancy. In SW1, the raised free-surface near the trailing edge of wave B is due to the reflection of wave A from the sloping beach, which occurs because of the long wavelengths of the SW1 waves compared to the limited length of the flume.

4.4 SW2 – Strongly interacting case

The key features in the swash of SW2 are depicted in Figure 4.4, including the wave collapse location, where the wave overturning jet reconnected with land/water in front of it and the waveform was first seen to disintegrate into water with air entrained.

The swash zone flow of the first wave follows the swash solution, Eq. 3.10, like wave W7 of chapter 3, until the arrival of the second wave, SW2B. Figure 4.5 plots the position of the swash tip, x_s, of the swash for SW2. For the swash of the first wave, the swash tip coincides with the shoreline and can be identi-

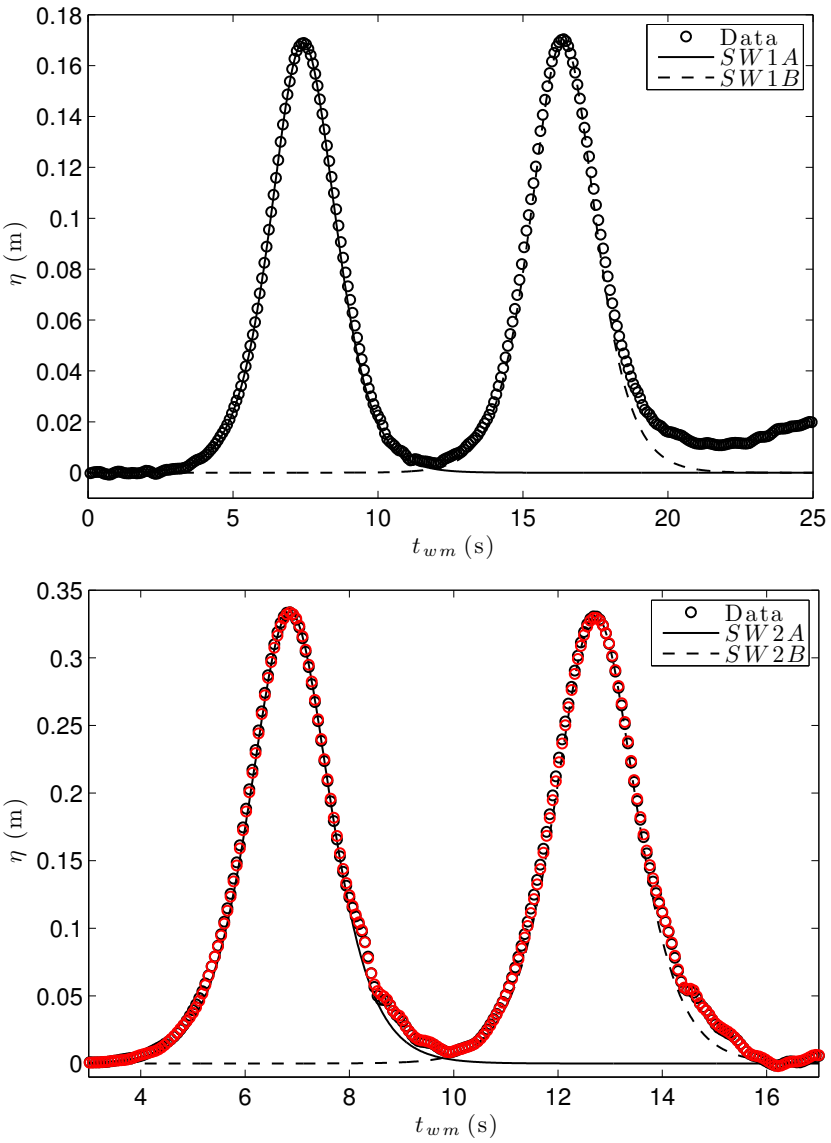

Figure 4.3: Free-surface displacement for incident successive solitary waves. *Top*: SW1; *Bottom*: SW2, Data from the repeated run is plotted in red and shows a very good match to the first run.

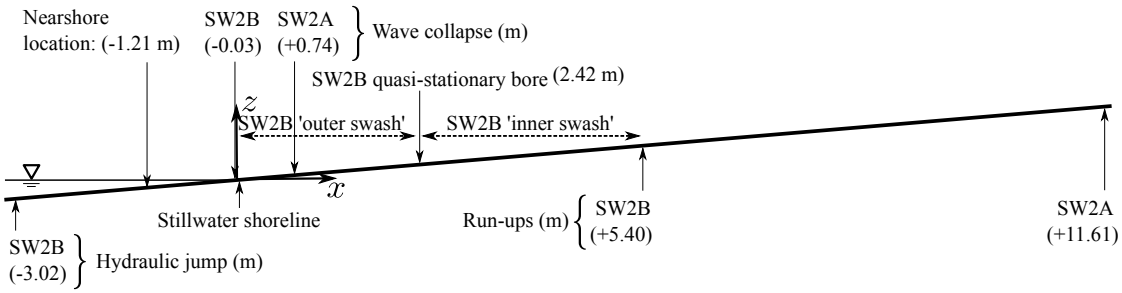

Figure 4.4: A diagram, to scale, of the swash zone for SW2. Numbers in brackets show the value of x, the distance along the beach measured from the stillwater shoreline. Dashed arrows indicate the extents of 'outer swash' and 'inner swash' for SW2B.

fied from the overhead camera images, whereas for the second wave, the actual shoreline was difficult to identify due to the wet surface and the extremely thin-layered flow. The swash tip for SW2A travels in a very similar trajectory to the swash tip for wave W7, leading to a very similar run-up (see Table 4.1), but the swash tip for SW2B follows a very different trajectory. The wavefront of SW2B collapses at a location further offshore than the collapse of SW2A (Figure 4.4). As the swash tip for SW2B climbs the slope against the downrush of SW2A, there is a strong interaction between the two flows and the swash tip of SW2B is held in space temporarily by the downrush of SW2A and a quasi-stationary bore occurs at $x \approx 2.42$ m and $t_{wm} \approx 23$ s. The swash tip of SW2B then climbs further up the beach to reach a run-up that is approximately 45% of the run-up of SW2A – a significant reduction due to the strong interaction between the second wave uprush and the first wave downrush. The flow velocity at the location of the quasi-stationary bore at $x \approx 2.42$ m must be negative after the bore collapses at $t_{wm} \approx 23$ s, making the interaction a 'strong wave-downrush interaction' (Hughes and Moseley, 2007; Cáceres and Alsina, 2012; Alsina *et al.*, 2012). The swash flow of SW2B in the region $2.42 < x < 5.40$ m is in the 'inner swash' according to the Hughes and Moseley (2007) classification since that region does

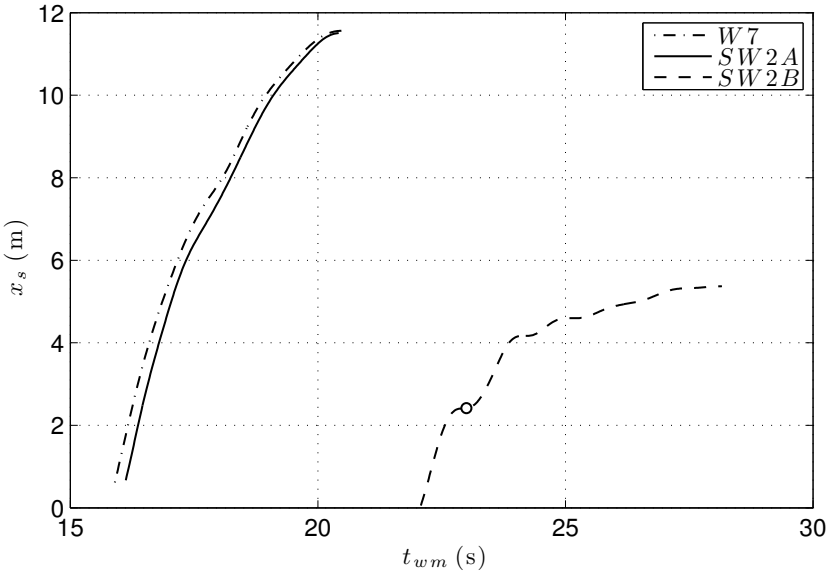

Figure 4.5: Shoreline (or swash tip) motion for SW2.

not experience interacting swash events (see Figure 4.4), but it is clear from the trajectory of the swash tip that the swash flow in this inner swash is weakened by the interaction further offshore. The hydraulic jump of the downrush of the combined swash flow occurs offshore of the stillwater shoreline, as shown in Figure 4.4.

Figure 4.6 plots the free-surface displacement and the horizontal velocity at the near-toe location (see Figure 4.1). There are two incident waves, with positive free-surface displacement and positive (onshore-directed) velocity, but the signal due to the reflection of the waves (negative, offshore-directed velocity) shows a merged reflected wave with a peak in free-surface displacement at $t \approx 31$ s. This feature is further evidence of the strong interaction between the swash events, since the reflected wave signal does not show two distinct waves (cf. Lo *et al.*, 2013).

Figure 4.7 plots the free-surface displacement, η, the bed pressure, p_b, the

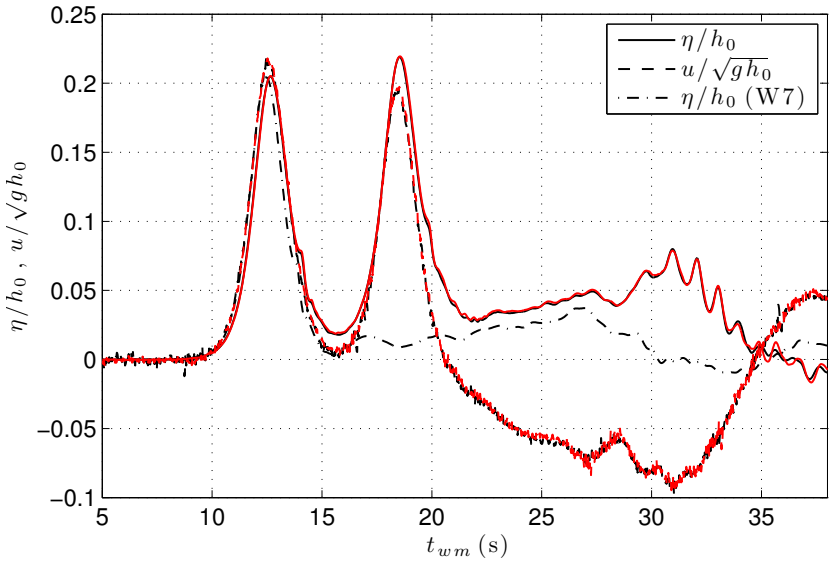

Figure 4.6: Free-surface displacement, η, and horizontal velocity, u, at near-toe location, h = 1.42 m, for SW2. Data from the repeated run is plotted in red and shows a very good match to the first run. The hump at $t_{wm} \approx 31$ s corresponds to the reflected wave due to the combined swash events of SW2.

near-bed velocity, u, and the bed shear stress, τ_b, at the measurement location for SW2. At t_1 = 16.3 s, there exist fluctuations in bed pressure and bed shear stress that are likely due to the collapse of SW2A, as discussed in section 3.4.1. Time t_2 = 19 s is the start of the downrush at the nearshore location as the velocity and bed shear stress change sign. The wavefront of SW2B arrives at t_3 = 22 s, but it is insufficiently steep to break – SW2B collapses further onshore as shown in Figure 4.4 – and so there is a smooth transition from offshore-directed flow to onshore-directed flow that is further discussed below. The height of the SW2B wave crest is larger than the wave crest of SW2A, but the peak near-bed velocity is lower, due to the raised water elevation in the downrush of SW2A. Consequently, the peak bed shear stress is lower under the wave crest of SW2B compared to the wave crest of SW2A at this location. The strong interaction between SW2B and the downrush of SW2A occurs onshore of the measurement

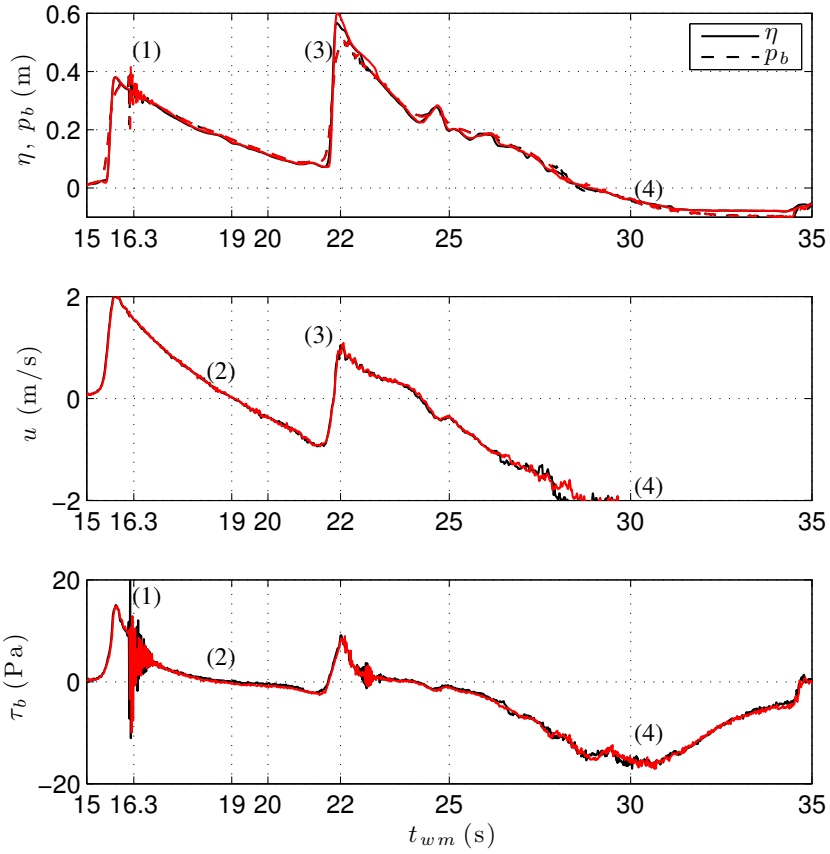

Figure 4.7: Data at nearshore location (x = −1.21 m, h = 0.10 m) for SW2. Top panel: Free-surface displacement, η, and bed pressure, p_b; Middle panel: Near-bed velocity, u; Bottom panel: Bed shear stress, τ_b. Data from the repeated run is plotted in red and shows a very good match to the first run.

location. At the measurement location, the downrush results in a large, negative bed shear stress due to accelerating flow and decreasing water depth (t_4 = 30 s).

Figure 4.8 plots the same data from the nearshore location, but truncated in time around t_3 = 22.0 s to focus on the flow reversal. Vertical accelerations are important in the steep wavefront of SW2B as seen by the difference between the bed pressure and the free-surface elevation. Attention is drawn to the instances marked (3a) and (3b) in Figure 4.8, for which sketches of the velocity profiles and flow patterns are shown in Figure 4.9. At instance (3a), the vertical

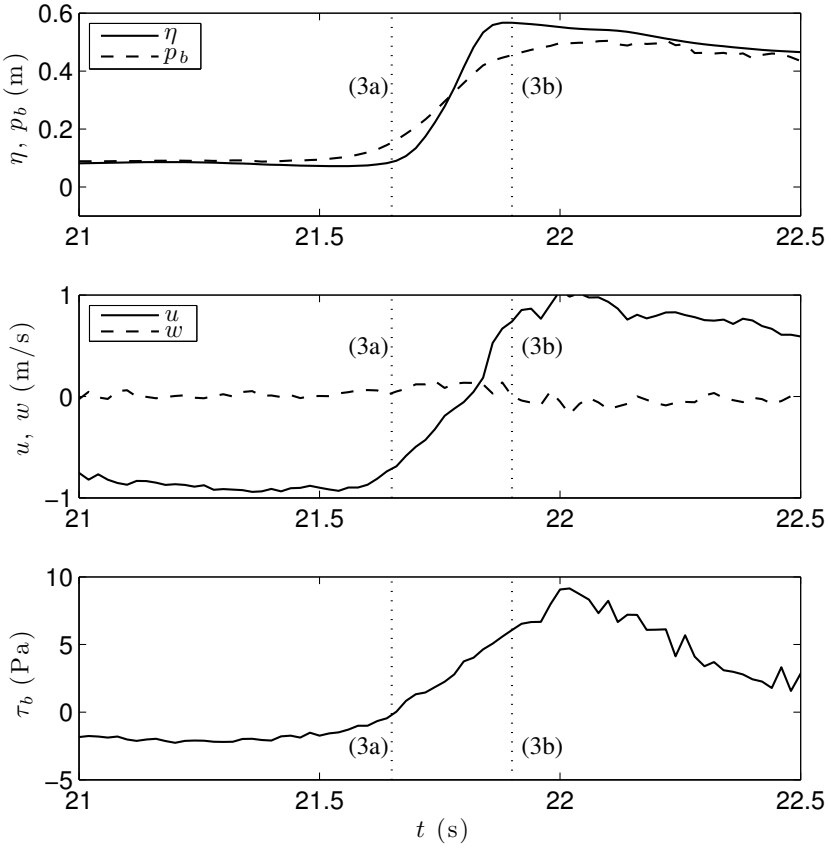

Figure 4.8: Data at nearshore location ($x = -1.21$ m, $h = 0.10$ m) around $t_{wm} = 22$ s for SW2. Top panel: Free-surface displacement, η, and bed pressure, p_b; Middle panel: Near-bed velocity, u; Bottom panel: Bed shear stress, τ_b. Data from the repeated run is plotted in red and shows a very good match to the first run.

acceleration must be positive (upward-directed) to cause an increase in the free-surface steepness and this is accompanied by bed pressure that is higher than hydrostatic, whereas at instance (3b), the vertical acceleration must be negative (downward-directed) to cause a decrease in the free-surface steepness and this is accompanied by bed pressure that is lower than hydrostatic. The bed shear stress goes to zero at instance (3a) while the near-bed velocity is still offshore-directed and before the free-surface begins to rise because of the 'extra' horizontal pressure gradient due to the non-hydrostatic pressure distribution in the

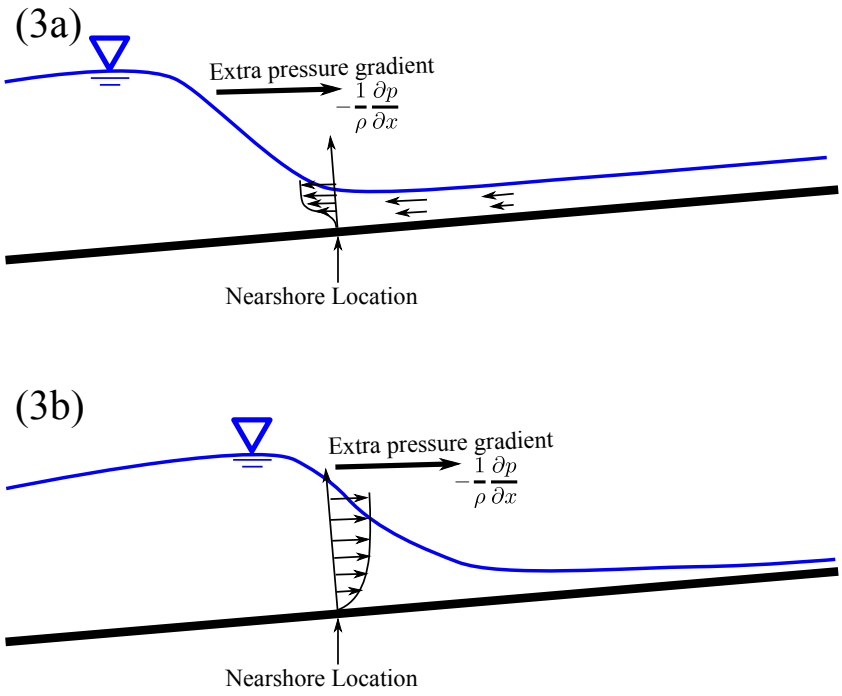

Figure 4.9: Sketch of flow patters and velocity profile corresponding to points (3a) and (3b) in Figure 4.8.

wavefront of SW2B (*e.g.* Peregrine, 1966). Thus, the bed shear stress leads the near-bed velocity and the free-surface elevation in phase at instance (3a). At instance (3b), the near-bed velocity and the bed shear stress are both positive and both become lower in magnitude than behind the wave crest.

4.5 SW1 – Weakly interacting swash events

The key features of the swash of SW1 are depicted in Figure 4.10. As noted in Table 4.1, SW1A is a non-breaking wave and closely matches wave W3. The swash of SW1A is almost complete, *i.e.*, the swash tip for SW1A reaches its run-up and the downrush of SW1A develops into a hydraulic jump, before the wavefront of SW1B arrives. The downrush of SW1A induces breaking in the wavefront of

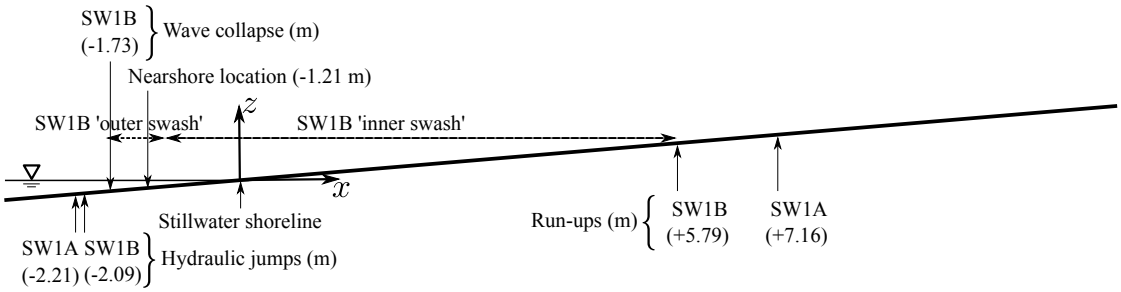

Figure 4.10: A diagram, to scale, of the swash zone for SW1. Numbers in brackets show the value of x, the distance along the beach measured from the stillwater shoreline. Dashed arrows indicate the extents of 'outer swash' and 'inner swash' for SW1B.

SW1B, which collapses at a location onshore of the hydraulic jump caused by the downrush of SW1A. The broken bore of SW2B continues to travel against the downrush of SW1A and creates its own uprush that reaches a run-up 20% lower than that of SW1A. If the run-up of SW1B is measured from the location of the hydraulic jump of SW1A, *i.e.*, the run-down limit of the previous wave (as suggested by Baldock *et al.*, 2008), the run-up of SW1B becomes $R_B = 0.65$ m, even higher, but close to the run-up of SW1A $R_A = 0.6$ m. The interaction between the swash uprush of SW1B and the downrush of SW1A is a 'weak wave-downrush interaction' (Hughes and Moseley, 2007; Cáceres and Alsina, 2012; Alsina *et al.*, 2012) since the velocity continues due to be onshore-directed as the uprush of SW1B climbs to reach a run-up similar to that of SW1A. The weak interaction is evidenced in the motion of the swash tips of SW1A and SW1B, plotted in Figure 4.11, which follow similar trajectories though the swash tip for SW1B forms offshore of the stillwater shoreline.

Figure 4.12 shows the free-surface displacement and horizontal velocity from the near-toe location. It can be seen that there are two distinct reflected waves from the beach that must correspond to reflected components of SW1A

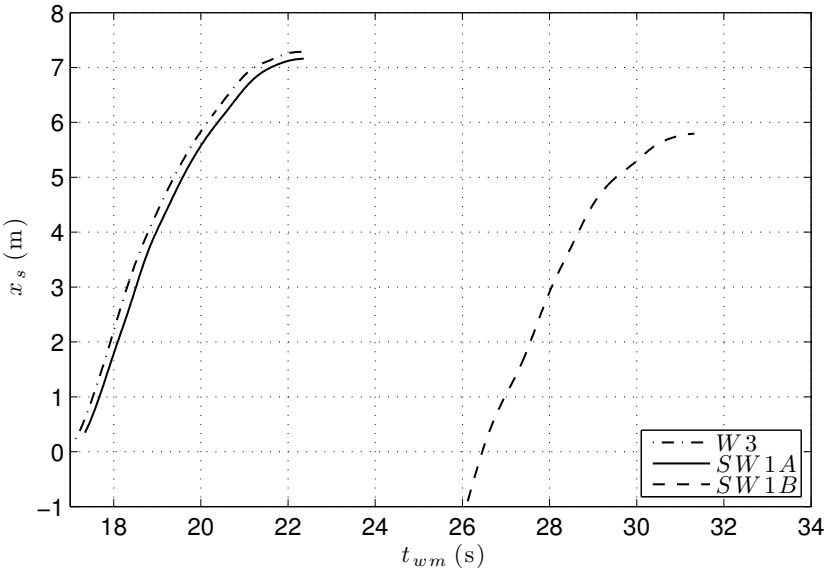

Figure 4.11: Shoreline (or swash tip) motion for SW1.

and SW1B, respectively. Two separate reflected waveforms further indicates that the interaction of the successive swash events is weak.

Figure 4.13 plots the free-surface displacement, η, the bed pressure, p_b, the near-bed velocity, u, and the bed shear stress, τ_b, at the nearshore location for SW1. The wavefront of SW1A, which has mild steepness consistent with its classification as a non-breaking wave, is marked at $t_4 = 16$ s. After the passage of the incident wave, the downrush develops starting at $t_5 = 20$ s and continues until $t_6 = 26.2$ s when the swash tip of of SW1B arrives. The top panel of Figure 4.13 shows that the shoreline during downrush has almost reached the nearshore location at $t_6 = 26.2$ s as the total water depth $\eta + h \approx 0$ (stillwater depth at the nearshore location is $h = 0.1$ m). Thus, almost the entire swash of SW1B is in the 'inner swash' (Hughes and Moseley, 2007) since it is free from interactions of the previous swash event (see Figure 4.10). However, there still exists a large negative velocity associated with the downrush flow at $t_6 = 26.2$

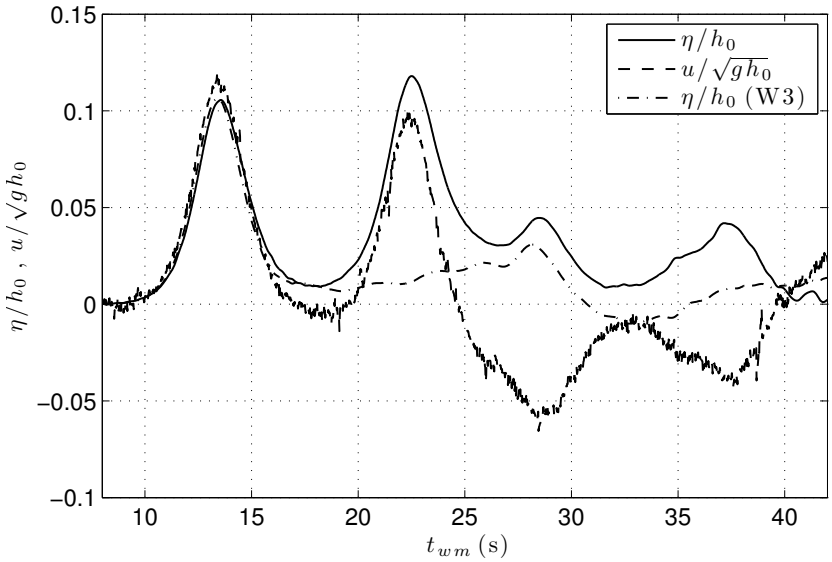

Figure 4.12: Free-surface displacement, η, and horizontal velocity, u, at near-toe location, h = 1.42 m, for SW1. The humps at $t_{wm} \approx$ 28.5 s and $t_{wm} \approx$ 37.5 s correspond to reflected waves due to SW1A and SW1B, respectively.

s and the opposing flow fields create a flow separation at the bed, which is further discussed below. In contrast to the data for SW2, the maximum elevation of the free-surface for SW1B is about the same as SW1A but the peak near-bed velocity is larger for SW1B than SW1A. These differences between SW2 and SW1 are due to the fact that SW1B forms a broken bore by the time it arrives at the nearshore location, whereas SW2B collapses onshore of the nearshore location. The breaking process causes a decrease in wave height and an increase in the water particle velocity.

Figure 4.14 plots the same data from the nearshore location, but truncated in time around t_6 = 26.2 s to focus on the flow separation event. Attention is drawn to the instances marked (6a) and (6b). Prior to instance (6a), there is a large negative bed shear stress in the downrush of SW1A as the water depth is slowly decreasing. There is also a downward tumbling flow in the bore front as

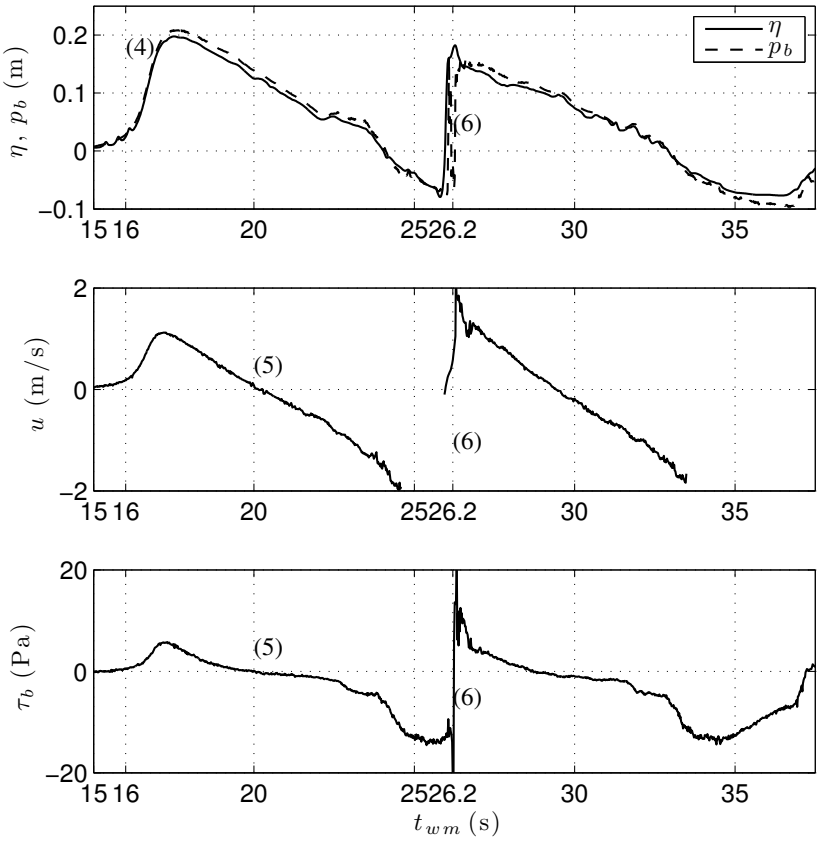

Figure 4.13: Data at measurement location ($x = -1.21$ m, $h = 0.10$ m) for SW1. Top panel: Free-surface displacement, η, and bed pressure, p_b; Middle panel: Near-bed velocity, u; Bottom panel: Bed shear stress, τ_b.

seen from the negative vertical velocity, w. The temporal vertical flow acceleration, $\partial w/\partial t$, is negative and the bed pressure has a lower magnitude than the free-surface elevation, both of which show that this flow is also accompanied by negative (downward-directed) vertical acceleration of fluid particles and non-hydrostatic pressure distribution. At the instance (6a), the pressure suddenly increases, but the bed shear stress still remains negative indicating that the flow nearest to the bed is still offshore-directed due to the downrush of SW1A, but the near-bed velocity is positive. Thus, the flow must be flowing in different directions in the water column. A sketch of the the velocity profiles and flow

patterns is given in Figure 4.15. Immediately after instance (6a), the bed shear stress shows a sudden decrease to a larger negative value, which may be due to boundary layer thinning caused by uprush flow of the bore. Note, that the location of pressure transducer is not exactly the same as that of the shear plate (see Figure 3.4), and the bore front is not precisely two-dimensional (the surface roller of a bore has a three-dimensional structure, Yeh and Mok, 1990). Therefore, the data shown in Figure 4.14 may be subject to contain small discrepancies in timing between instruments. At instance (6b), the bed shear stress transitions from negative to positive and this transition is sudden, suggesting the occurrence of bursting. The negative spike in the bed pressure at instance (6b) indicates that the flow separation is accompanied by positive (upward-directed) vertical acceleration of fluid particles and non-hydrostatic pressure distribution. The near-bed velocity in the horizontal direction remains onshore-directed. The velocity profile and flow patterns for instance (6b) are also sketched in Figure 4.15. Immediately behind the bore front, the magnitude of shear stress becomes much smaller than that of the downrush. As the bore propagates onshore, the flow separation point must move onshore until the bore of SW1B climbs far enough to reach dry land. The dominant bed-load sediment transport in the downrush and the dominant suspended-load sediment transport in the swash zone are discussed by Jackson *et al.* (2004); Pritchard (2009); Cáceres and Alsina (2012) and others. These measurements show the quantitative evidence for the sediment-transport mechanism when there is an interaction of the downrush of the previous wave with the broken bore of the following wave: the strong bed shear stress in the downrush of the previous wave mobilizes sediment as bed-load and the burst-like vertical fluid accelerations associated with the flow separation point picks up the bed-load sediment into the bore. Sou and Yeh

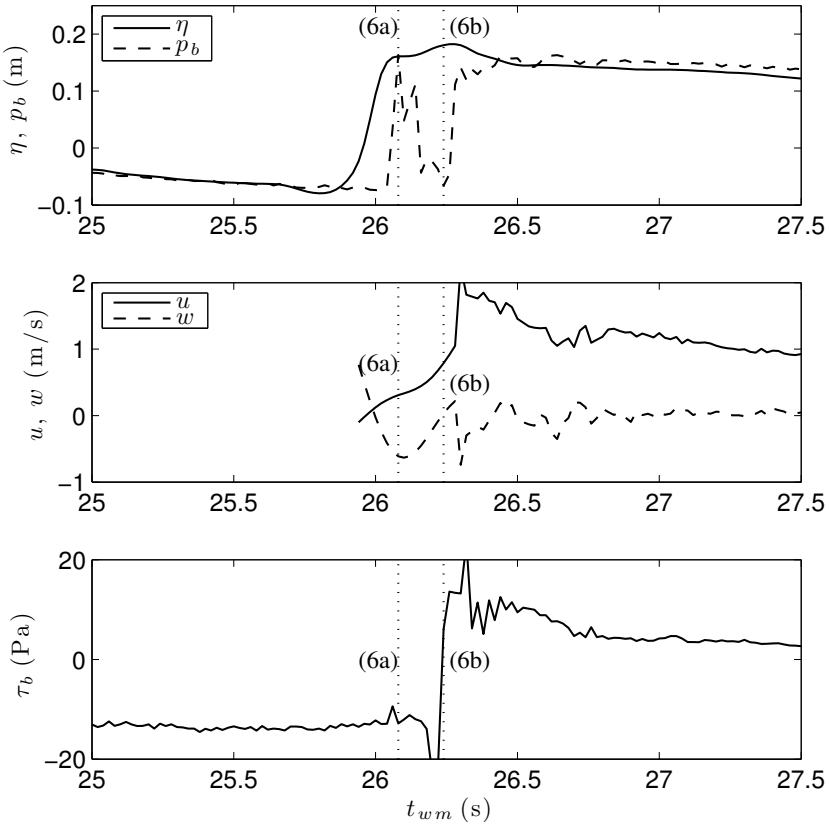

Figure 4.14: Data at nearshore location ($x = -1.21$ m, $h = 0.10$ m) around $t_{wm} = 26.2$ s for SW1. Top panel: Free-surface displacement, η, and bed pressure, p_b; Middle panel: Near-bed velocity, u; Bottom panel: Bed shear stress, τ_b.

(2011) also discussed this mechanism in their study of the swash of plunging regular waves using particle image velocimetry (PIV) measurements, but here it is shown for larger-scale experiments and using the direct measurements of bed shear stress and bed pressure.

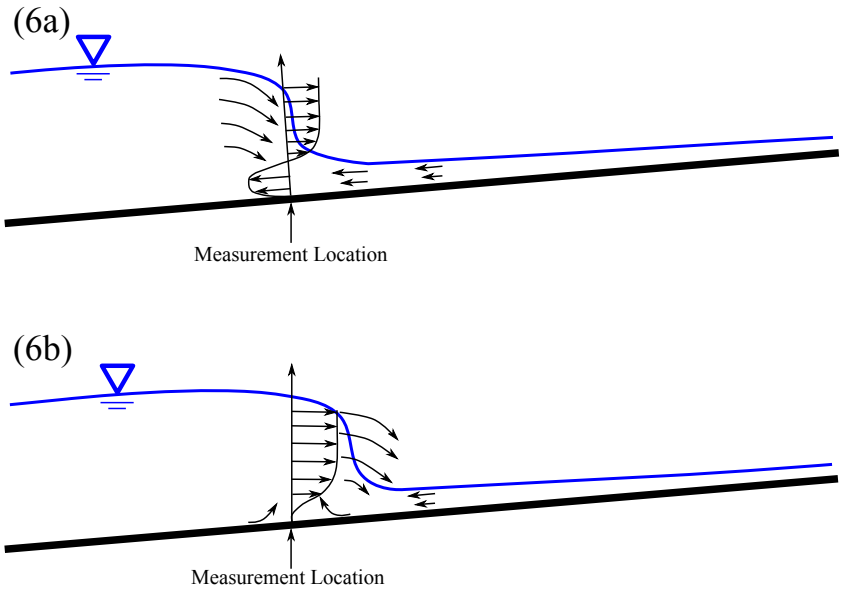

Figure 4.15: Sketch of flow patters and velocity profile corresponding to points (6a) and (6b) in Figure 4.14.

4.6 Run-up of two successive solitary waves

Of the two wave cases studied, SW1, for which wave A did not break and had a higher value of the solitary wave slope parameter, S_0, showed weakly interacting successive swash events. On the other hand, SW2, for which wave A broke as a plunging breaker and had a lower value of S_0, showed strongly interacting swash events. The reduction in run-up of wave B compared to that of wave A provided the most easily visible indication of whether the successive swash events are weakly interacting or strongly interacting.

It would be useful to link the interaction of waves in the swash to the properties of the incident waves and the beach slope. We attempt to establish this link for the swash of two successive solitary waves with wave crests separated by approximately one wavelength using the breaker type of a single solitary wave, *i.e.*, the solitary wave slope parameter, S_0. Figure 4.16, from chapter 3,

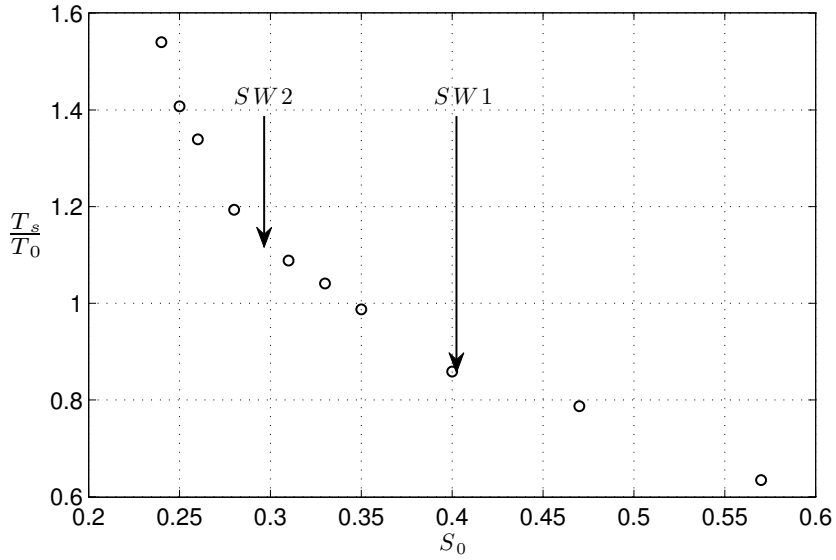

Figure 4.16: The swash period of a single solitary wave, T_s, normalized by effective wave period of incident wave, T_0, as a function of the slope parameter. The arrows show the values of S_0 for the successive wave cases.

plots the swash period, T_s, defined as the time from wave collapse in uprush to the occurrence of the hydraulic jump during downrush, normalized by the incident wave period, T_0, as a function of S_0. As the solitary wave slope parameter decreases, i.e., moving from non-breaking waves to surging breakers to plunging breakers, the time period of the swash relative to the incident wave period increases. For non-breaking waves ($S_0 > 0.37$), $T_s/T_0 < 1$, but for the plunging breakers in PLY15 ($0.025 < S_0 < 0.3$), $T_s/T_0 > 1.2$. For SW1 ($S_0 = 0.41$, $T_s/T_0 \approx 0.85$), the interaction between the wavefront of wave B with the swash of wave A occurs when the swash event of wave A is almost complete, whereas for SW2 ($S_0 = 0.29$, $T_s/T_0 \approx 1.1$), the interaction between wavefront of wave B and the swash of wave A occurs when there is a strong downrush flow.

Figure 4.17 plots the run-up of wave B normalized by the run-up of wave A, R_B/R_A, as a function of the solitary wave slope parameter, S_0. It includes the two

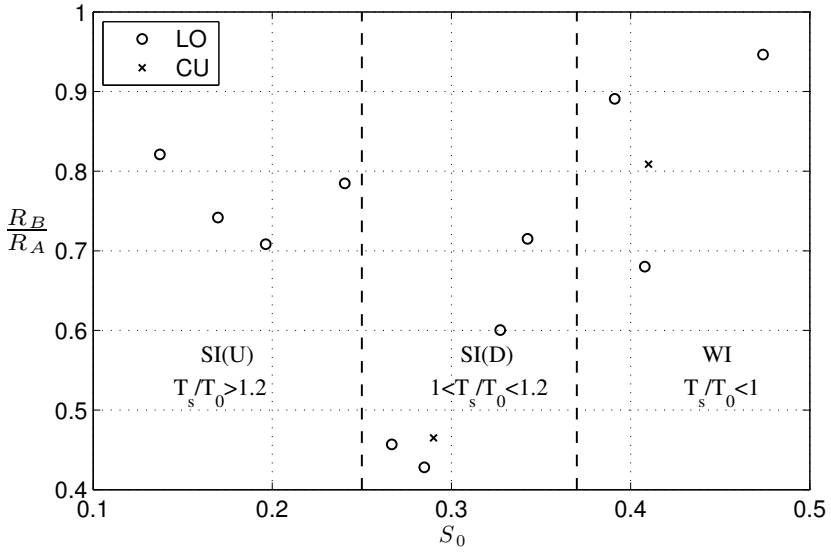

Figure 4.17: Run-up of second wave normalized by run-up of first wave for two successive solitary waves with wave crests separated by $0.9 < T_{\text{sep}}/T_0 < 1.1$. *LO*: Lo *et al.* (2013); *CU*: current data. Dashed vertical lines demarcate different zones: Weakly interacting, WI, $S_0 > 0.37$; Strongly interacting with the majority of the swash in downrush, SI(D), $0.25 < S_0 < 0.37$; Strongly interacting with the majority of the swash in uprush, SI(U), $S_0 < 0.25$.

wave cases from the current study as well as data from Lo *et al.* (2013), which includes measurements from of run-up of two successive solitary waves with wave crests separated by approximately one wavelength on slopes of $s = 1/20$, $s = 1/10$ (small-scale laboratory facilities at DeFrees Hydraulics laboratory at Cornell University) and $s = 1/12$ (LWF at Oregon State University). The overall description of the interaction between two successive solitary waves on a plane beach can be distributed into three different zones in terms of the solitary wave slope parameter, S_0: weakly interacting swash events [WI; $S_0 > 0.37$; $T_s/T_0 < 1$], where the swash event of the first wave is almost complete and the water depth is zero in the majority of the swash zone; strongly interacting swash events [SI(D); $0.25 < S_0 < 0.37$; $1 < T_s/T_0 < 1.2$], where the majority of

the swash of the first wave is in downrush; strongly interacting swash events [SI(U); $S_0 < 0.25$; $T_s/T_0 > 1.2$], where the majority of the swash of the first wave is in uprush. SW1 is an example of a WI event, whereas SW2 is an example of a SI(D) event. WI events are most likely when there is a 'weak wave-downrush interaction', whereas SI(D) events are most likely when there is a 'strong wave-downrush interaction'. SI(U) events are similar to 'wave capture' (Hughes and Moseley, 2007; Cáceres and Alsina, 2012), but the swash tip of the second wave does not necessarily overtake the swash tip of the first wave. The boundaries between the zones are defined here somewhat arbitrarily since in reality, there is a gradual transition between the three types of interactions, but the run-up data in Figure 4.17, R_B/R_A, support the description of the three zones. This characterization is limited to the interaction of only two successive solitary waves and the interaction of a third solitary wave with the swash of the first two might be different, particularly in strongly interacting swash events since the flow conditions under which the third wave climbs the slope will be different to those under which the second wave climbs the slope. Here, the conjecture is put forward that for weakly interacting swash events, the third and subsequent waves would continue to only weakly interact with the previous and following waves. Thus, for weakly interaction waves, the period of shoreline oscillations would remain roughly constant, whereas for strongly interacting waves, the shoreline oscillations will not be periodic but will likely contain a range of timescales, as previously noted by Watson *et al.* (1994), Baldock and Holmes (1999) and others.

4.7 Concluding remarks

The swash of successive solitary waves can be used to study the interaction of waves in the swash zone. Specifically, two successive solitary waves that are separated in the constant depth region by approximately one wavelength of a single solitary wave and their interact on a plane sloping beach were studied. The overall description of the interaction is linked to the ratio of the period of the swash to the period of the incoming waves, T_s/T_0, and in turn to the breaker type of the first wave. T_s/T_0 has been identified as an important parameter in the swash zone (Watson *et al.*, 1994; Baldock and Holmes, 1999; Holland and Puleo, 2001; Masselink and Puleo, 2006; Hughes and Moseley, 2007; Brocchini and Baldock, 2008, and others), but here, results have been shown for isolated swash-swash interaction for different regimes of T_s/T_0 using successive solitary waves. Doing so has allowed the link between the swash period, incident wave period and the breaker type to be indentified.

When the broken bore of the second wave overcomes the downrush of the first wave, there is a flow separation point at the bed with the near-bed flow changing direction from moving offshore to onshore in a bursting manner. In such a flow separation point, measurements of bed shear stress, bed pressure and near-bed velocity show that the offshore-directed velocity persists close to the bed even as the velocity further away from the bed becomes onshore-directed. Thus there exists a shear layer in the velocity profile. Soon after, the bed shear stress changes sign and the velocity throughout the water column becomes onshore-directed. The bed pressure experiences a sudden decrease during the change of sign of bed shear stress that is associated with upward-directed vertical fluid accelerations. This process provides evidence for a mech-

anism by which the sediment mobilized in a sheet flow regime during downrush is transported into the bore of the following wave and advected into the swash zone.

CHAPTER 5

CONCLUSIONS AND FUTURE WORK

5.1 Conclusions

The objectives of the work were to gain a better understanding of the flow of (solitary) waves on (plane, impermeable) beaches, including the spatiotemporal distribution of bed shear stresses to improve the knowledge of the hydrodynamic processes occuring in the swash. The work is divded into three separate parts.

First, the design, development and analysis of the shear plate sensor. Here it was found that a simple design of a passive shear plate forming the top plate of a parallel linkage mechanism whose stiffness is known and whose deflections are measured in order to measure the tangential shear force of a fluid flow leads to a robust sensor that can be used in the nearshore flow conditions. Shear plate sensors are usually limited to zero pressure gradient flows due to the extra force created by streamwise pressure gradients, but with analysis of the flow within the sensor, a new methology was proposed to correct for this extra force extending the utility of shear plate sensors. Essentially, depending upon ratio of the thickness of the shear plate to the width of the gap between the shear plate and the sensor housing, the shear plate 'feels' a fraction of the pressure gradient that exists in the flow. That fraction is within the range $0.5 < f_{pg} < 1$ with an increase in the thickness-to-gap size ratio resulting in a lower value of f_{pg}.

Second, the swash of solitary waves on a plane sloping beach. Here it was found that the approximate solution to bore collapse naturally leads to a swash

flow that is equivalent to the breaking of a dam. Moreover, it was found that the swash of breaking solitary waves follow this solution, which is completely determined from the initial shoreline velocity. Thus, this one measurement can approximately describe the mean flow, neglecting the effects of friction. Since it is difficult to measure the shoreline velocity at the instance when it impulsively starts moving, it was shown that measurements of wave (or bore) height very close to the shoreline can provide a good estimate of the initial shoreline velocity via the bore collapse solution. The most drastic effects of friction were found to be confined within the leading edge of the swash tip during uprush and a simple theoretical model that treats this region in a bulk sense and includes the effects of friction was developed. This model was found to be able to predict the shoreline motion during the initial stages of the uprush when friction is most important.

Third, the swash of successive solitary waves on a plane sloping beach to study swash-swash interactions. Here it was found that when two identical solitary waves follow each other, properties of a single wave are able to predict the nature of the interactions between the two waves in the swash. Measurements in the bottom boundary layer revealed different dynamics depending upon how strongly the swash events interact and the location within the swash.

5.2 Future work

There are several directions in which this work could be expanded and complemented. For the work in chapter 2, the logical extension is to see how well the method for correcting of the pressure gradient force works for other sensors

and other flow conditions, though it was derived without assuming details of any particular sensor or type of flow. It may be possible to re-interpret data previously taken.

The motivation for studying the swash of solitary waves was that it could form a good physical model for wave crests of ocean swells. The next question would be: what about the troughs? The use of solitary waves meant that there was no offshore-directed flow associated with the incident wave, but as periodic waves approach the shoreline, the wave trough preceding the wave crest may play an important role. Transient waves with leading depressions may form good physical models to study this effect.

Linked to this same line of enquiry is the study of non-linear evolution of waves propagating into shallower water. For solitary waves, it was shown here that the wave height close to the shoreline is difficult to predict from knowledge of the wave in the constant depth region, or even knowledge of the initial growth rate near the toe of the beach. However, the initial growth rate showed a change either side of $S_0 \approx 0.37$, the empirical breaking criterion. Thus, for general long transient waves, could the shoaling be described a parameter similar to the slope parameter, S_0, but one which explicitly contains the effects of dispersion, *i.e.*, $s\mu/\epsilon$? Such a slope parameter reduces back to the fundamental form of S_0, $s/\sqrt{\epsilon}$, for waves under the Boussinesq approximation $\epsilon = O(\mu^2)$. Since the collapse of wave crests leads to swash events, it would seem important to understand how wave crests form and evolve in the nearshore. In that case, the climb of undular (or weak) bores is an important area for further exploration.

The bed shear stress in the downrush may fit a developing flat plate boundary layer model, but this idea has not been explored in this work. The effects of

bed friction in the boundary layer may be leading order importance in the formation of the hydraulic jump since the water depth is so shallow in this phase of the swash. To that end, a general empirical downrush breaking criterion in terms of S_0, based on numerical solutions to the fully non-linear potential equations, would be useful.

Considering successive swash events, there seem to robust qualitative demarcations between different types of interactions, analogous to different types of breaking of a single wave crest (*e.g.*, surging, plunging, *etc.*). If the characteristic variable, α, gives a useful characterization of a single swash event, how this variable evolves in space and time in successive swash events would be worth exploring. This would enable building an understanding of the swash on a wave-by-wave basis. Finally, further experimental investigations of a porous beach would be useful to understand the likelyhood of fluidization of the bed, especially in the case of swash-swash interactions.

APPENDIX A

DATA REPEATABILITY

To check the repeatability of the data, various experimental runs were repeated. Figures A.1–A.3 plots the data from the comparison between the first run and the repeated run of wave cases of each breaker type (non-breaking, NB; surging breaker; SU, plunging breaker, PL), repeated at different locations on the beach. Table A.1 lists the repeated experimental runs. The data taken in the swash was found to be repeatable to a high degree, as seen in the plots below.

When an experimental run is repeated, the initially dry portion of the beach ($x > 0$) is not in fact completely dry as it is, for example, at the start of the experiments, because residual water from the previous run still forms a damp surface on the beach. Thus, there is a question of whether the beach boundary conditions for a repeated run are the same as a completely dry beach. However, in large-scale experiments, the role of surface tension is diminished and thus a slightly wet beach does not alter the results. This notion was confirmed not only by the plots of data repeatability, but also by visual observations of the run-up: a repeated run was observed to reach the same run-up to within a horizontal distance of ±5 cm, less than 2% of the run-up of wave W1.

Wave	Breaker type	Repeated location
W3	NB	L5
W5	SU	L6
W9	PL	L8

Table A.1: Repeated experimental runs

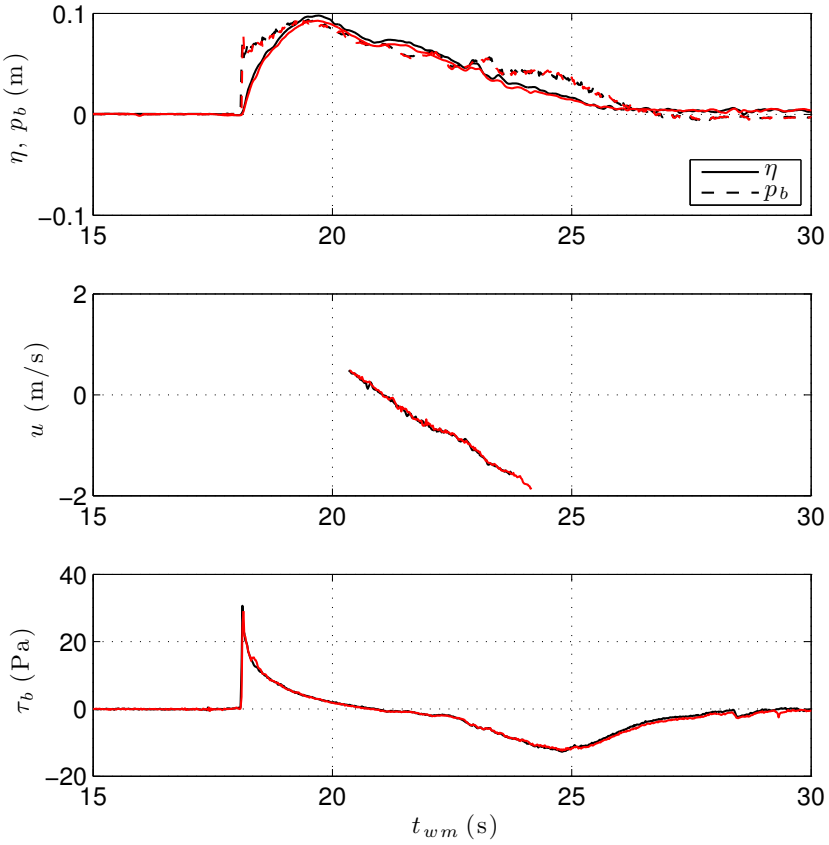

Figure A.1: Comparison of data for repeated runs of for W3 (NB, H_0 = 0.173 m, ϵ_0 = 0.100) at location L5 (x = 2.42 m). Data from the repeated run is plotted in red and shows a very good match to the first run.

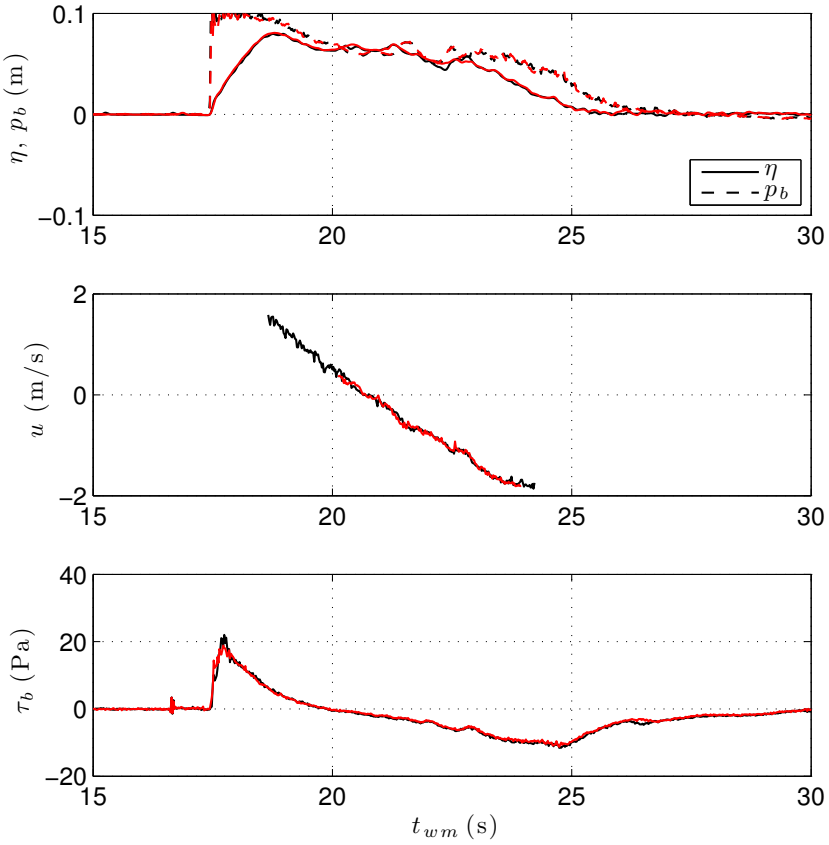

Figure A.2: Comparison of data for repeated runs of for W5 (SU, H_0 = 0.261 m, ϵ_0 = 0.151) at location L6 (x = 3.92 m). Data from the repeated run is plotted in red and shows a very good match to the first run.

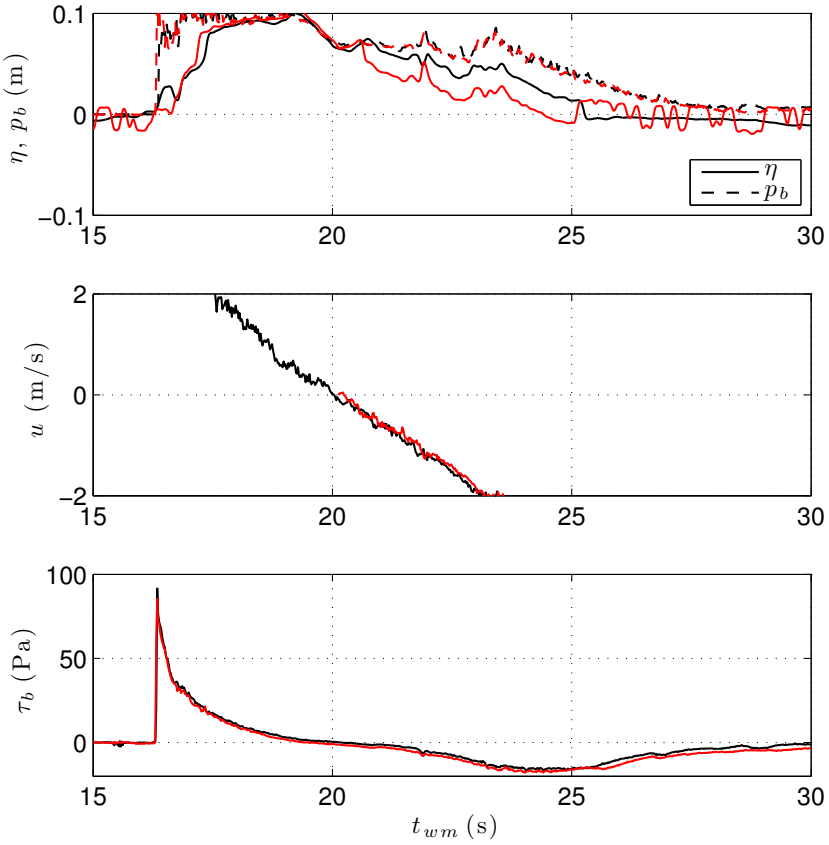

Figure A.3: Comparison of data for repeated runs of for W9 (PL, H_0 = 0.443 m, ϵ_0 = 0.256) at location L8 (x = 6.10 m). Data from the repeated run is plotted in red and shows a very good match to the first run.

REFERENCES

M. Acharya, J. Bornstein, M. P. Escudier, and V. Vokurka. Development of a floating element for the measurement of surface shear stress. *AIAA Journal*, 23:410–415, 1985.

J. M. Allen. Experimental study of error sources in skin-friction balance measurements. *Journal of Fluids Engineering*, 99:197–204, 1977.

J. M. Allen. An improved sensing element for skin-friction balance measurements. *AIAA Journal*, 18:1342–1345, 1980.

J. M. Alsina, I. Cáceres, M. Brocchini, and T. E. Baldock. An experimental study on sediment transport and bed evolution under different swash zone morphological conditions. *Coastal Engineering*, 68:31–43, 2012.

M. Antuono, L. Soldini, and M. Brocchini. On the role of the Chezy frictional term near the shoreline. *Theoretical and Computational Fluid Dynamics*, 26:105–116, 2012.

R. Bakhtyar, D. A. Barry, L. Li, D. S. Jeng, and A. Yeganeh-Bakhtiary. Modeling sediment transport in the swash zone: A review. *Ocean Engineering*, 36:767–783, 2009.

T. E. Baldock and P. Holmes. Simulation and prediction of swash oscillations on a steep beach. *Coastal Engineering*, 36:219–242, 1999.

T. E. Baldock and M. G. Hughes. Field observations of instantaneous water slopes and horizontal pressure gradients in the swash-zone. *Continental Shelf Research*, 26:574–588, 2006.

T. E. Baldock, A. Kudo, P. A. Guard, J. M. Alsina, and M. P. Barnes. Lagrangian measurements and modelling of fluid advection in the inner surf and swash zones. *Coastal Engineering*, 55:791–799, 2008.

T. E. Baldock, R. Grayson, B. Torr, and H. E. Power. Flow convergence at the tip and edges of a viscous swash front — Experimental and analytical modeling. *Coastal Engineering*, 88:123–130, 2014.

J. W. Barker and G. B. Whitham. The similarity solution for a bore on a beach. *Communications on Pure and Applied Mathematics*, 33:447–460, 1980.

M. P. Barnes, T. O'Donoghue, J. M. Alsina, and T. E. Baldock. Direct bed shear stress measurements in bore-driven swash. *Coastal Engineering*, 56:853–867, 2009.

J. A. Battjes. Surf similarity. *Proceedings of 14th International Conference on Coastal Engineering*, 1:466—480., 1974.

R. A. Beach and R. W. Sternberg. Suspended sediment transport in the surf zone: Response to incident wave and longshore current interaction. *Marine Geology*, 108:275–294, 1992.

M. Boers. *Surf Zone Turbulence: Turbulentie in de brandingszone*. PhD thesis, Delft University of Technology, 2005.

J. Boussinesq. Théorie des ondes et des remous qui se propagent le long d'un canal rectangulaire horizontal, en communiquant au liquide contenu dans ce canal des vitesses sensiblement pareilles de la surface au fond. *Journal de mathématiques pures et appliquées*, 17:55–102, 1872.

M. J. Briggs, C. E. Synolakis, G. S. Harkins, and D. R. Green. *Laboratory experiments of tsunami runup on a circular island*, pages 569–593. Springer, 1995.

M. Brocchini. Integral swash-zone models. *Continental Shelf Research*, 26:653–660, 2006.

M. Brocchini and T. E. Baldock. Recent advances in modeling swash zone dynamics: Influence of surf-swash interaction on nearshore hydrodynamics and morphodynamics. *Reviews of Geophysics*, 46:RG3003, 2008.

M. Brocchini and N. Dodd. Nonlinear shallow water equation modeling for Coastal Engineering. *Journal of Waterway, Port, Coastal, and Ocean Engineering*, 134:104–120, 2008.

K. C. Brown and P. N. Joubert. The measurement of skin friction in turbulent boundary layers with adverse pressure gradients. *Journal of Fluid Mechanics*, 35:737–757, 1969.

T. Butt and P. Russell. Hydrodynamics and cross-shore sediment transport in the swash-zone of natural beaches: a review. *Journal of Coastal Research*, 16: 255–268, 2000.

I. Cáceres and J. M. Alsina. A detailed, event-by-event analysis of suspended sediment concentration in the swash zone. *Continental Shelf Research*, 41:61–76, 2012.

F. E. Camfield and R. L. Street. Shoaling of solitary waves on small slopes. *Journal of Waterway, Port, Coastal, and Ocean Engineering*, 95:1–22, 1969.

G. F. Carrier and H. P. Greenspan. Water waves of finite amplitude on a sloping beach. *Journal of Fluid Mechanics*, 4:97–109, 1958.

Y. H. Chang, K. S. Hwang, and H. H. Hwung. Large-scale laboratory measurements of solitary wave inundation on a 1:20 slope. *Coastal Engineering*, 56: 1022—1034, 2009.

D. E. Coles. *Measurements in the boundary layer on a smooth flat plate in supersonic flow*. PhD thesis, California Institute of Technology, 1953.

D. C. Conley and J. G. Griffin. Direct measurements of bed stress under swash in the field. *Journal of Geophysical Research*, 109:C03050, 2004.

E. A. Cowen and S. G. Monismith. A hybrid digital particle tracking velocimetry technique. *Experiments in Fluids*, 22:199–211, 1997.

E. A. Cowen, I. M. Sou, P. L.-F. Liu, and B. Raubenheimer. Particle image velocimetry measurements within a laboratory-generated swash zone. *Journal of Engineering Mechanics*, 129:1119–1129, 2003.

D. T. Cox, N. Kobayashi, and A. Okayasu. Bottom shear stress in the surf zone. *Journal of Geophysical Research*, 101:14337–14348, 1996.

J. P. den Hartog. *Mechanical vibrations*. Dover Publications, 1956.

S. Dhawan. Direct measurements of skin friction. Technical report, California Institute of Technology, 1953.

T. L. Dibble and C. K. Sollitt. New Designs for Acoustic and Resistive Wave Profiles. *IAHR Workshop of instrumentation for hydraulics laboratories*, 1989.

M. W. Dingemans. *Water Wave Propagation Over Uneven Bottoms: Non-linear wave propagation*, volume 13, Pt. 2s of *Advanced Series on Ocean Engineering*. World Scientific, 1997.

B. Efron and R. Tibshirani. *An introduction to the bootstrap*. Chapman and Hall, London, 1993.

G. A. El, R. H. J. Grimshaw, and W. K. Tiong. Transformation of a shoaling undular bore. *Journal of Fluid Mechanics*, 709:371–395, 2012.

B. Elfrink and T. E. Baldock. Hydrodynamics and sediment transport in the swash zone: a review and perspectives. *Coastal Engineering*, 45:149–167, 2002.

L. Erikson, M. Larson, and H. Hanson. Prediction of swash motion and run-up including the effects of swash interaction. *Coastal Engineering*, 52:285–302, 2005.

J. Fenton. A ninth-order solution for the solitary wave. *Journal of Fluid Mechanics*, 53:257–271, 1972.

J. D. Fenton and M. M. Rienecker. A Fourier method for solving nonlinear water-wave problems: application to solitary-wave interactions. *Journal of Fluid Mechanics*, 118:411–443, 1982.

H. H. Fernholz, G. Janke, M. Schober, P. M. Wagner, and D. Warnack. New developments and applications of skin-friction measuring techniques. *Measurement Science and Technology*, 7:1396–1409, 1996.

H. Fischer, E. List, R. Koh, J. Imberger, and N. Brooks. *Mixing in inland and coastal waters*. Academic Press, California, 1979.

D. Frei and H. Thomann. Direct measurements of skin friction in a turbulent boundary layer with a strong adverse pressure gradient. *Journal of Fluid Mechanics*, 101:79–95, 1980.

D. R. Fuhrman and P. A. Madsen. Surf similarity and solitary wave runup. *Journal of Waterway, Port, Coastal, and Ocean Engineering*, 134:195–198, 2008.

C. J. Galvin. *Waves on beaches and resulting sediment transport*, chapter Wave breaking in shallow water, pages 357–411. Academic Press New York, 1972.

C. J. Galvin. Transformation of swell over a reef: Solitons. *Shore & Beach*, 58:31, 1990.

D. G. Goring. *Tsunamis–the propagation of long waves onto a shelf*. PhD thesis, California Institute of Technology, 1978.

S. T. Grilli, R. Subramanya, I. A. Svendsen, and J. Veeramony. Shoaling of solitary waves on plane beaches. *Journal of Waterway, Port, Coastal, and Ocean Engineering*, 120:609–628, 1994.

S. T. Grilli, I. A. Svendsen, and R. Subramanya. Breaking criterion and characteristics for solitary waves on slopes. *Journal of Waterway, Port, Coastal, and Ocean Engineering*, 123:102–112, 1997.

R. Grimshaw. The solitary wave in water of variable depth. Part 2. *Journal of Fluid Mechanics*, 46:611–622, 1971.

J. V. Hall and G. M. Watts. Laboratory investigation of the vertical rise of solitary waves on impermeable slopes. Technical report, Army Coastal Engineering Research Center, 1953.

J. L. Hammack and H. Segur. Modelling criteria for long water waves. *Journal of Fluid Mechanics*, 84:359–373, 1978.

T. J. Hanratty and J. A. Campbell. *Fluid mechanics measurements*, chapter Measurement of wall shear stress, pages 575–648. Taylor and Francis, 1996.

J. H. Haritonidis. *Advances in fluid mechanics measurements*, chapter The measurement of wall shear stress, pages 229–261. Springer, 1989.

S. Hibberd and D. H. Peregrine. Surf and run-up on a beach: a uniform bore. *Journal of Fluid Mechanics*, 95:323–345, 1979.

D. V. Ho and R. E. Meyer. Climb of a bore on a beach. Part 1. Uniform beach slope. *Journal of Fluid Mechanics*, 14:305–318, 1962.

K. T. Holland and J. A. Puleo. Variable swash motions associated with foreshore profile change. *Journal of Geophysical Research*, 106:C3–4613–4623, 2001.

D. P. Horn. Measurements and modelling of beach groundwater flow in the swash-zone: a review. *Continental Shelf Research*, 26:622–652, 2006.

S. C. Hsiao, T. W. Hsu, T. C. Lin, and Y. H. Chang. On the evolution and run-up of breaking solitary waves on a mild sloping beach. *Coastal Engineering*, 55: 975—988, 2008.

M. G. Hughes and A. S. Moseley. Hydrokinematic regions within the swash zone. *Continental Shelf Research*, 27:2000–2013, 2007.

IPCC. *Climate Change 2014: Impacts, Adaptation, and Vulnerability. Part A: Global and Sectoral Aspects. Contribution of Working Group II to the Fifth Assessment Report of the Intergovernmental Panel on Climate Change*. Cambridge University Press, Cambridge, United Kingdom and New York, NY, USA, 2014.

A. T. Ippen and G. Kulin. The shoaling and breaking of the solitary wave. *Proceedings of 5th International Conference on Coastal Engineering*, (1):27–47, 1954.

N. L. Jackson, G. Masselink, and K. F. Nordstrom. The role of bore collapse and local shear stresses on the spatial distribution of sediment load in the uprush of an intermediate-state beach. *Marine Geology*, 203:109–118, 2004.

A. Jensen, G. K. Pedersen, and D. J. Wood. An experimental study of wave run-up at a steep beach. *Journal of Fluid Mechanics*, 468:161–188, 2003.

H. B. Keller, D. A. Levine, and G. B. Whitham. Motion of a bore over a sloping beach. *Journal of Fluid Mechanics*, 7:302–316, 1960.

J. B. Keller and H. B. Keller. Water wave run-up on a beach. Technical Report NONR-3828(00), Office of Naval Research, Department of the Navy, Washington, D.C., 1964.

G. H. Keulegan. Gradual damping of solitary waves. *Journal of Research of the National Bureau of Standards*, 40:487–498, 1948.

G. A. Kikkert, D. Pokrajac, and T. O'Donoghue. Bed shear stress in bore-generated swash on steep beaches. *Proceedings of 6th International Conference on Coastal Dynamics*, pages U56–U57, 2009.

G. A. Kikkert, T. O'Donoghue, D. Pokrajac, and N. Dodd. Experimental study of bore-driven swash hydrodynamics on impermeable rough slopes. *Coastal Engineering*, 60:149—166, 2012.

G. A. Kikkert, D. Pokrajac, T. O'Donoghue, and K. Steenhauer. Experimental study of bore-driven swash hydrodynamics on permeable rough slopes. *Coastal Engineering*, 79:42–56, 2013.

N. Kobayashi and E. A. Karjadi. Surf-similarity parameter for breaking solitary-wave runup. *Journal of Waterway, Port, Coastal, and Ocean Engineering*, 120: 645–650, 1994.

N. Kobayashi and A. R. Lawrence. Cross-shore sediment transport under breaking solitary waves. *Journal of Geophysical Research*, 109:C03047, 2004.

C. Kolitawong, A. J. Giacomin, and L. M. Johnson. Invited Article: Local shear stress transduction. *Review of Scientific Instruments*, 81:021301, 2010.

D. J. Korteweg and G. de Vries. On the change of form of long waves advancing in a rectangular canal, and on a new type of long stationary waves. *Philosophical Magazine*, 39:422–443, 1895.

M. Langsholt. *Experimental study of wave run-up*. PhD thesis, University of Oslo, 1981.

Y. Li. *Tsunamis: Non-breaking and breaking solitary wave run-up*. PhD thesis, California Institute of Technology, 2000.

Y. Li and F. Raichlen. Discussion of" Breaking Criterion and Characteristics for Solitary Waves on Slopes". *Journal of Waterway, Port, Coastal, and Ocean Engineering*, pages 329–335, 1998.

Y. Li and F. Raichlen. Solitary wave runup on plane slopes. *Journal of Waterway, Port, Coastal, and Ocean Engineering*, 127:33–44, 2001.

Y. Li and F. Raichlen. Non-breaking and breaking solitary wave run-up. *Journal of Fluid Mechanics*, 456:295–318, 2002.

Y. Li and F. Raichlen. Energy balance model for breaking solitary wave runup. *Journal of Waterway, Port, Coastal, and Ocean Engineering*, 129:47–59, 2003.

Q. Liao and E. A. Cowen. An efficient anti-aliasing spectral continuous window shifting technique for PIV. *Experiments in fluids*, 38:197–208, 2005.

P. Lin, K. A. Chang, and P. L.-F. Liu. Runup and rundown of solitary waves on sloping beaches. *Journal of Waterway, Port, Coastal, and Ocean Engineering*, 125: 247–255, 1999.

S. C. Ling. Heat transfer from a small isothermal spanwise strip on an insulated boundary. *Journal of Heat Transfer*, 85:230–235, 1963.

P. L.-F. Liu and A. Orfila. Viscous effects on transient long-wave propagation. *Journal of Fluid Mechanics*, 520:83–92, 2004.

P. L.-F. Liu, C. E. Synolakis, and H. Yeh. Report on the international workshop on long-wave run-up. *Journal of Fluid Mechanics*, 229:675–688, 1991.

P. L.-F. Liu, Y. S. Cho, M. J. Briggs, U. Kanoglu, and C. E. Synolakis. Runup of solitary waves on a circular island. *Journal of Fluid Mechanics*, 302:259–285, 1995.

P. L.-F. Liu, G. Simarro, J. Vandever, and A. Orfila. Experimental and numerical investigation of viscous effects on solitary wave propagation in a wave tank. *Coastal Engineering*, 53:181–190, 2006.

P. L. F. Liu, Y. S. Park, and E. A. Cowen. Boundary layer flow and bed shear stress under a solitary wave. *Journal of Fluid Mechanics*, 574:449–463, 2007.

H. Y. Lo, Y. S. Park, and P. L.-F. Liu. On the run-up and back-wash processes of single and double solitary waves—An experimental study. *Coastal Engineering*, 80:1–14, 2013.

S. Longo, M. Petti, and I. J. Losada. Turbulence in the swash and surf zones: a review. *Coastal Engineering*, 45:129–147, 2002.

M. S. Longuet-Higgins. On the Mass, Momentum, Energy and Circulation of a Solitary Wave. *Proceedings of the Royal Society A: Mathematical, Physical and Engineering Sciences*, 337:1–13, 1974.

M. S. Longuet-Higgins and J. Fenton. On the Mass, Momentum, Energy and Circulation of a Solitary Wave. II. *Proceedings of the Royal Society A: Mathematical, Physical and Engineering Sciences*, 340:471–493, 1974.

O. S. Madsen and C. C. Mei. The transformation of a solitary wave over an uneven bottom. *Journal of Fluid Mechanics*, 39:781–791, 1969.

P. A. Madsen and H. A. Schäffer. Analytical solutions for tsunami runup on a plane beach: single waves, N-waves and transient waves. *Journal of Fluid Mechanics*, 645:27–57, 2010.

P. A. Madsen, D. R. Fuhrman, and H. A. Schäffer. On the solitary wave paradigm for tsunamis. *Journal of Geophysical Research*, 113:C12012, 2008.

J. J. Mahony and W. G. Pritchard. Wave reflexion from beaches. *Journal of Fluid Mechanics*, 101:809–832, 1980.

G. Masselink and J. A. Puleo. Swash-zone morphodynamics. *Continental Shelf Research*, 26:661—680, 2006.

C. C. Mei. *The applied dynamics of ocean surface waves*, volume 1 of *Advanced Series on Ocean Engineering*. World Scientific, 1989.

R. E. Meyer and A. D. Taylor. *Waves on beaches and resulting sediment transport*, chapter Run-up on beaches, pages 357–411. Academic Press New York, 1972.

J. W. Miles. Solitary waves. *Annual Review of Fluid Mechanics*, 12:11–43, 1980.

H. Mirfenderesk and I. R. Young. Direct measurements of the bottom friction factor beneath surface gravity waves. *Applied Ocean Research*, 25:269–287, 2003.

R. J. Moffat. Describing the uncertainties in experimental results. *Experimental thermal and fluid science*, 1:3–17, 1988.

W. H. Munk. The solitary wave theory and its application to surf problems. *Annals of the New York Academy of Sciences*, 51:376–424, 1949.

P. Nielsen. *Coastal bottom boudary layers and sediment transport*, volume 4 of *Advanced Series on Ocean Engineering*. World Scientific, 1992.

P. Nielsen. Shear stress and sediment transport calculations for swash zone modelling. *Coastal Engineering*, 45:53–60, 2002.

NOAA. *National Coastal Population Report: Population Trends from 1970 to 2020. Available from http://stateofthecoast.noaa.gov/features/coastal-population-report.pdf (last accessed 26 Nov. 14)*. National Oceanic and Atmospheric Administration, 2013.

T. O'Donoghue, D. Pokrajac, and L. J. Hondebrink. Laboratory and numerical study of dambreak-generated swash on impermeable slopes. *Coastal Engineering*, 57:513–530, 2010.

Y. S. Park. *Seabed dynamics and breaking waves*. PhD thesis, Cornell Univeristy, 2009.

G. K. Pedersen and B. Gjevik. Run-up of solitary waves. *Journal of Fluid Mechanics*, 135:283–299, 1983.

G. K. Pedersen, E. Lindstrom, A. F. Bertelsen, A. Jensen, D. Laskovski, and G. Sælevik. Runup and boundary layers on sloping beaches. *Physics of Fluids*, 25:012102, 2013.

D. H. Peregrine. Calculations of the development of an undular bore. *Journal of Fluid Mechanics*, 25:321–330, 1966.

D. H. Peregrine. Long waves on a beach. *Journal of Fluid Mechanics*, 27:815–827, 1967.

D. H. Peregrine. *Waves on beaches and resulting sediment transport*, chapter Equations for water waves and the approximations behind them, pages 95–121. Academic Press, New York, 1972.

D. H. Peregrine. Breaking waves on beaches. *Annual Review of Fluid Mechanics*, 15:149–178, 1983.

D. H. Peregrine and S. M. Williams. Swash overtopping a truncated plane beach. *Journal of Fluid Mechanics*, 440:391—399, 2001.

S. B. Pope. *Turbulent flows*. Cambridge University Press, 2000.

D. Pritchard. Sediment transport under a swash event: the effect of boundary conditions. *Coastal Engineering*, 56:970–981, 2009.

N. Pujara and P. L. F. Liu. Direct measurements of local bed shear stress in the presence of pressure gradients. *Experiments in fluids*, 55:1767, 2014.

N. Pujara, P. L.-F. Liu, and H. Yeh. The swash of solitary waves on a plane beach: flow evolution, bed shear stress and run-up. *Journal of Fluid Mechanics*, (accepted), 2015.

J. A. Puleo and T. Butt. The first international workshop on swash-zone processes. *Continental Shelf Research*, 26:556–560, 2006.

M. Raffel. *Particle image velocimetry: a practical guide*. Springer, 2007.

K. L. Rankin and R. I. Hires. Laboratory measurement of bottom shear stress on a movable bed. *Journal of Geophysical Research*, 105:17011–17019, 2000.

B. Raubenheimer. Observations of swash zone velocities: A note on friction coefficients. *Journal of Geophysical Research*, 109:C01027, 2004.

P. H. Riedel and J. W. Kamphuis. A shear plate for use in oscillatory flow. *Journal of Hydraulic Research*, 11:137–156, 1973.

J. S. Russell. Report on waves. In *Report of the fourteenth meeting of the British Association for the Advancement of Science*, pages 311–390, London, 1845. John Murray.

H. S. Saeki, A. O. Hanayasu, and K. Takgi. The shoaling and run-up height of the solitary wave. *Coastal Engineering in Japan*, 14:25–42, 1971.

J. K. Seelam, P. A. Guard, and T. E. Baldock. Measurement and modeling of bed shear stress under solitary waves. *Coastal Engineering*, 58:937–947, 2011.

M. C. Shen and R. E. Meyer. Climb of a bore on a beach. Part3. Run-up. *Journal of Fluid Mechanics*, 16:113–125, 1963.

A. D. Short. Coastal processes and beaches. *Nature Education Knowledge*, 3:15, 2012.

R. R. Simons, T. J. Grass, and M. Mansour-Tehrani. Bottom shear stresses in the boundary layers under waves and currents crossing at right angles. *Proceedings of 23rd International Conference on Coastal Engineering*, pages 604–617, 1992.

R. R. Simons, T. J. Grass, W. M. Saleh, and M. M. Tehrani. Bottom shear stresses under random waves with a current superimposed. *Proceedings of 24th International Conference on Coastal Engineering*, pages 565–578, 1994.

J. E. Skjelbreia. *Observations of breaking waves on sloping bottoms by use of laser Doppler velocimetry*. PhD thesis, California Institute of Technology, 1987.

I. M. Sou and H. Yeh. Laboratory study of the cross-shore flow structure in the surf and swash zones. *Journal of Geophysical Research*, 116:C03002, 2011.

I. M. Sou, E. A. Cowen, and P. L.-F. Liu. Evolution of the turbulence structure in the surf and swash zones. *Journal of Fluid Mechanics*, 644:193—216, 2010.

P. R. Spalart. Direct simulation of a turbulent boundary layer up to R=1410. *Journal of Fluid Mechanics*, 187:61–98, 1988.

J. J. Stoker. *Water Waves*. Interscience, New York, 1957.

B. M. Sumer, P. M. Jensen, L. B. Sørensen, J. Fredsøe, P. L.-F. Liu, and S. Carstensen. Coherent structures in wave boundary layers. Part 2. Solitary motion. *Journal of Fluid Mechanics*, 646:207–231, 2010.

B. M. Sumer, M. B. Sen, I. Karagali, B. Ceren, J. Fredsøe, M. Sottile, L. Zilioli, and D. R. Fuhrman. Flow and sediment transport induced by a plunging solitary wave. *Journal of Geophysical Research*, 116:C01008, 2011.

B. M. Sumer, H. Guner, and N. M. Hansen. Laboratory observations of flow and sediment transport induced by plunging regular waves. *Journal of Geophysical Research: Oceans*, 118:6161–6182, 2013.

I. A. Svendsen. *Introduction to Nearshore Hydrodynamics*, volume 24 of *Advanced Series on Ocean Engineering*. World scientific, 2006.

C. E. Synolakis. *The runup of long waves*. PhD thesis, California Institute of Technology, 1986.

C. E. Synolakis. The runup of solitary waves. *Journal of Fluid Mechanics*, 185: 523–545, 1987.

C. E. Synolakis. Generation of long waves in laboratory. *Journal of Waterway, Port, Coastal, and Ocean Engineering*, 116:252–266, 1990.

C. E. Synolakis. Green's law and the evolution of solitary waves. *Physics of Fluids A: Fluid Dynamics*, 3:490–491, 1991.

C. E. Synolakis and E. N. Bernard. Tsunami science before and beyond Boxing Day 2004. *Philosophical Transactions of the Royal Society A: Mathematical, Physical and Engineering Sciences*, 364:2231–2265, 2006.

C. E. Synolakis and J. E. Skjelbreia. Evolution of maximum amplitude of solitary waves on plane beaches. *Journal of Waterway, Port, Coastal, and Ocean Engineering*, 119:323–342, 1993.

M. Tanaka. The stability of solitary waves. *Physics of Fluids*, 29:650–655, 1986.

J. R. Taylor. *An introduction to error analysis*. University science books, 1997.

G. Watson, T. C. D. Barnes, and D. H. Peregrine. The generation of low-frequency waves by a single wave group incident on a beach. *Coastal Engineering Proceedings*, 1:1–26, 1994.

G. B. Whitham. The Effects of Hydraulic Resistance in the Dam-Break Problem. *Proceedings of the Royal Society A: Mathematical, Physical and Engineering Sciences*, 227:399–407, 1955.

G. B. Whitham. On the propagation of shock waves through regions of non-uniform area or flow. *Journal of Fluid Mechanics*, 4:337–360, 1958.

R. L. Wiegel. Transformation of swell over a reef. *Shore & Beach*, 58:31, 1990.

P. Winckler, P. L.-F. Liu, and C. Mei. Advective Diffusion of Contaminants in the Surf Zone. *Journal of waterway, port, coastal, and ocean engineering*, 139:437–454, 2013.

K. G. Winter. An outline of the techniques available for the measurement of skin friction in turbulent boundary layers. *Progress in Aerospace Sciences*, 18:1–57, 1979.

H. Yeh and A. Ghazali. On bore collapse. *Journal of Geophysical Research: Oceans*, 93:6930–6936, 1988.

H. Yeh, A. Ghazali, and I. Marton. Experimental study of bore run-up. *Journal of Fluid Mechanics*, 206:563–578, 1989.

H. H. Yeh and K. M. Mok. On turbulence in bores. *Physics of Fluids A: Fluid Dynamics*, 2:821–828, 1990.

Z.-J. You and B. S. Yin. Direct measurement of bottom shear stress under water waves. *Journal of Coastal Research, SI*, 50:1132–1136, 2007.

J. A. Zelt. The run-up of nonbreaking and breaking solitary waves. *Coastal Engineering*, 15:205–246, 1991.

Q. Zhang and P. L.-F. Liu. A numerical study of swash flows generated by bores. *Coastal Engineering*, 55:1113—1134, 2008.